Astronomy & Astrophysics manuscript no. output
September 25, 2023

A Survey of SiO $J = 1 - 0$ emission toward massive star-forming regions

W.-J. Kim[1,5], J. S. Urquhart[2], V. S. Veena[1,3], G. A. Fuller[1,4], P. Schilke[1], and K-T Kim[5,6]

[1] I. Physikalisches Institut, Universität zu Köln, Zülpicher Str. 77, 50937 Köln, Germany
e-mail: wonjukim@ph1.uni-koeln.de
[2] Centre for Astrophysics and Planetary Science, University of Kent, Ingram Building, Canterbury, Kent CT2 7NH, UK
[3] Max-Planck-Institut für Radioastronomie, Auf dem Hügel 69, 53121 Bonn, Germany
[4] Jodrell Bank Centre for Astrophysics, Department of Physics and Astronomy, the University of Manchester, Oxford Road, Manchester M13 9PL, UK
[5] Korea Astronomy and Space Science Institute, 776 Daedeokdae-ro, Yuseong-gu, Daejeon 34055, Republic of Korea
[6] University of Science and Technology, Korea (UST), 217 Gajeong-ro, Yuseong-gu, Daejeon 34113, Republic of Korea

Received ; accepted

ABSTRACT

Aims. The application of silicon monoxide (SiO) as a shock tracer arises from its propensity to occur in the gas phase as a result of shock-induced phenomena, including outflow activity and interactions between molecular clouds and expanding HII regions or supernova remnants. Here we search for indications of shocks toward 366 massive star-forming regions by observing the ground rotational transition of SiO ($v = 0$, $J = 1 - 0$) at 43 GHz with the Korean VLBI Network (KVN) 21 m telescopes to extend our understanding on the origins of SiO in star-forming regions.
Methods. We analyze the thermal SiO 1 – 0 emission and compare the properties of SiO emission with the physical parameters of associated massive dense clumps as well as 22 GHz H_2O and Class I 44 GHz CH_3OH maser emission.
Results. We detect SiO emission toward 104 regions which consist of 57 IRDCs, 21 HMPOs, and 26 UCHIIs. Out of 104 sources, 71 and 80 sources have 22 GHz H_2O and 44 GHz Class I CH_3OH maser counterparts, respectively. The determined median SiO column density, N(SiO), and abundance, X(SiO), relative to $N(H_2)$ are 8.12×10^{12} cm^{-2} and 1.28×10^{-10}, respectively. These values are similar to those obtained toward other star-forming regions and also consistent with predicted values from shock models with low-velocity shocks ($\lesssim$10 – 15 km s^{-1}). For sources with dust temperatures ($T_{\rm dust}$) $\lesssim$ 20 K, we find that N(SiO) and X(SiO) derived with the $J = 1 - 0$ transition are a factor $\sim$ 3 larger than those from the previous studies obtained with SiO 2 – 1. While the X(SiO) does not exhibit any strong correlation with the evolutionary stages of their host clumps, $L_{\rm SiO}$ is highly correlated with dust clump mass, and $L_{\rm SiO}/L_{\rm bol}$ also has a strong negative correlation with $T_{\rm dust}$. This shows that colder and younger clumps have high $L_{\rm SiO}/L_{\rm bol}$ suggestive of an evolutionary trend. This trend is not due to excess emission at higher velocities, such as SiO wing features, as the colder sources with high $L_{\rm SiO}/L_{\rm bol}$ ratios lack wing features. Comparing with H_2O and Class I CH_3OH masers, we find a significant correlation between $L_{\rm SiO}/L_{\rm bol}$ and $L_{\rm CH_3OH}/L_{\rm bol}$ ratios, whereas no similar correlation is seen for the H_2O maser emission. This suggests a similar origin for the SiO and Class I CH_3OH emission in these sources.
Conclusions. We demonstrate that in cold regions SiO $J = 1 - 0$ may be a better tracer of shocks than higher J transition of SiO. Lower $T_{\rm dust}$ (and so probably less globally evolved) sources appear to have higher $L_{\rm SiO}$ relative to their $L_{\rm bol}$. The SiO 1 – 0 emission toward infrared dark sources ($T_{\rm dust} \lesssim 20$ K), which do not contain identified outflow sources, may be related to other mechanisms producing low-velocity shocks (5 – 15 km s^{-1}) for example, arising from cloud-cloud collisions, shocks triggered by expanding HII regions, global infall, or converging flows.

Key words. astrochemistry – surveys – ISM:clouds – stars:formation

1. Introduction

In the quiescent cold interstellar medium (ISM), silicon monoxide (SiO) is depleted in the gas phase to the point of being undetectable as $X(\mathrm{SiO}) < 10^{-12}$ (Ziurys et al. 1989; Martin-Pintado et al. 1992) as silicon (Si) is mostly locked into the dust grain cores, although SiO can be present in the icy mantles of dust grains. SiO is only liberated into the gas phase, or formed from released Si, and detectable at millimeter and submillimeter wavelengths if the mantle or grain core is disrupted (Schilke et al. 1997; Gusdorf et al. 2008).

Most commonly, this disruption takes place in the high-velocity shocks ($v_s > 20 - 25$ km s^{-1} and up to 100 km s^{-1}) associated with outflows from young stars, with either the jets from the protostars or the interaction of the molecular outflow with the surrounding ambient gas (e.g., Gusdorf et al. 2008; Guillet et al. 2011; Kelly et al. 2017). In addition to outflow regions with strong radiation regions such as photodissociation regions (PDRs), photo-desorption can also lead to an enhancement of SiO in the gas phase (Walmsley et al. 1999; Schilke et al. 2001). Recently, SiO emission of a different nature has been detected in several regions, including massive star-forming regions (e.g., Jiménez-Serra et al. 2010; Nguyen-Lu'o'ng et al. 2013; Louvet et al. 2016; Cosentino et al. 2020) and even diffuse molecular clouds at high latitudes (e.g., Rybarczyk et al. 2023). This emission found toward active star-forming regions is spatially extended and does not always coincide with outflow sources or CO outflows (e.g., Widmann et al. 2016), which are concentrated on smaller scales (< 0.05 pc).

Spatially extended SiO emission with a typical fractional SiO abundance, X(SiO), of 10^{-11} – 10^{-10} is not only weaker than expected from energetic outflows associated with massive stars, which produce bright and broad lines with X(SiO) from 10^{-9} to $\sim 10^{-7}$ (e.g., Jiménez-Serra et al. 2010; López-Sepulcre et al. 2016), but often also has a narrower line width range, typically, $\sim 2-4$ km s^{-1}, even smaller than 1 km s^{-1} for some cases (e.g., Jiménez-Serra et al. 2010; Cosentino et al. 2020). Such narrow SiO emission lines imply the existence of low-velocity shocks. According to several observational studies with shock models (e.g., Nguyen-Lu'o'ng et al. 2013; Jiménez-Serra et al. 2008; Duarte-Cabral et al. 2014; Louvet et al. 2016; Csengeri et al. 2011a,b), shock velocities of 5 – 15 km s^{-1}can produce abundances of SiO about 10^{-11} – 10^{-10}. Two possible explanations have been proposed for the origin of narrow and spatially extended SiO emission: (1) association with the outflows from an undetected dispersed population of low-mass protostars (Jiménez-Serra et al. 2010), (2) produced in low velocity, large scale shocks associated with the formation of the molecular cloud themselves, perhaps as a result of colliding/converging flows (e.g., Csengeri et al. 2011a,b, 2016a), cloud-cloud collisions (e.g., Cosentino et al. 2020; Armijos-Abendaño et al. 2020; Zhu et al. 2023) or accretion flows associated with global collapse (e.g., Duarte-Cabral et al. 2014), or (3) low-velocity shocks (~ 20 km s^{-1}) driven by supernova remnants, interacting with adjacent molecular clouds (e.g., Vaupré et al. 2014; Dumas et al. 2014; Cosentino et al. 2019, 2022).

Massive stars ($> 8-10$ M$_\odot$) and their clusters of lower mass companions form in massive (up to several 10^3 M$_\odot$), pc-sized clumps within molecular clouds (Urquhart et al. 2022; Elia et al. 2021). Understanding how stars form in such environments requires tracing the gas flow from the clouds through the clumps and the progenitors of individual stars, ~ 0.1 pc-sized cores, and ultimately on to the protostars. Observational evidence increasingly shows that the formation of most massive clumps is driven by the global collapse of regions several parsec in size (e.g., Csengeri et al. 2017; Jackson et al. 2019; Pillai et al. 2023). Peretto et al. (2013) and Wyrowski et al. (2016) report an infall rate range between $(0.3-16) \times 10^{-3}$ M$_\odot$/yr for massive clumps that are in a wide range of evolutionary stages. Blue asymmetric line profiles of HCO$^+$ ($J = 1-0$), which are diagnostic of infall motions, have also been observed on pc-scales in massive but less evolved regions (Fuller et al. 2005; Traficante et al. 2018; Pillai et al. 2023). However, the exact nature of these gas infall motions, such as how they are initiated and their role in assembling massive clumps, is still unclear.

In this paper, we will use SiO ($J = 1-0$) observations towards 366 massive star-forming regions to explore the connection between extended shocks and star formation activity. In Sect. 2, we describe the source selection criteria, observational setup, and data reduction. We complement these observations with H_2O and Class I CH_3OH masers archival data as well as properties derived from dust surveys (i.e., molecular hydrogen column density and dust temperature, Urquhart et al. 2018, 2022; Marsh et al. 2017); these are introduced in Sect. 2. In Sect. 3, we present the SiO (1 – 0) detection statistics, line profiles, and determined column density and abundances. In Sect. 4, we compare the SiO column densities and abundances with the archival datasets (dust properties and maser associations) and discuss the origin of SiO (1 – 0) emission. We summarize our results and highlight our main findings in Sect. 5.

2. Observation

2.1. Description of target sources

We selected 366 sources toward massive star-forming regions from five catalogs covering three different categories, there are being: infrared dark clouds (IRDCs) defined as high extinction regions against bright mid-infrared Galactic background (Perault et al. 1996; Egan et al. 1998; Hennebelle et al. 2001; Rathborne et al. 2006; Peretto & Fuller 2009), high-mass protostellar objects (HMPOs, Molinari et al. 1996) considered as a precursor of ultra-compact HII regions (UCHIIs), and molecular clump hosting UCHIIs (Wood & Churchwell 1989b; Kurtz et al. 1994) considered to be the most evolved evolutionary stage of the massive star formation. The selected sources consist of 134 infrared dark cloud (IRDC) cores toward 33 IRDCs taken from Rathborne et al. (2006), 129 high-mass protostellar objects (HMPOs) taken from the catalogs of Molinari et al. (1996) and Sridharan et al. (2002), and 103 UCHIIs from the radio continuum catalogs of Wood & Churchwell (1989b) and Kurtz et al. (1994).

The 134 IRDC cores are identified as compact dust emission sources at 1.2 mm wavelength observed with the 117 element bolometer array MAMBO II at the Institut de Radioastronomie Millimetrique (IRAM) 30 m telescope (Rathborne et al. 2006), and based on their mid-infrared emission, the cores are characterized as associated to different evolutionary phases (Chambers et al. 2009). The UCHII sources were initially selected with *IRAS* colors ($\mathrm{Log}(F_{60}/F_{12}) \geq 1.30$ and $\mathrm{Log}(F_{25}/F_{12}) \geq 0.57$); Wood & Churchwell 1989a) and later the 103 sources were confirmed as UCHIIs with radio continuum emission observations at 2/6 cm and 7 mm wavelengths (Wood & Churchwell 1989b; Kurtz et al. 1994; Walsh et al. 1998; Carral et al. 1999) (see Kim et al. 2019 for details). The 129 HMPOs are selected from two different catalogs that are Molinari et al. (1996) and Sridharan et al. (2002). The sources from Molinari et al. (1996) are divided into two groups, indicated as *High* and *Low* based on the *IRAS* colors. The catalog from Molinari et al. (1996) has the same *IRAS* color criteria used for the UCHII catalogs of Wood & Churchwell (1989b) and Kurtz et al. (1994), and due to the same initial selection criteria, HMPO candidates referred to as *High* can potentially be UCHIIs. The other HMPO catalog from Sridharan et al. (2002) used the *IRAS* criteria defined by Ramesh & Sridharan (1997), and besides, all the selected sources are satisfied by the following criteria: detection of CS (2 – 1) line (Bronfman et al. 1996), $F_{60} > 90$ Jy and $F_{100} > 500$ Jy, and the absences of radio continuum emission detected from the Galaxy-Wide 5 GHz Green bank (Gregory & Condon 1991) and Parkes-MIT-NRAO ratio continuum surveys (Griffith et al. 1994; Wright et al. 1994). Except for the UCHII source group, the source classifications for the two categories (i.e., IRDC and HMPO) are not definitive. Thus instead of using the three catalogs, we use the ratio of bolometric luminosity and clump mass as well as dust temperatures for indicators of evolutionary stages. However, as supplementary information, we list the classification defined in The APEX Telescope Large Area Survey of the Galaxy (ATLASGAL) survey (Urquhart et al. 2022). For the UCHII sample, if there are no classifications from the ATLASGAL catalog, we refer to their classification as MSF (radio-HII) in the classification column because we already know that all the sources have radio continuum sources indicating them as HII regions (Kim et al. 2019). Table 1 lists information on the observed sources.

Table 1: Summary of sources.

Source name	R.A. α (J2000)	Dec. δ (J2000)	v_{sys} (km s^{-1})	SiO (1 – 0)	H_2O Maser	CH_3OH Maser	Selected Category	ATLASGAL Name	Classification
IRAS18032−2032	18:06:14	−20:31:47	5.0	Y^b	Y	Y	UCHII	009.621+00.194	MSF (radio-HII)*
G8.67−0.36	18:06:19	−21:37:32	38.0	Y^b	Y	Y	UCHII	008.671−00.356	MSF (radio-HII)*
G10.47+0.03	18:08:38	−19:51:52	66.2	Y^b	Y	Y	UCHII	010.472+00.027	MSF (radio-HII)*
G10.30−0.15	18:08:56	−20:05:54	11.0	Y^b	Y	Y	UCHII	010.299−00.147	MSF (radio-HII)*
G10.15−0.34	18:09:25	−20:19:15	5.0	N	N	N	UCHII	–	MSF (radio-HII)*
IRAS18073−2046	18:10:17	−20:45:43	28.0	N	Y	Y	UCHII	009.879−00.751	MSF (radio-HII)*
G10.62−0.38	18:10:24	−19:56:15	−3.0	N	Y	Y	UCHII	–	MSF (radio-HII)*
IRAS18085−1931	18:11:33	−19:30:39	−1.1	Y^e	N	N	UCHII	011.109−00.397	MSF (radio-HII)*
HM18089−1732	18:11:51	−17:31:28	33.0	Y^c	Y	Y	HMPO	012.888+00.489	MSF (radio-HII)
HM18090−1832	18:12:02	−18:31:56	110.0	N	N	N	HMPO	012.024−00.031	YSO
G12.21−0.10	18:12:40	−18:24:21	20.0	Y^{b,c}	Y	Y	UCHII	012.208−00.102	MSF (radio-HII)*
G12.43−0.05	18:12:55	−18:11:08	40.0	N	N	N	UCHII	012.431−00.049	MSF (radio-HII)*
HM18102−1800	18:13:12	−17:59:35	21.0	Y^b	N	Y	HMPO	–	unclassified
G11.94−0.62	18:14:01	−18:53:24	38.9	Y^{b,c}	Y	Y	UCHII	011.936−00.616	MSF (radio-HII)*
HM18144−1723	18:17:24	−17:22:13	47.0	Y^{a,c}	Y	Y	HMPO	013.658−00.599	YSO
G015.05+00.07 MM2	18:17:40	−15:48:55	24.7	N	N	N	IRDC	015.053+00.089	YSO
G015.05+00.07 MM1	18:17:50	−15:53:38	24.7	Y^d	N	N	IRDC	015.006+00.009	Quiescent
HM18151−1208	18:17:57	−12:07:22	33.0	Y^e	Y	Y	HMPO	–	unclassified
HM18159−1550	18:18:48	−15:48:54	60.0	N	N	N	HMPO	015.184−00.159	MSF (HII)
G015.31−00.16 MM2	18:18:50	−15:43:19	31.1	N	N	N	IRDC	015.271−00.122	Protostellar
G015.31−00.16 MM1	18:18:56	−15:45:00	31.1	N	N	N	IRDC	–	unclassified

Notes. This table only shows a fraction of the whole table; the remaining are available in Table A.2. v_{sys} is systemic velocity, and the velocity information is obtained from several molecular line observations (NH_3; (Churchwell et al. 1990; Molinari et al. 1996; Beuther et al. 2002; Chira et al. 2013), CS; (Bronfman et al. 1996)). Asterisk (*) in the classification column indicates UCHII sources without ATLASGAL classification. The presence of SiO wings in rotational transitions, 1 – 0 from this survey and 2 – 1 from the survey presented in (Csengeri et al. 2016a) are indicated with four different classifications: ^{a} indicates wing features in SiO 1 – 0 emission, and ^{b} means SiO wing candidates for cases with a SiO FWHM ≥ 8 kms. ^{c} indicates SiO wings in the 2 – 1 transition, and ^{d} is for the cases that there are no wings in 2 – 1 transition but a broad Gaussian component has a FWHM line width ≥ 8 kms. ^{e} marks for sources without any sign of wing features in either 1 – 0 or 2 – 1 transitions.

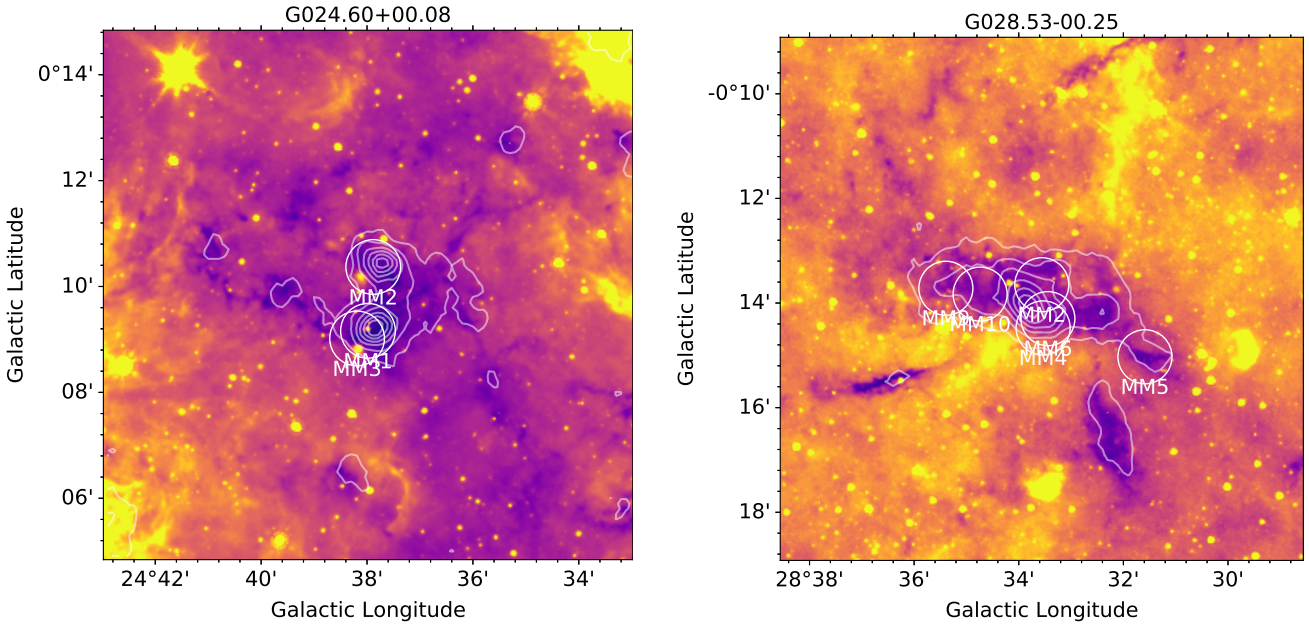

Fig. 1: GLIMPSE IRAC 8 μm image in color toward G024.50+00.08 and G028.53−00.25 from left to right, with the dust emission at 870 μm, in gray contours, made from the combined Planck/HFI and APEX/LABOCA maps (Csengeri et al. 2016b) from the ATLASGAL survey (Schuller et al. 2009). The white circles indicate the beam of KVN observations toward target sources.

2.2. SiO (1 – 0) observations and data reduction

Observations of the rotational ground state transition of SiO ($v = 0, J = 1 - 0$, 43.42376 GHz) toward 366 sources were carried out over four observation periods (2010 October - December, 2011 February, 2012 October-November, and 2013 May) using the Korean VLBI Network (KVN) 21 m telescopes[1] at the Yonsei, Ulsan and Tamna sites (Kim et al. 2011; Lee et al. 2011). The pointing and focus observations were performed every 2–3 hours by observing strong H_2O ($6_{1,6}-5_{2,3}$, 22.23508 GHz) and SiO ($v = 1$, $J = 1 - 0$, 43.12203 GHz) maser sources (i.e., V1111 Oph, R Cas, W3(OH), and Orion KL) and found

[1] https://radio.kasi.re.kr/kvn/main_kvn.php

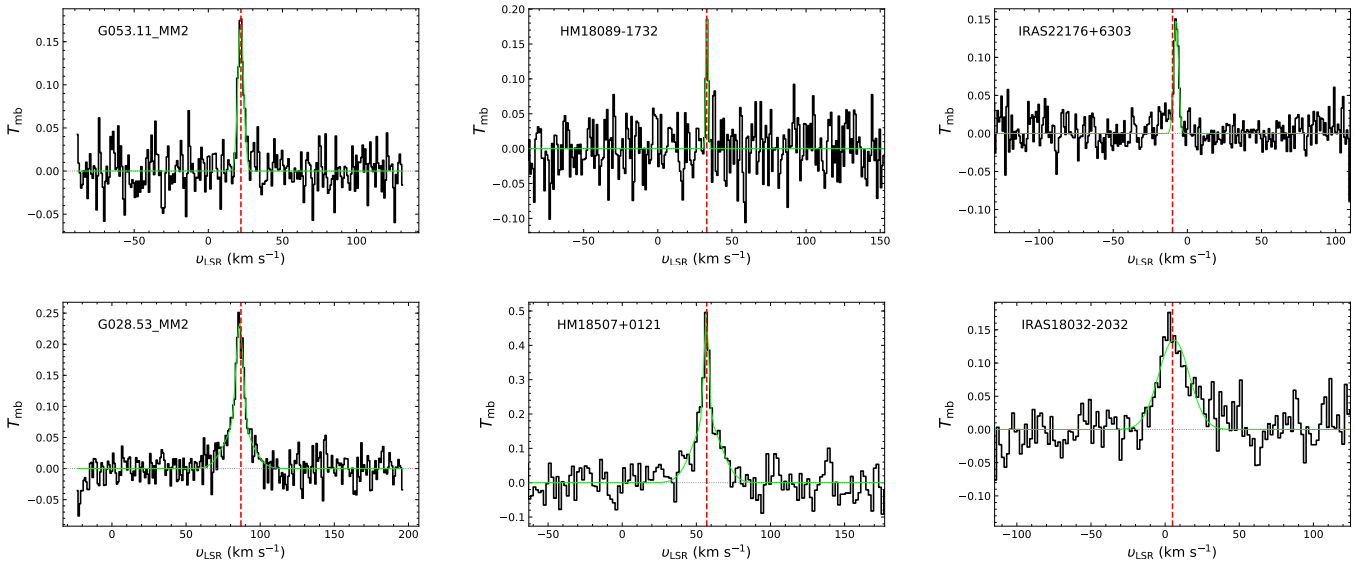

Fig. 2: 43 GHz SiO $J = 1 - 0$ spectra in T_{mb} scale toward two IRDCs (G053.11+00.05 MM2 and G28.53−00.25 MM2) in the left panel, two HMPOs (HM18089−1732 and HM18507+0121) in the middle panel, two UCHIIs (IRAS22176+6303 and IRAS18032−2032) in the right panel. The SiO spectral plots for all other detected sources are presented in Figs. D.1, D.2, D.3,D.4, D.5, and D.6. The vertical green dotted lines indicate a systemic velocity of individual sources. The purple curves are Gaussian profile fits to SiO emission.

Table 2: Beam size and efficiency.

Telescope	Beam size (″)	Beam efficiency
KVN−Yonsei	61.5	0.45
KVN−Ulsan	61.6	0.42
KVN−Tamna	62.1	0.48

Notes. These values are updated in 2013[a].

[a] https://radio.kasi.re.kr/kvn/status_report_2013/aperture_efficiency.html

to be within 5″. Position switching mode was used with a total ON+OFF integration time of ∼30 minutes per source, yielding a typical rms noise level up to ∼ 50 mK at velocity resolutions (δv) of 0.86 and 1.73 km s^{-1} depending on the noise of a spectrum. The main beam efficiencies for converting T_a^* to T_{mb} and the full-width half maxima (FWHM) of the beams are listed in Table 2. We used the Continuum and Line Analysis Single-dish Software (CLASS) software[2] of the Grenoble Image and Line Data Analysis Software (GILDAS) package (Pety 2005) for the data reduction and fitting a Gaussian profile.

In addition, to investigate the association with outflows of embedded objects and surrounding environment toward our target positions, we use published observational data of 22 GHz H_2O ($6_{1,6}-5_{2,3}$) and 44 GHz Class I CH_3OH (7_0-6_1 A$^+$) masers. These maser observations were done toward the same coordinates of our SiO sources with the same three KVN 21 m telescopes. The H_2O and CH_3OH maser data toward UCHII sources are taken from Kim et al. (2019), but both maser line parameters for the HMPO and IRDC samples are obtained from Kim (2016). In Table 1 and A.2, we provide detections of both masers toward the observed sources.

[2] https://www.iram.fr/IRAMFR/GILDAS/doc/html/class-html/class.html

3. Results and analysis

3.1. Detection and SiO line properties

We detected SiO (1 – 0) emission lines toward 106 massive star-forming regions. Among the detected sources, 59 sources are associated with the IRDCs, and the positions of two pairs of four cores (i.e., G024.60+00.08 MM1/MM3 and G028.53−00.25 MM4/MM6) as shown in Fig. 1 are very close to each other within $\frac{1}{2}$ a beam width. They match a common ATLASGAL clump, respectively. The SiO detections from these sources are likely duplicates; thus, we only include the brightest spectrum for these duplicated positions toward in the following statistical analysis. The other 21 and 26 detections are found toward HMPO and UCHII associated sources, respectively. Figures 2, D.1, D.2, D.3, and D.4 show SiO emission spectral lines detected from this survey. Table 3 and Table B.3 list Gaussian fit parameters of SiO emission lines, which are velocity-integrated intensities ($\int T_{mb}\, dv$) in K km s^{-1}, peak velocity (v_{peak}) in km s^{-1}, full width at half maximum (Δv_{FWHM}) in km s^{-1}, peak intensity ($T_{mb,\,peak}$) in K, and rms level in K. For the following analyses, we exclude the beam-overlapped sources, G024.60+00.08 MM3 and G028.53−00.25 MM4, and 104 out of 106 sources is the total number of SiO emission sources confirmed as final detections.

SiO emission lines for 86 sources are fitted with a single Gaussian profile, and in 17 cases two Gaussian components are required to fit, based on visual inspection of the residual emission after subtracting a first Gaussian component that was fitted. Only one case (G5.48−0.24) is fitted with three Gaussian components, and the FWHM line width of its broadest components is 54 km s^{-1} (see Fig. D.6). Figure 3 shows the histogram of Δv_{FWHM} for all the SiO spectral lines, and for multi-components, we plot all the fitted components, including a narrow component where the peak velocity is consistent with the ambient gas velocity and a broad component tracing outflows. The median line width marked as a black vertical line is 7.87 km s^{-1} and a sig-

Table 3: SiO line parameters.

ID	Source name	Fitted component	$\int T_{\rm mb}\, dv$ (K km s^{-1})	$v_{\rm peak}$ (km s^{-1})	$\Delta v_{\rm FWHM}$ (km s^{-1})	$T_{\rm mb,\,peak}$ (K)	rms (mK)
1	G015.05+00.07 MM1	1	0.604±0.143	24.27±0.66	6.45±1.34	0.088	15.82
	···	2	0.374±0.157	14.50±1.85	9.21±4.50	0.038	15.82
2	G018.82−00.28 MM1	1	1.732±0.194	41.08±0.37	6.70±0.85	0.243	53.67
3	G018.82−00.28 MM3	1	0.566±0.080	43.53±0.56	7.16±1.02	0.074	16.10
4	G018.82−00.28 MM4	1	1.006±0.154	63.72±1.13	15.72±3.04	0.060	18.70
5	G019.27+00.07 MM1	1	0.962±0.142	26.05±0.44	6.26±1.15	0.144	27.29
6	G019.27+00.07 MM2	1	1.216±0.142	26.93±0.32	6.16±1.03	0.186	35.07
7	G022.35+00.41 MM1	1	0.870±0.053	51.48±0.86	4.37±0.86	0.187	45.94
	···	2	1.260±0.053	52.44±0.86	20.09±0.86	0.059	45.94
8	G023.60+00.00 MM1	1	0.976±0.130	105.60±0.57	8.63±1.27	0.106	22.68
9	G023.60+00.00 MM2	1	1.452±0.218	50.79±0.58	7.53±1.38	0.181	38.91
10	G023.60+00.00 MM4	1	0.373±0.140	52.98±0.35	4.39±1.10	0.080	17.58
	···	2	0.690±0.184	46.34±1.93	14.04±3.19	0.046	17.58
11	G023.60+00.00 MM7	1	0.978±0.138	52.09±0.49	7.60±1.44	0.121	32.55
12	G024.33+00.11 MM1	1	0.864±0.057	112.60±0.29	4.54±0.42	0.179	25.55
	···	2	1.221±0.142	116.20±0.51	9.68±1.71	0.119	25.55
13	G024.33+00.11 MM2	1	1.026±0.110	116.90±0.28	5.15±0.66	0.187	34.18
14	G024.33+00.11 MM3	1	0.942±0.089	115.90±0.12	2.89±0.37	0.307	30.81
	···	2	0.276±0.082	110.80±0.58	3.64±1.05	0.071	30.81
15	G024.33+00.11 MM5	1	0.472±0.158	116.10±0.31	3.54±0.75	0.125	23.45
	···	2	2.221±0.223	116.20±1.04	15.78±2.12	0.132	23.45
16	G024.33+00.11 MM6	1	1.323±0.089	113.50±0.18	6.09±0.55	0.204	23.79
17	G024.33+00.11 MM10	1	0.487±0.102	116.20±0.48	4.94±1.36	0.093	21.63

Notes. Extract of the table of Gaussian fit parameters the SiO spectra. The full table is presented in Table B.3. If there are more a single Gaussian component fitted, the component number is indicated in Column 3.

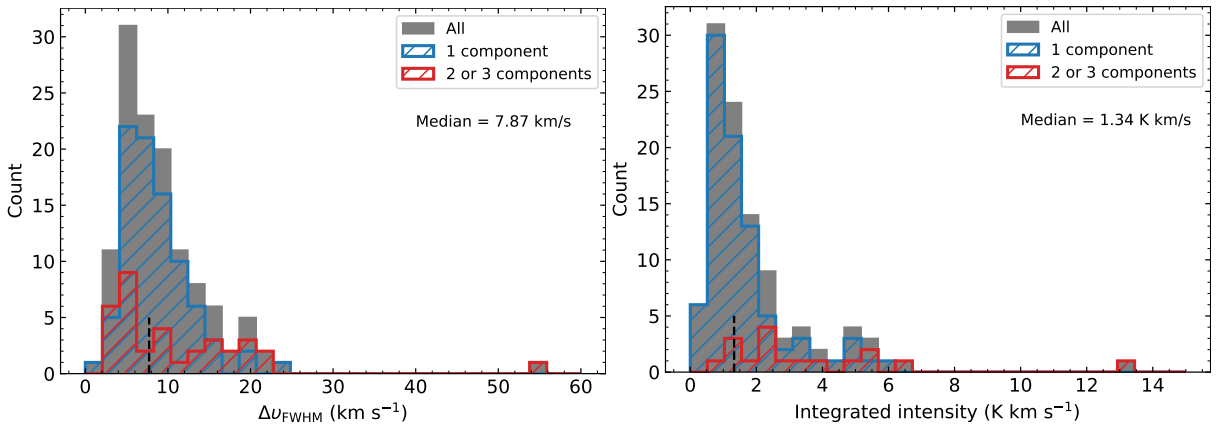

Fig. 3: Histogram of Gaussian fit line widths (left panel) and full area (right panel) of SiO (1 – 0) lines. Gray histograms indicate all the SiO detected sample. Blue and red histograms represent SiO sources fitted with one Gaussian component and with more than one Gaussian component, respectively. Black dashed-lines mark the median values of the gray histograms.

nificant fraction of the Gaussian components have FWHM narrower. The components with $\Delta v_{\rm FWHM}$ narrower than 7.87 km s^{-1} exhibit an average $\Delta v_{\rm FWHM}$ of 5.38 km s^{-1}. The narrowest observed $\Delta v_{\rm FWHM}$ being 1.8 km s^{-1} toward HM18089−1732, where the spectrum has a velocity resolution of 0.86 km s^{-1}. We note that in some cases, weak SiO emission lines are smoothed to a velocity resolution of 1.73 km s^{-1}, which can cause broadened line widths.

The median value (7.87 km s^{-1}) of $\Delta v_{\rm FWHM}$ toward our data are close to 8 km s^{-1}. If the $\Delta v_{\rm FWHM}$ is narrower than 8 km s^{-1}, we, thus, consider the SiO emission lines as low-velocity components. The same $\Delta v_{\rm FWHM}$ is used in Csengeri et al. (2016a). The average $\Delta v_{\rm FWHM}$ of the narrow components from one and multiple Gaussian fitting are 5.71 and 4.63 km s^{-1}, respectively, and for broad components, we obtained 11.46 and 17.39 km s^{-1}, respectively. These average values are in good agreement with the $\Delta v_{\rm FWHM}$ (∼5 – 6 kms and 14 – 19 km s^{-1}) obtained from SiO 2 – 1 emission measured toward massive dust clumps (Csengeri et al. 2016a). As depicted in the upper panels of Fig. 2, certain sources exhibit narrower SiO profiles compared to others (lower panels), characterized by broader wings fitted with a broad Gaussian component. The histogram of the total velocity integrated intensity shows that multiple Gaussian component SiO lines have a bright total velocity integrated intensity

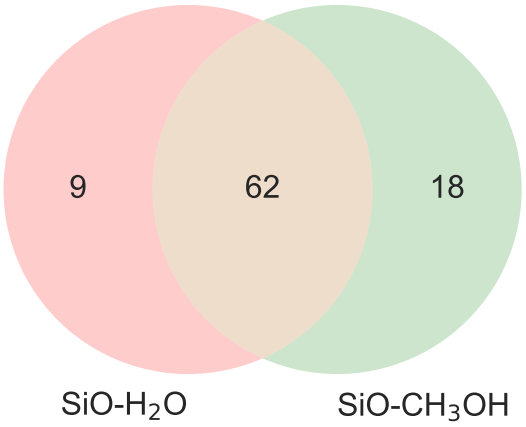

Fig. 4: Venn diagram for H_2O and CH_3OH maser detections toward SiO detected sources.

than those with a single Gaussian component, except for some sources that are associated with a single bright components.

The Venn diagram in Figure 4 illustrates the distribution of H_2O and Class I CH_3OH masers toward 104 SiO detected sources. We find 22 GHz H_2O maser emission toward 71 sources (in red and orange colored areas), and 80 sources have 44 GHz Class I CH_3OH masers (in green and orange colored areas). Among these maser-detected sources, 62 sources (in the orange colored area) have both maser emission lines. Out of 71 SiO-H_2O detected sources, 9 positions do not have CH_3OH maser emission lines, and 18 sources of the 80 SiO-CH_3OH detected sources only have CH_3OH masers, not H_2O masers. Toward HMPOs and UCHIIs associated sources, most SiO detected sources have either H_2O or CH_3OH masers, and only 2 and 5 sources toward HMPOs and UCHIIs respectively have SiO detection without maser emission. On the other hand, toward IRDC sources, 26 and 18 sources with SiO detections have a lack of H_2O and CH_3OH maser emission lines, respectively.

3.2. Physical properties of SiO detected and non-detected sources

We investigated the physical properties (bolometric luminosity, clump mass, dust temperature, and L_{bol}/M_{clump}) derived from Urquhart et al. (2018) toward the SiO detected and non-detected sources. Figure 5 displays histograms of these properties of sources showing the SiO detections (red bars) and non-SiO detections (gray bars). To qualify the statistical significance of these differences, we performed Kolmogorov-Smirnov (KS) tests to M_{clump} and T_{dust} between the two groups. The $p-$values from the KS-tests are remarkably small, $\ll 0.001$, indicating a significant distinction between the groups. The distribution of SiO emission sources in L_{bol}/M_{clump} spread widely, while the non-SiO detected sources trend to be concentrated to associated clumps with higher L_{bol}/M_{clump} indicating more evolved clumps. The KS-test resulted in a reasonably small $p-$value, 0.007, implying that the SiO emission clumps are likely different with the clumps without SiO emission. In addition, we do not find any apparent differences in source distances and L_{bol} toward sources of the two groups, with large $p-$values > 0.09 and 0.8, respectively. In summary, the SiO detected sources are notably associated with massive (median Log M_{clump} = 3.26) and colder (a median T_{dust} = 20 K) sources compared to the sources without

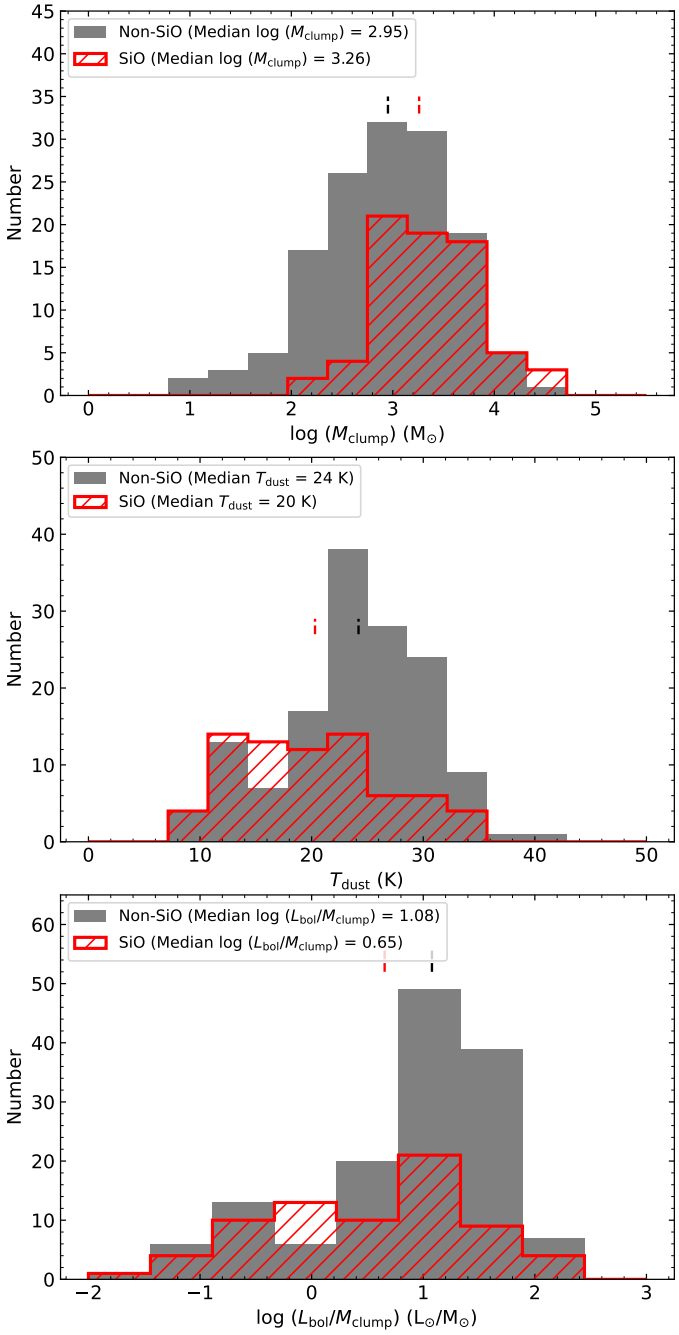

Fig. 5: Histograms of dust clump mass (top panel), dust temperature (middle panel), and bolometric luminosity over dust clump mass (bottom panel) for sources with SiO detection (red) and non-detection (gray). The black and red vertical dashed lines correspond to the median values of the respective physical properties for SiO detected and non-SiO detected sources, respectively.

SiO emission. In addition, there is an indication that the SiO detected sources have a lower median L_{bol}/M_{dust} by a factor $\sim 40\%$ lower than the non-detected sources, suggestive of being somewhat less evolved.

Table 4: Derived column density and abundances, and physical parameters of associated dust clumps.

Source	N_{SiO} (cm^{-2})	Log(N_{H_2})^a (cm^{-2})	Log(N_{H_2})^b (cm^{-2})	X_{SiO}	Dist. (kpc)	T_{dust} (K)	Log(L_{bol}) ($L_\odot$)	Log(M_{clump}) ($M_\odot$)	L_{H_2O} ($L_\odot$)	L_{CH_3OH} ($L_\odot$)
G018.82−00.28MM1	1.06×10^{13}	23.055	22.936	9.34×10^{-11}	12.6	18.7	4.806	4.369	1.34×10^{-3}	9.71×10^{-5}
G019.27+00.07MM2	7.44×10^{12}	22.714	22.560	1.44×10^{-10}	2.8	12.1	2.079	2.713	2.31×10^{-6}	···
G022.35+00.41MM1	1.30×10^{13}	22.953	22.465	1.45×10^{-10}	3.6	13.1	2.420	3.057	6.70×10^{-6}	4.23×10^{-6}
G023.60+00.00MM1	5.97×10^{12}	22.930	22.771	7.02×10^{-11}	5.9	16.9	3.782	3.519	1.21×10^{-6}	2.42×10^{-5}
G023.60+00.00MM2	8.89×10^{12}	22.806	22.673	1.39×10^{-10}	3.6	16.7	3.362	3.064	···	1.24×10^{-5}
G31.41+0.31	5.57×10^{12}	23.696	···	1.12×10^{-11}	4.9	22.0	4.800	3.852	1.52×10^{-4}	1.30×10^{-5}
G33.92+0.11	4.49×10^{12}	23.048	22.857	4.02×10^{-11}	6.9	27.4	5.226	3.726	7.73×10^{-7}	5.26×10^{-6}
G34.26+0.15	2.87×10^{13}	23.917	23.253	3.48×10^{-11}	2.9	29.2	5.330	3.776	3.34×10^{-4}	2.58×10^{-5}
G45.47+0.05	1.06×10^{13}	22.915	22.763	1.29×10^{-10}	7.7	29.0	5.557	3.779	2.61×10^{-5}	···
HM18507+0121	3.40×10^{13}	23.249	22.679	1.92×10^{-10}	2.9	20.5	4.042	3.260	1.37×10^{-4}	2.25×10^{-5}
HM18517+0437	3.50×10^{12}	···	···	···	1.9	···	···	···	1.50×10^{-6}	7.47×10^{-7}
HM18530+0215	7.74×10^{12}	22.855	22.624	1.08×10^{-10}	4.7	26.1	4.674	3.283	···	6.20×10^{-6}
HM18566+0408	8.28×10^{12}	22.908	22.606	1.02×10^{-10}	4.9	22.5	4.365	3.293	9.69×10^{-6}	4.64×10^{-6}
HM19217+1651	5.22×10^{12}	22.659	22.373	1.15×10^{-10}	10.9	29.1	5.035	3.457	2.37×10^{-4}	4.04×10^{-5}

Notes. Only a fraction of the entire table is presented here, and the remaining results are provided in Table C.4. The properties of dust clumps are taken from the ATLASGAL point source catalog (Urquhart et al. 2018, 2022). $N(H_2)$ preceded by superscript a is from the ATLASGAL catalog, and the other one marked by b is measured from the Hi-GAL PPMAP over the observed KVN beam size. The listed X(SiO) are determined using $N(H_2)$ from the ATLASGAL catalog. All other clump physical parameters (i.e., T_{dust}, Log(L_{bol}), and Log(M_{clump})), and distance also come from the ATLASGAL catalog. L_{H_2O} and L_{CH_3OH} are recalculated with the distance from the point source catalog and velocity-integrated intensities of H_2O and Class I CH_3OH are taken from Kim (2016) and Kim et al. (2019).

3.3. SiO (1 – 0) column density and abundance

We assume that the SiO (1−0) is optically thin (e.g., Csengeri et al. 2016a), and so the total column density is given by,

$$N_{tot}^{thin} = \left(\frac{8\pi\nu^3}{c^3 A_{ul}}\right)\left(\frac{Q(T)}{g_u}\right)\frac{\exp\left(\frac{E_u}{k_B T_{ex}}\right)}{\exp\left(\frac{h\nu}{k_B T_{ex}}\right)-1} \times \frac{1}{[J_\nu(T_{ex}) - J_\nu(T_{bg})]}\int \frac{T_{MB}}{f}\,dv \quad (1)$$
$$\simeq 6.12\times10^{12}\int T_{MB}\,dv,$$

where ν is 43423.760 MHz, the Einstein coefficient for spontaneous emission, A_{ul}, is 3.049×10^{-6} s^{-1}, and the statistical weight of the upper state level, g_u is 3. $Q(T)$ and k_B are the partition function and Boltzmann constant, respectively. The energy of the upper level, E_u, is 2.084 K. All these values are taken from the Cologne Database for Molecular Spectroscopy (CDMS, Müller et al. 2005; Endres et al. 2016). The partition function at 10 K is calculated by interpolating data from the CDMS. $\int T_{MB}\,dv$ is the velocity integrated main beam temperature of an observed source, and f is the beam filling factor, which is the fraction of the beam filled by the source. Here we consider the calculated column densities are beam-averaged values, and the medium is spatially homogeneous and larger than the size of the beam. Thus, the beam filling factor is adopted to be 1. We note that toward some sources the beam filling factor could be smaller than 1 if a SiO 1–0 emitting region is localized on scales smaller than the beam. In these cases, the beam filling factors will be smaller than unity and the derived column density is a lower limit. $J_\nu(T)$ is the Rayleigh-Jeans temperature, $J_\nu(T) \equiv \frac{h\nu/k_B}{\exp(h\nu/k_B T)-1}$. T_{bg} is the background emission temperature assumed to be 2.7 K that is the cosmic microwave background radiation. Some sources do not have available T_{dust} measurements, and the SiO emitting regions are not always necessarily associated with embedded sources heating dust grains. It is also possible that the SiO and dust grains are not in thermal equilibrium. We assumed a fixed excitation temperature, T_{ex}, of 10 K for all the sources. Given that our data will be compared with other SiO surveys that have also utilized the same fixed excitation temperature for calculating the SiO column density, this assumption remains valid within this specific context. However, to consider the potential variation in N(SiO) caused by an unknown T_{ex}, we estimated uncertainties in N(SiO) using a range of temperatures. We applied 5 K as the lower limit, while considering T_{dust} as the upper limits if T_{dust} is available. Thus, N(SiO) derived in this study only represent lower limits of the measurements. Instead of using integrated intensity over the full width at zero power (FWZP), we adopt velocity-integrated intensity from Gaussian fit to avoid overestimating SiO column density due to noise. We derived SiO (1−0) column density, N(SiO), in a range 2.18×10^{12} – 7.92×10^{13} cm^{-2} toward the all detected positions. The median N(SiO) is 8.12×10^{12} cm^{-2}. The N(SiO) derived in this study are comparable with the SiO column densities (1.6×10^{12} – 7.9×10^{13} cm^{-2} from SiO 2 – 1 and $0.31 - 4.32\times10^{12}$ cm^{-2} from SiO 1 – 0) determined from SiO 1 – 0 and 2 – 1 surveys toward other massive star-forming regions (Csengeri et al. 2016a; Zhu et al. 2020).

To determine the SiO abundance, X(SiO) relative to molecular hydrogen, we used H_2 column densities from the ATLASGAL catalog (Urquhart et al. 2018, 2022) but also obtained a beam-averaged $N(H_2)$ from H_2 column density maps produced by the point process mapping (PPMAP) to Hi-GAL data (Marsh et al. 2017) using the Python package, `Photutils`. N(SiO), $N(H_2)$, and X(SiO), that are derived here, and physical properties of associated dust clumps are listed in Tables 4 and C.4. With $N(H_2)$ obtained from PPMAP, the median and mean SiO abundances are 1.95×10^{-10} and 3.00×10^{-10}. The SiO abundance can change significantly depending on $N(H_2)$, and thus to compare with SiO data from other surveys, we also use H_2 column densities obtained from Urquhart et al. (2018, 2022) for the other catalogs, which will be compared with SiO column densities of our sources. The median and mean SiO abundances determined using the H_2 column densities from Urquhart et al. (2018, 2022) are 1.28×10^{-10} and 1.71×10^{-10}, respectively. These abundances are close to the estimated abundances with the beam-average $N(H_2)$ from PPMAP. In the following sections, we will use the physical parameters of associated clumps as well as $N(H_2)$ taken from

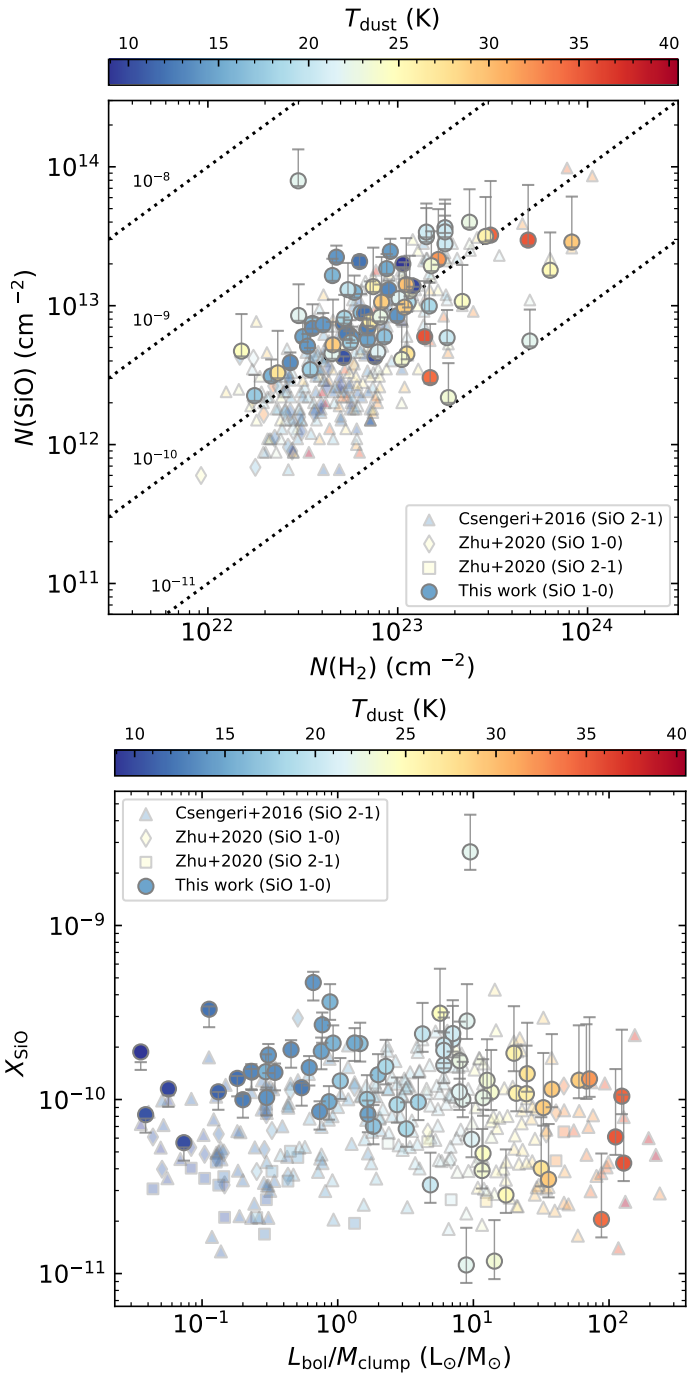

Fig. 6: *Upper*: Molecular hydrogen column density versus SiO column density. Black diagonal dot-lines indicate SiO abundance on the y-axis relative to $N(H_2)$, with its values labelled. *Lower*: Comparison between L_{bol}/M_{clump} and SiO abundance. Uncertainties depending on T_{ex} are indicated with error bars for both the plots.

the ATLASGAL catalog only for comparisons with previous surveys (i.e., Csengeri et al. 2016a; Zhu et al. 2020). In addition, for discussion, we will use the PPMAP $N(H_2)$ column densities for sources that do not have ATLASGAL counterparts within the single-dish beam size. For uncertainties in X(SiO), we used upper and lower limits of N(SiO) using a range of excitation temperatures (from 5 K to T_{dust}) but used a fixed $N(H_2)$. Thus, we note that these X(SiO) values and their uncertainties are probably lower limits since SiO in the gas-phase will likely only exist in part of the relative H_2 column density. Moreover, additional uncertainties arising from Gaussian fits, calculated with $\sqrt{\sigma_1^2 + \sigma_2^2}$ where σ_1 and σ_2 represent uncertainties of $\int T_{mb}\, dv$ for the narrow and broad Gaussian components respectively, are found to be insignificant.

4. Discussion

4.1. Comparisons with the properties of dust clumps

To understand the origin of SiO (1 – 0) emission, we compare the physical parameters of dust clumps associated with the detected SiO emission. The selected categories of observed sources do not provide the evolutionary stages of the embedded sources or surroundings. For instance, even some IRDCs, considered as the earliest stage, host evolved embedded objects, such as young stellar objects or hyper/ultra-compact HII regions. For this reason, we utilize dust temperature and L_{bol}/M_{clump} as an indicator of the evolutionary stages of star formation (Urquhart et al. 2018, 2022). Thus, in the following analyses, we exclusively compare sources with ATLASGAL counterparts to use the physical parameters measured from the dust continuum. In the upper panel of Fig. 6 shows the comparison between N(SiO) and $N(H_2)$ for 73 sources observed in this survey (marked by circles), 261 dust clump sources hosting different evolutionary stages of massive stars (triangles) (Csengeri et al. 2016a), and 24 starless clump candidates (diamonds and squares) (Zhu et al. 2020) in the 1.1 mm continuum Bolocam Galactic Plane Survey (Svoboda et al. 2016). As mentioned in the previous section, the uncertainties of N(SiO) indicated with error bars in Fig. 6 are determined by applying a T_{ex} range of 5 K as the lower limit and T_{dust} as the upper limit for cases with available T_{dust} from the ATLASGAL catalog (Urquhart et al. 2018, 2022). N(SiO) trends to increase as $N(H_2)$ increases, while these column densities do not show any association with the evolutionary stages as indicated by the temperatures.

The plot in the lower panel of Fig. 6 shows the comparison of X(SiO) and the ratio of bolometric luminosity and clump mass (L_{bol}/M_{clump}) with dust temperature in color, for sources mentioned above. The abundance uncertainties, represented by the error bars, are derived from the upper and lower N(SiO) limits, while maintaining a constant $N(H_2)$. Therefore, as previously indicated, these X(SiO) values serve as lower limits. The SiO abundances do not have any correlation with evolutionary stages. The lack of correlation between X(SiO) and L_{bol}/M_{clump} is also found toward the data points from the other SiO surveys with no dependency of the observed transitions. All the surveys used here adopt the excitation temperature of 10 K for SiO 1 – 0 and 2 – 1 transitions. To compare with our observations, we use the dust properties from Urquhart et al. (2018, 2022) to avoid any biased results due to applying different assumptions. Csengeri et al. (2016a) and Zhu et al. (2020) estimate $N(H_2)$ with different assumptions. Csengeri et al. (2016a) shows a moderate correlation of X(SiO) with L_{bol}/M_{dust} in their work, but that is likely due to assuming 18 K for the dust temperature to calculate the $N(H_2)$ used in their work. As a result, the $N(H_2)$ estimated in Csengeri et al. (2016a) are likely underestimated for infrared dark clumps, and thus SiO abundances toward the cold sources are overestimated.

Zhu et al. (2020) also shows higher abundances in their analysis toward starless clump candidates, and their $N(H_2)$ column densities determined with NH_3 kinetic gas temperature

are smaller than the $N(H_2)$ from the ATLASGAL catalog. This causes higher abundances of SiO toward the starless clump candidates. If kinetic gas temperature and dust temperatures are out of thermal equilibrium, using the gas temperature also leads to less accurate clump properties. Zhu et al. (2020) also shows higher abundances in their analysis toward starless clump candidates, and their $N(H_2)$ column densities determined with NH_3 kinetic gas temperature are smaller than the $N(H_2)$ from the ATLASGAL catalog. This causes higher abundances of SiO toward the starless clump candidates. If the kinetic gas temperature and dust temperatures are out of thermal equilibrium, using the gas temperature also leads to less accurate clump properties. Therefore, for all sources of these three surveys (Csengeri et al. 2016a, Zhu et al. 2020 and this work), with ATLASGAL counterparts, we used $N(H_2)$ taken from Urquhart et al. (2018, 2022) because the $N(H_2)$ were estimated with dust temperatures determined by fitting spectral energy distributions of mid- and far-infrared continuum data with individual cold greybody and warm blackbody functions (see König et al. 2017 for details). The lower panel of Fig. 6 shows that when using a uniform $N(H_2)$ data the gradient in abundance disappears.

We also notice that toward sources with $T_{dust} < 20$ K, X(SiO) determined in our study ($J = 1 - 0$, circle markers) and by Zhu et al. (2020) ($J = 1 - 0$, diamond markers) tend to be higher than Csengeri et al. (2011b) ($J = 2 - 1$, triangle markers) and Zhu et al. (2020) ($J = 2 - 1$, square markers). The origin of the difference between the $J = 1 - 0$ and $J = 2 - 1$ is unclear. The fixed excitation temperature to 10 K for SiO toward all the sources can affect the distribution of X(SiO). Until the lines attain thermalization for a given density, the $J = 2 - 1$ transition exhibits a lower T_{ex} compared to the $J = 1 - 0$ transition, though this is unlikely to be the sole explanation. Decreasing T_{ex} to 5 K results in a 7% reduction in the inferred SiO column density from the 2 – 1 line, while further reducing T_{ex} to 3 K would be required to raise the column density by 30%. The observed discrepancy between the two transitions may be influenced by the distinct beam sizes employed for the 1 – 0 ($\sim 61''$) and 2 – 1 ($\sim 31''$) transitions. Consequently, the higher column densities of SiO derived from the 1 – 0 transition could imply that the SiO emission exhibits spatial extension beyond the region probed by the 2 – 1 transition.

By using the same data set for the clump properties for the three SiO surveys compared here, we find that X(SiO) does not show any apparent correlation with L_{bol}/M_{clump} which indicate the evolutionary stage of clumps. This is consistent with the findings from previous observations (e.g., Liu et al. 2022). With potential uncertainty for the SiO excitation temperature, Csengeri et al. (2016a) also conclude that there are no clear trends in SiO abundances compared with the evolutionary stages. We also find that distributions of all three surveys (i.e., this survey, Csengeri et al. 2016a, and Zhu et al. 2020) show significant variations in SiO abundance across the samples of objects. The median X(SiO) toward all the samples is about 10^{-10} that is consistent with SiO abundances measured toward narrow and extended SiO emission regions toward IRDCs and low-velocity ($v_s \sim$ 10–15 km s^{-1}) shocked areas (e.g., Duarte-Cabral et al. 2014; Jiménez-Serra et al. 2010; Cosentino et al. 2020) but smaller than SiO abundances $\geq 10^{-8} - 10^{-9}$, determined with SiO emission from outflow sources and high-velocity regimes of SiO emission in low- and high-mass star-forming regions (e.g., Jiménez-Serra et al. 2005, 2010; Sánchez-Monge et al. 2013; Duarte-Cabral et al. 2014; López-Sepulcre et al. 2016).

The upper panel of Fig. 7 shows the comparison between SiO luminosity and bolometric luminosity toward the three SiO surveys. Using a partial-spearman ρ-rank correlation, which takes into account the influence of distance on the outcome, to all the data points, the distribution shows a moderate correlation (partial-$\rho_s = 0.44^{+0.08}_{-0.08}$) between the two parameters as higher L_{SiO} sources trend to be associated with higher L_{bol}. In addition, at a given L_{bol}, sources with T_{dust} lower than 20 K have brighter SiO luminosity compared with other sources with $T_{dust} \geq 20$ K.

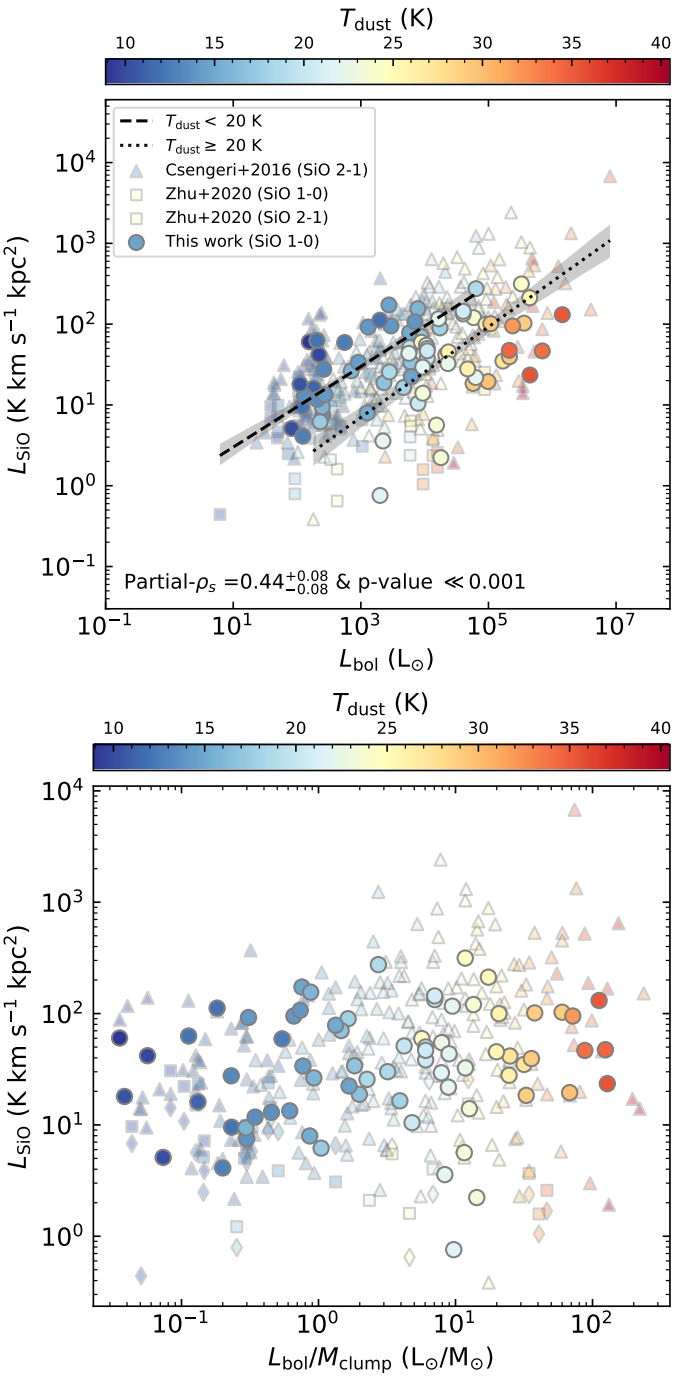

Fig. 7: *Upper*: Bolometric luminosity (L_{bol}) versus SiO luminosity (L_{SiO}). The dashed and dotted lines are the best fits for sources with temperatures < 20 K and > 20 K, respectively. The gray shaded regions represent 2σ confidence intervals for the best fits. *Lower*: The bolometric luminosity over clump mass versus SiO luminosity. The markers are as same as Fig.6. The colour bars for both the plots present dust temperature.

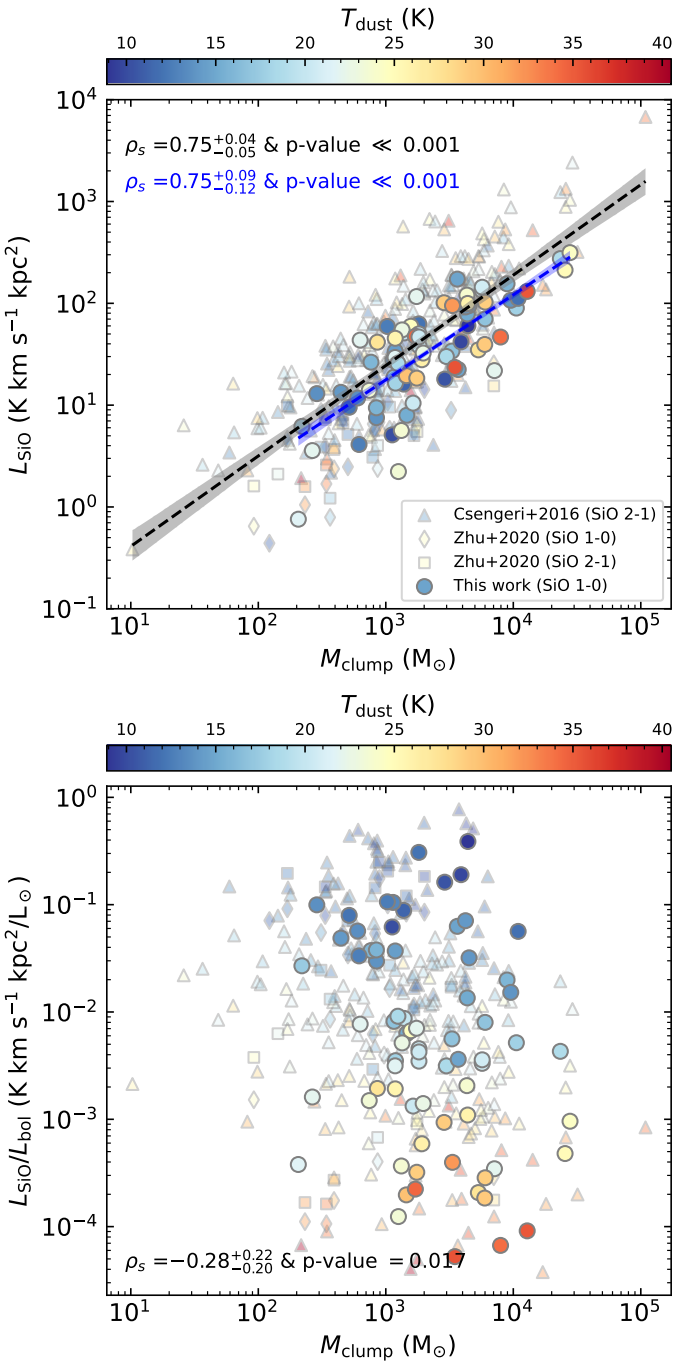

Fig. 8: *Upper*: Comparison of SiO luminosity and clump mass. *Lower*: L_{SiO}/L_{bol} versus L_{bol}/M_{clump}. The markers are as same as Fig. 6. The colour bars for both the panels present dust temperature. The dashed black and blue lines in the upper panel are the best fits to data points of three surveys and only our survey, respectively. The gray and blue shaded regions present 2σ confidence intervals for the best fits matched with the same colors.

The dashed and dotted lines are the best fits of linear regression to the sources with T_{dust} colder or hotter than 20 K, respectively. The gray areas indicate the 2σ confidence interval of uncertainties for the best fits. These uncertainties are estimated by iteratively performing linear regression fitting randomly resampled data sets of the applied sample. It seems that SiO luminosity for sources of a given bolometric luminosity is greater by a factor of ∼ 7 for sources with dust temperatures less than 20 K.

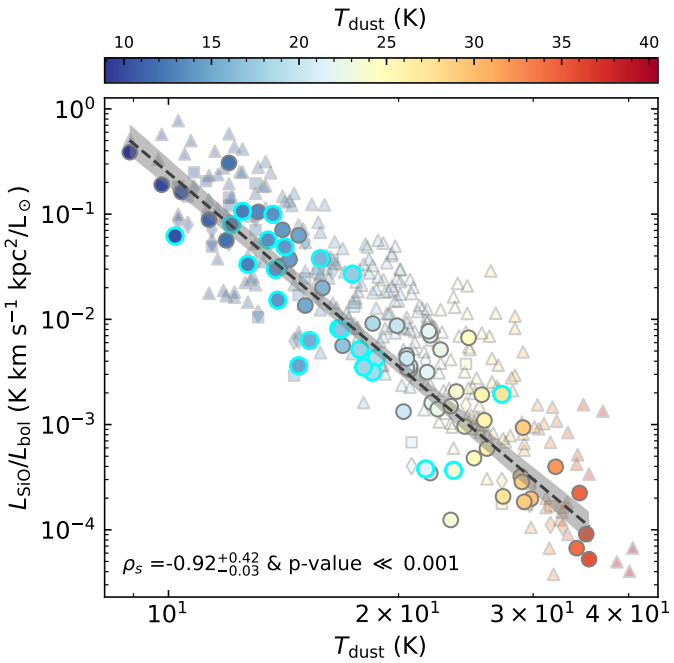

Fig. 9: Comparison of L_{SiO}/L_{bol} and T_{dust} toward sources with available T_{dust} and L_{bol}. The colour bar shows dust temperature. Black dashed line is the best fit to data points from this study, and the gray shaded region presents the 2σ confidence intervals for the best fit. Sources without SiO wing features are indicated by open cyan circles. The symbols are same as in Figs.7 and 8

.

However, the excess SiO luminosity is not relevant to the evolutionary stage of the embedded objects or the clumps as estimated by L_{bol}/M_{clump} as we do not find any correlation in the comparison of L_{SiO} and L_{bol}/M_{clump} plotted in the lower panel of Fig. 7. Liu et al. (2022) also did not find a trend in the comparison between L_{SiO} and L_{bol}/M_{clump} for SiO (2 – 1) toward 171 massive star-forming clumps from the ALMA ACA observations, which have higher angular resolutions (∼ 13.5″) than this survey. Their colder clumps also have a higher SiO luminosity at a given bolometric luminosity. This might imply that there could be additional formation mechanisms to release SiO in the gas phase from dust grains, for example, via low-velocity shocks (Jiménez-Serra et al. 2008) apart from stronger/fast shocks from outflows or/and jets releasing SiO from dust cores (Schilke et al. 1997; Gusdorf et al. 2008).

In Fig. 8, the upper panel shows L_{SiO} versus M_{clump}. The SiO luminosities estimated over the beam size show the excellent correlations, with masses of the associated dust clumps for both cases including all the three surveys (black dashed line and gray shade region) or only our survey (blue dashed line and blue shade region) with a significant spearman ρ-rank coefficient of $0.75^{+0.04}_{-0.05}$ with $p-$value $\ll 3\sigma$. In contrast to the plot of L_{SiO} versus L_{bol}, there is no gradient in dust temperature observed in this comparison of mass and SiO luminosity. The lower panel of Fig. 8 shows the comparison of L_{SiO}/L_{bol} versus M_{clump} indicating no obvious correlation as spearman ρ-rank coefficient of $-0.28^{+0.22}_{-0.20}$ ($p-$value of 0.017) is not significant. As found in the lower panel of Fig. 7 showing no trend with evolutionary stages of embedded sources, we also see no correlation between the clump mass and the dust temperature. Figure 9 shows that L_{SiO}/L_{bol} has a significant correlation (ρ_s =$0.92^{+0.42}_{-0.03}$ with $p-$value $\ll$0.001) with T_{dust} indicating the evolutionary stages

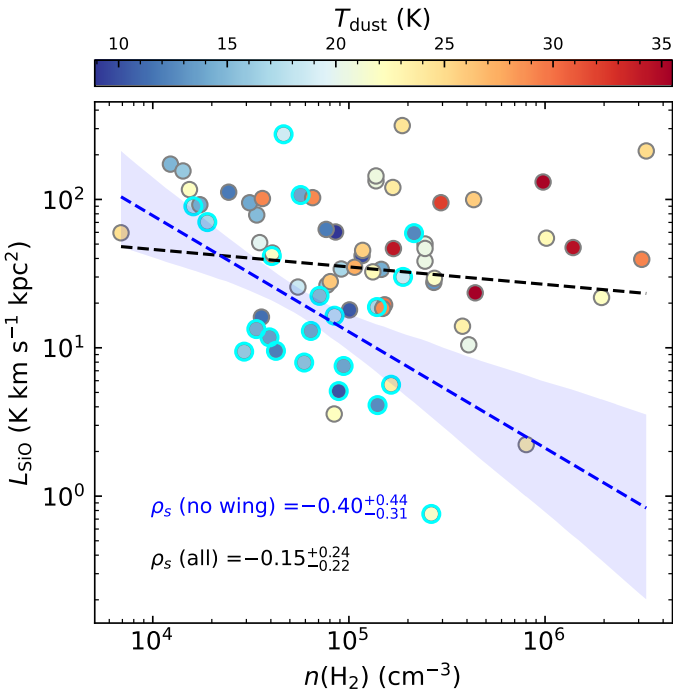

Fig. 10: *Upper*: Comparison of L_{SiO} and $n(H_2)$ toward sources having $n(H_2)$ parameter available. *Lower*: Comparison of L_{SiO}/L_{bol} and $n(H_2)$ toward sources having $n(H_2)$ and L_{bol} parameters. The colour bars for both the panels present dust temperature. The black and blue dashed lines in the upper panel are the best fits to data points with SiO wings or without. The blue shaded region presents 2σ confidence intervals for the best fit for non-SiO wing sources indicated by open cyan circles. The markers are same as for Figs.7 and 8.

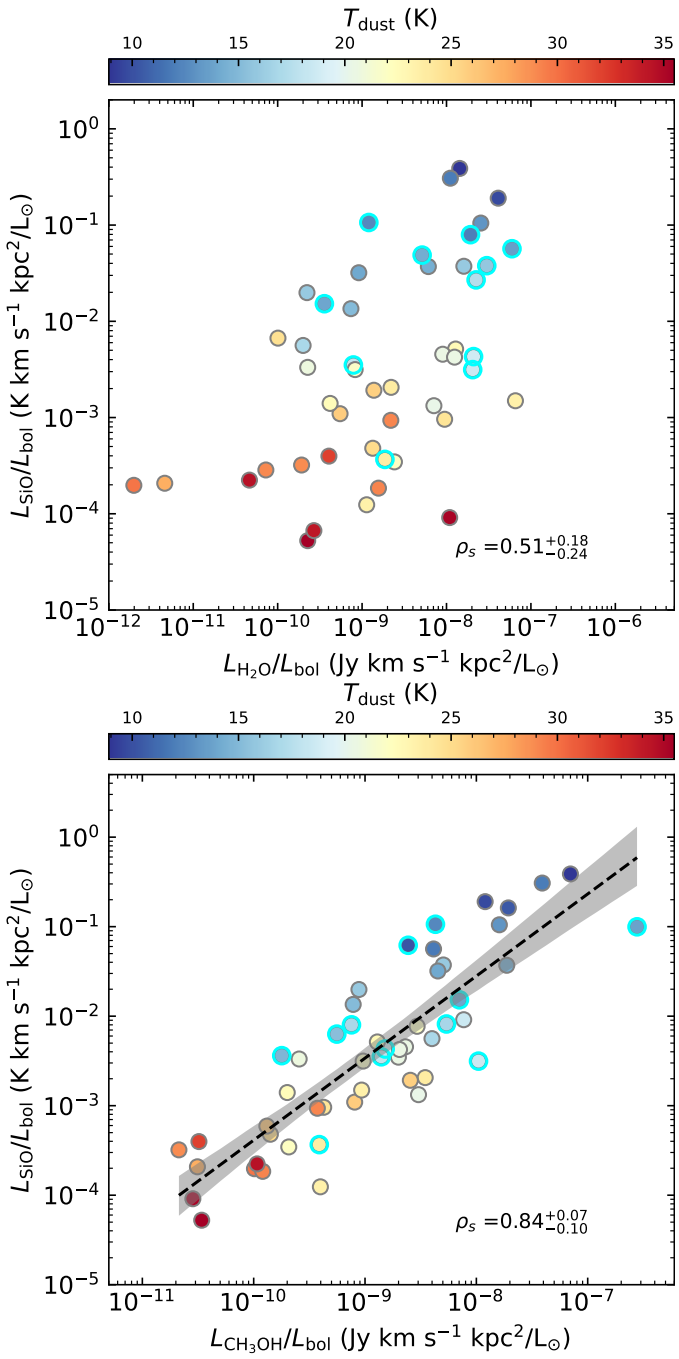

Fig. 11: L_{SiO}/L_{bol} versus ratios of 22 GHz H_2O (*upper*) maser and Class I CH_3OH maser luminosities (*lower*) and L_{bol} toward sources with both detections of SiO and masers. The colors indicate dust temperatures. The black dashed lines and gray shade regions are the best-fit and the 95 % confidence intervals of fitting. The cyan open circles indicate sources considered to show no significant sign of SiO wings.

of associated dust clumps. We find that L_{SiO}/L_{bol} is clearly larger toward colder ($T_{dust} < 20$ K) clumps at a given clump mass.

To distinguish SiO emission caused by ongoing star-forming activities (i.e., outflows or jets), we divide SiO emission sources into two groups based on four classifications of SiO emission features for SiO 1 – 0 and 2 – 1 transitions, from this survey and Csengeri et al. (2016a), respectively. In the SiO detection column of Table 1, sources marked with *e* indicating no sign of wing features in either $J = 1 - 0$ or $J = 2 - 1$ transitions with a narrow Δv_{FWHM} <8 km s^{-1} are classified as non-wing SiO sources, in other words, which are narrow line SiO sources. The other cases with SiO wing features or/and broad SiO line with Δv_{FWHM} ≥8 km s^{-1} are considered SiO wing sources. The narrow SiO emission marked with cyan circles in Fig. 9 are tightly

associated with cold clumps, which also have large L_{SiO}/L_{bol} ratios. We will discuss the physical properties of these narrow SiO sources in detail in the following section (Sect. 4.3).

Figure 10 shows comparisons of the volume density of molecular hydrogen and SiO luminosity (in the upper panel) and L_{SiO}/L_{bol} (in the lower panel). For all the sources in the upper panel plot, we find no correlation ($\rho_s = -0.15^{+0.24}_{-0.22}$) between L_{SiO} and $n(H_2)$, and the linear-regression fit is the black dashed line. However, interestingly, the narrow SiO sources marked with open cyan circles are mainly located in the lower envelope of the distribution and show a moderate correlation of $-0.40^{+0.44}_{-0.31}$. The linear regression best fit is the blue dashed line, and its 2σ confidence intervals are indicated in the blue shaded area.

In the lower panel plot of L_{SiO}/L_{bol} versus $n(H_2)$, we see a slightly better correlation with $\rho_s = -0.56^{+0.18}_{-0.14}$. Although the range of volume density is small, it is clear that lower volume density regions have higher SiO luminosity relative to L_{bol}. In general, we expect lower $n(H_2)$ toward early evolutionary stages due to longer free-fall times, while more evolved stages trend to have high $n(H_2)$ and corresponding shorter free-fall times (Urquhart et al. 2018, 2022). The lower panel of Fig. 10 also shows trend as clumps with colder T_{dust} are mainly distributed toward $n(H_2) < 10^5$ cm^{-3}. However, at $n(H_2)$ around 10^5 cm^{-3}, both colder and hotter clumps exist. Nevertheless, it is significant that narrow SiO emission lines are often detected toward clumps with $T_{dust} < 20$ K and $n(H_2) < 10^5$ cm^{-3}, and these clumps tend to have $L_{SiO}/L_{bol} > 10^{-3}$ km s^{-1} kpc^2/L$_\odot$. Duarte-Cabral et al. (2014) and Csengeri et al. (2016a) suggest that narrow SiO emission sources without any bright infrared sources might trace the earliest phase of molecular clouds undergoing global-infalling processes or converging flows on clouds. Here we find high relative SiO luminosity to L_{bol} toward sources with $T_{dust} < 20$ K and $n(H_2) < 10^5$ cm^{-3}, with most of them showing narrow SiO emission. This trend might suggest that those narrow SiO sources or high L_{SiO}/L_{bol} sources observed in this survey are experiencing large-scale infall processes. If this suggestion is correct, it can explain why we see higher SiO luminosity toward sources with colder dust temperatures, mainly associated with IRDC sources.

4.2. Comparisons with 22 GHz H_2O and 44 GHz Class I CH_3OH maser emission

All of the positions observed for SiO (1 – 0) were also observed for 22 GHz H_2O and 44 GHz Class I CH_3OH masers with the KVN telescopes. We recalculate the luminosities of both the maser species with the same distances used for the SiO luminosities, and these are listed in Tables 4 and C.4. Figure 11 shows the comparisons of SiO and masers luminosities normalized by bolometric luminosity as L_{SiO}/L_{bol} tends to vary with evolutionary stages (e.g., shown in the lower panel of Fig. 10). Felli et al. (1992) show a strong correlation between L_{H_2O} and the mechanical luminosity of outflows in CO emission, which is proportional to the bolometric luminosity measured at submillimeter/far-infrared wavelengths. This indicates that H_2O masers are strongly associated with outflow sources. H_2O maser luminosities presented in this study, as shown, however, show a moderate correlation with SiO luminosities with the spearman correlation coefficient of $0.51^{+0.18}_{-0.24}$ and p-value $\ll 0.001$). In addition, Duarte-Cabral et al. (2014) show that L_{SiO} estimated for individual outflow sources correlate well with the respective CO outflow momentum flux (F_{CO}). However, when they compare the SiO luminosities obtained over entire fields including outflows and ambient gas regions, in which the observations do not resolve individual outflow sources, with the F_{CO} and find no correlation between SiO emission and CO flux powered by outflows. This is consistent with the lack of a significant correlation that we see between L_{SiO}/L_{bol} and L_{H_2O}/L_{bol}.

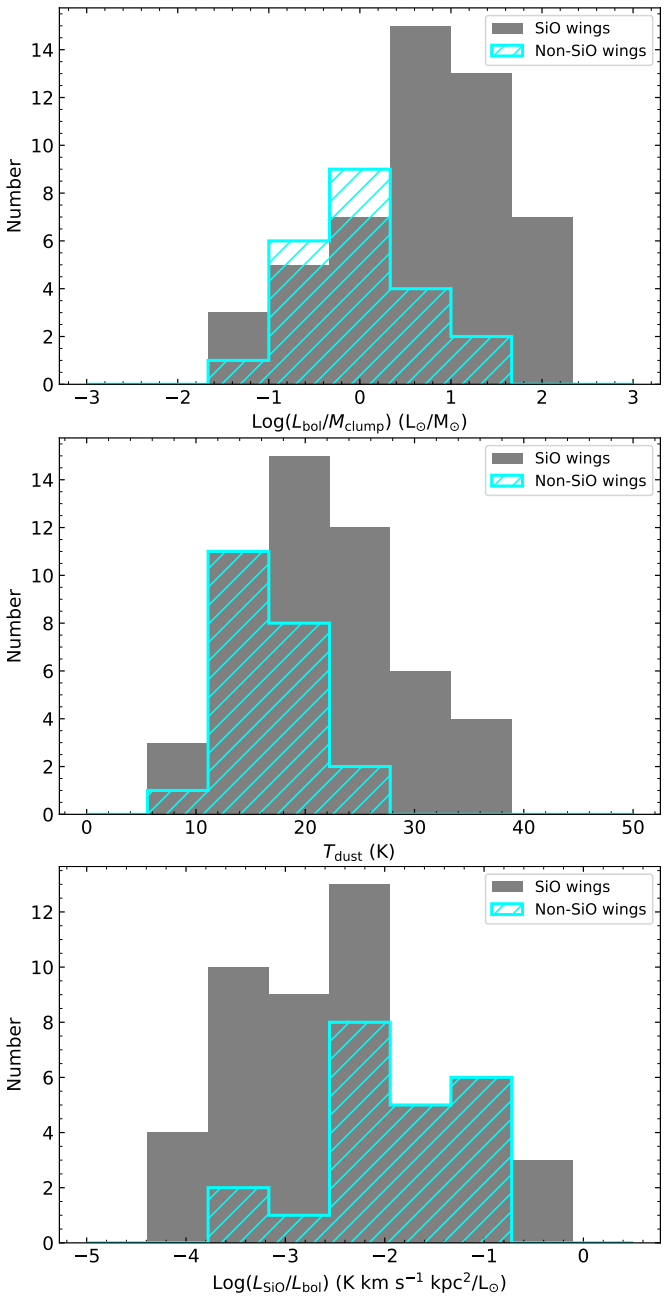

Fig. 12: Histograms of Log(L_{bol}/M_{clump}), T_{dust} Log(L_{SiO}/L_{bol}) from top to bottom. The cyan histograms represent the distributions of sources without SiO wing features (non-wing sources) while the gray histograms are SiO wing sources.

The scatter plot for L_{SiO}/L_{bol} versus L_{CH_3OH}/L_{bol} in the lower panel of Fig. 11 shows a significant correlation. The spearman ρ-rank efficient is $0.84^{+0.07}_{-0.10}$ with a small p-value $\ll 0.001$. Such the strong correlation indicates that SiO and Class I 44 GHz CH_3OH maser trace similar properties of shocked gas toward these massive star-forming regions. We also find that SiO luminosity is strongly correlated with clump mass shown in the left panel of Fig. 8.

The 22 GHz H_2O and Class I 44 GHz CH_3OH masers are known to be collisionally pumped by mainly outflows (Felli et al.

Table 5: Physical properties toward sources with the presence of SiO wings.

	SiO wing source				Non-wing SiO source			
	#	Mean	Median	Standard deviation	#	Mean	Median	Standard deviation
$N(H_2)$ [cm^{-2}]	51	1.48×10^{23}	1.02×10^{23}	1.55×10^{23}	22	6.08×10^{22}	5.68×10^{22}	3.24×10^{22}
N(SiO) [cm^{-2}]	66	1.49×10^{13}	1.07×10^{13}	1.23×10^{13}	38	6.22×10^{12}	5.93×10^{12}	2.76×10^{12}
X(SiO)	51	1.96×10^{-10}	1.29×10^{-10}	3.59×10^{-10}	22	1.13×10^{-10}	1.01×10^{-10}	4.18×10^{-11}
T_{dust} [K]	51	21.6	21.9	6.8	22	16.3	15.6	3.9
Log (L_{bol}) [L$_\odot$]	50	5.03	4.04	5.38	22	3.87	3.21	4.14
Log (M_{clump}) [M$_\odot$]	50	3.63	3.38	3.72	22	3.50	3.03	3.72
$n(H_2)$ [cm^{-3}]	51	5.27×10^{5}	1.37×10^{5}	1.30×10^{6}	21	9.02×10^{4}	6.40×10^{4}	6.74×10^{4}
Log (L_{bol}/M_{clump}) [L$_\odot$/M$_\odot$]	50	1.32	0.90	1.51	22	0.49	−0.02	0.75
Log (L_{SiO}/L_{bol}) [K km s^{-1}kpc^2/L$_\odot$]	50	−1.48	−2.47	−1.12	22	−1.54	−1.93	−1.49
L_{H_2O}/L_{bol}	37	7.00×10^{-9}	1.34×10^{-9}	1.29×10^{-8}	11	1.66×10^{-8}	1.93×10^{-8}	1.71×10^{-8}
L_{CH_3OH}/L_{bol}	40	5.68×10^{-9}	9.47×10^{-10}	1.27×10^{-8}	12	2.60×10^{-8}	1.98×10^{-9}	7.59×10^{-8}

1992; Kurtz et al. 2004), but for some cases, Class I CH_3OH masers are excited by expanding ionized gas (Voronkov et al. 2010, 2014; Gómez-Ruiz et al. 2016) or cloud-cloud collisions (Haschick & Baan 1993; Sato et al. 2000). The processes collisionally exciting Class I CH_3OH maser can release SiO as well as possibly Si into the gas phase from icy mantles of dust grains/cores. This probably explains the tight correlation between Class I CH_3OH maser and SiO emission shown in Fig. 11.

We also note that potentially the inclusion of thermal or quasi-thermal emission in the 44 GHz CH_3OH luminosity estimate might contribute to the scatter shown in the shaded gray area in the lower panel of Fig. 11. For H_2O maser (the upper panel), it unexpectedly shows much larger scatters with less correlation between the H_2O maser and SiO emission. In general, outflows could be the primary origin of producing SiO and exciting H_2O maser transition but as mentioned earlier, SiO can be produced by other processes. This might cause the large scatter between the SiO and H_2O emission.

4.3. Association with the presence of SiO wing features

Table 5 lists mean, median, and standard deviation values of physical parameters toward sources with SiO wings and without them. M_{clump} shows no differences between the two groups. On the other hand, the mean and median values for Log (L_{bol}/M_{clump}), T_{dust}, and Log (L_{SiO}/L_{bol}), which are all of traces of evolution, are apparently different with the presence of SiO wing features. We do not find any siginicant differences in H_2, SiO column densities, and X(SiO) between SiO wing and non-wing sources. Overall sources with SiO wings have higher luminosity than non-wing sources by a factor 7 – 14 (depending on whether considering the median or mean L_{bol}).

Figure 12 shows histograms of those parameter ratios for sources with SiO wings (in gray color) and without them (in cyan color). To distinguish significant differences in these physical parameters as well as T_{dust} between SiO wing sources and non-wing sources, we performed KS-tests on L_{bol}/M_{clump}, T_{dust}, and L_{SiO}/L_{bol} where we find some differences in their mean and median values. According the KS-tests, we can strongly reject the null hypothesise, which is that the two group represent the same sample, for L_{bol}/M_{clump} and T_{dust} with small $p-$values $\ll 0.001$. For L_{SiO}/L_{bol}, comparing the two groups gives a $p-$value of 0.04 and so can be rejected at the 0.95 confidence level ($2\,\sigma$). Therefore, the sources with no apparent SiO wing features may tend to be associated with less evolved clumps indicated by lower L_{bol}/M_{clump} and lower T_{dust}, whereas their L_{SiO}/L_{bol} are higher than those of sources with SiO wings.

Several studies (e.g., Motte et al. 2007; Sakai et al. 2010) report bright SiO emission toward less evolved sources (i.e., mid-infrared dark). We also find the trend toward our sources showing bright SiO emission toward colder and younger sources. However, some of them do not show high-velocity SiO emission, and their SiO lines have relatively narrow line widths ($\Delta v_{FWHM} < 8$ km s^{-1}). This may imply that the SiO emission toward the sources with no wings are associated with low-velocity shock processes, such as cloud-cloud collision (Cosentino et al. 2020; Armijos-Abendaño et al. 2020) or converging flow/global-infalling flow (Jiménez-Serra et al. 2010; Duarte-Cabral et al. 2014; Csengeri et al. 2016a), to release the SiO into the gas-phase.

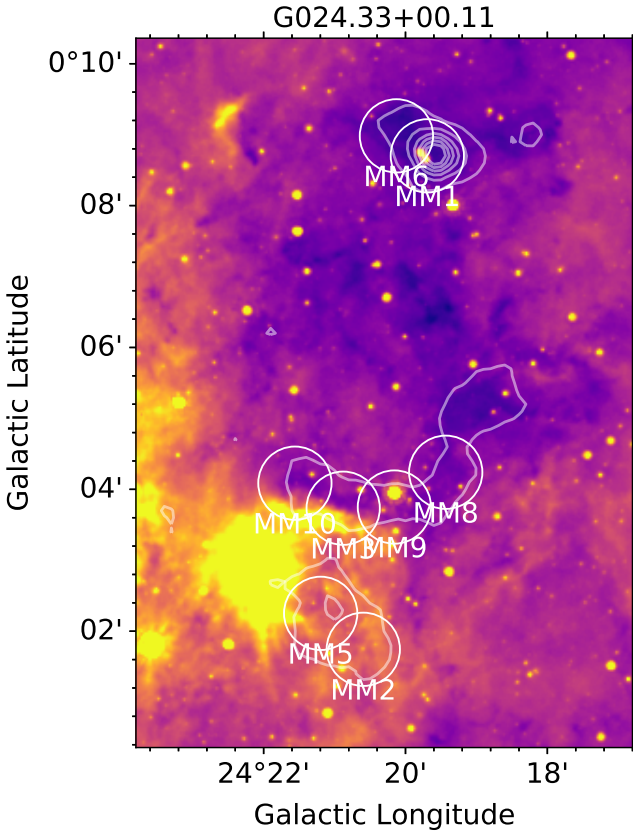

Fig. 13: GLIMPSE IRAC 8 μm image in color toward G024.33+00.11, with the dust emission at 870 μm, in gray contours. The white circles indicate the beam of KVN observations toward target sources.

4.4. The origin of SiO emission

Many sources observed in this survey host bright infrared objects, such as HMPOs and UCHIIs that are selected with infrared colors (Wood & Churchwell 1989b; Molinari et al. 1996; Rathborne et al. 2006). Some sources of the IRDCs have compact point sources at 4.5 μm and 8 μm wavelengths (Chambers et al. 2009). The detected SiO emission may originate from ongoing star-forming activity, such as outflows or jets from embedded sources. We have found 66 sources (18 UCHIIs, 15 HMPOs, and 33 IRDC cores) showing SiO wing features or broad SiO lines ($\Delta v_{\rm FWHM} > 8\,{\rm km\,s^{-1}}$), and most of the sources seem to be more evolved sources with a median Log($L_{\rm bol}/M_{\rm clump}$) of 0.90 compared with those showing no SiO wing features (a median Log($L_{\rm bol}/M_{\rm clump}$) = −0.02). Broad SiO line width and wing features apparently indicate the presence of fast shock with the typical C-shock velocity (e.g., Gusdorf et al. 2008). However, we also find narrow SiO components toward bright infrared sources at 8 μm or/and 24 μm wavelengths. Lefloch et al. (1998) found widespread SiO emission toward NGC 1333, and they proposed that the SiO emission lines trace materials shocked by outflows, being diverted and decelerated by interacting with colder ambient clumps. This can produce narrow SiO emission lines due to the processes formed by fast-shocks and surrounding gas at a systemic velocity (Lefloch et al. 1998; Codella et al. 1999; Duarte-Cabral et al. 2014).

Some SiO-detected sources, however, do not have discernible infrared objects, and so they are classified as infrared quiescent sources in the ATLASGAL catalog or unidentified. Among those sources, narrow SiO emission lines are found toward eight sources: G023.60+00.00 MM7, G024.33+00.11 MM6, G024.33+00.11 MM2, G024.33+00.11 MM3, G024.33+00.11 MM10, G028.37+00.07 MM1, G028.37+00.07 MM16, and G031.97+00.07 MM8.

Within the IRDC G024.33+00.11, three sources (MM2, MM3, and MM10) showing narrow SiO lines are found in the same cloud. G024.33+00.11 MM2 is very close to another source, G024.33+00.11 MM5, which shows a slightly broad SiO emission profile. The other positions, G24.33+00.11 MM3 and MM10, are situated in the vicinity of a HII bubble (Simpson et al. 2012; Anderson et al. 2015) showing bright 8 μm emission presented in Fig. 13. It might be possible that their narrow SiO lines are produced by the photo-desorption of icy mantles of dust grains (Walmsley et al. 1999; Schilke et al. 2001). The SiO abundances relative to $N(H_2)$ obtained from PPMAP toward these four sources (MM2, MM3, MM5, and MM10 of G024.33+00.11) surrounding the HII bubble are range from $7.1\times10^{-11} - 3.85\times10^{-10}$ that are close to SiO abundances measured in translucent clouds ($\sim 10^{-11} - 10^{-10}$, Turner 1998) and in the Orion Bar PDR ($\sim 10^{-11}$, Schilke et al. 2001). However, N(SiO) and X(SiO) toward the MM2, MM3, MM5, MM10 regions also enter typical ranges of column density and abundance of SiO found in regions showing large-scale shocks (Jiménez-Serra et al. 2010) or cloud-cloud collision by the interaction between ambient colder gas and expanding HII regions (Colombo et al. 2019; Zhu et al. 2023) as all of the positions surround the 8 μm bright HII region (see Fig. 13).

G024.33+00.11 MM6 is close to MM1, hosting a young stellar object that likely has outflows. Thus, the SiO emission detected toward MM6 could be tracing the shocked gas interacting with potential outflows, and this might be the same for G028.37+00.07 MM1, which is close to the bright 8 μm source. However, G028.37+00.07 MM1 and G024.33+00.11 MM6 are separated by 0.64 – 1.12 pc from the outflow candidate sources. These IRDCs are relatively isolated from the other IRDCs in IRDC G024.33+00.11. If these narrow SiO emission are not associated with outflows, this could be explained by shocks associated with infalling material from massive dense clumps ($\geq 0.1-0.3$ pc) onto the core envelope scale (≤ 0.02 pc) or small-scale converging flows creating low-velocity shocks (Jiménez-Serra et al. 2010; Csengeri et al. 2011a,b; Nguyen-Lu'o'ng et al. 2013; Duarte-Cabral et al. 2014; Louvet et al. 2016).

Although we adopt a $\Delta v_{\rm FWHM}$ of 8 km s^{-1} as the threshold to divide sources into two groups, narrow (i.e., non-wing SiO) and broad (i.e., SiO wing) SiO emission sources, the value is still arbitrary, and in many previous studies, the definition of the line width for narrow SiO components are variable ($\Delta v_{\rm FWHM} < 1\,{\rm km\,s^{-1}}$ to $10 - 15\,{\rm km\,s^{-1}}$) (e.g., Jiménez-Serra et al. 2010; Lefloch et al. 1998; Cosentino et al. 2020; Duarte-Cabral et al. 2014; Csengeri et al. 2016a; Louvet et al. 2016; Nguyen-Lu'o'ng et al. 2013). In this survey, seven sources (G015.05+00.07 MM1, G023.60+00.00 MM4, G028.53−00.25 MM10, G034.43+00.24 MM5, G034.43+00.24 MM6, G034.43+00.24 MM7, and G034.43+00.24 MM8) with $\Delta v_{\rm FWHM} > 8\,{\rm km\,s^{-1}}$ and no significant wing features of SiO do not have any infrared counterpart or are classified as embedded sources in the ATLASGAL catalog.

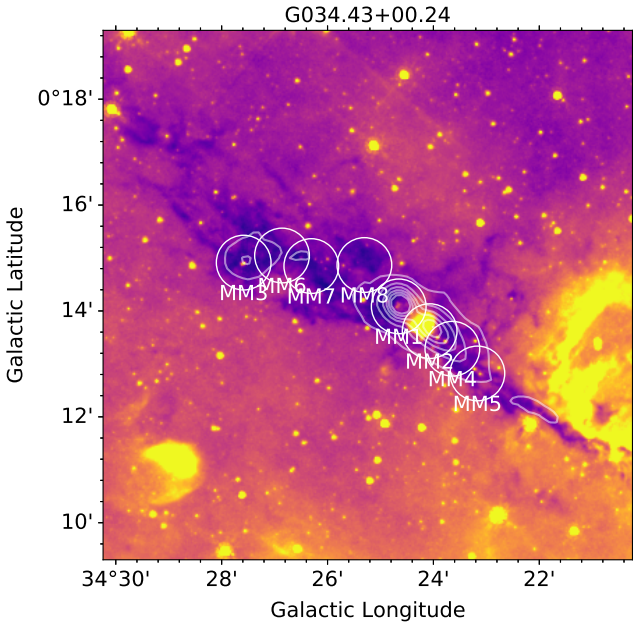

Fig. 14: GLIMPSE IRAC 8 μm image in color toward G034.43+00.24, with the dust emission at 870 μm, in gray contours. The white circles indicate the beam of KVN observations toward target sources.

Four positions out of the seven sources with SiO line width $\Delta v_{\rm FWHM} > 8\,{\rm km\,s^{-1}}$ without both SiO wing features and discernible embedded objects are located in the IRDC G034.43+00.24, these are MM5, MM6, MM7, and MM8 marked in Fig. 14. Those positions are located far from the outflow sources, that are MM1 which is known an extended green object (EGO G034.41+0.24, Cyganowski et al. 2008), MM2, and MM3, with separations of 0.64–0.86 pc. As seen in Fig. 14, these four positions clearly follow the high visual extinction region at 8 μm along the filamentary features. We find such cares toward other IRDCs for narrow SiO sources without embedded sources; G015.05+00.07 MM1, G023.60+00.00 MM4, G023.60+00.00 MM7, G028.37+00.07 MM1, G028.37+00.07

MM16, G028.53−00.25 MM10, and G031.97+00.07 MM8. In cold and dense environments, Si is unlikely to be in the gas phase because of depletion back onto the icy grain mantles or oxidization forming SiO_2, which itself is also eventually depleted to the ice mantle of dust grains. This leads to the relatively short lifetime of SiO in the gas phase in about $\sim 10^4$ yr (Martin-Pintado et al. 1992; Gusdorf et al. 2008). According to Nguyen-Lu'o'ng et al. (2013) and Duarte-Cabral et al. (2014), converging flow from diffuse interstellar mediums containing pre-existing SiO in the gas phase into massive dense clumps provide low-velocity shocks with v_s of 5 km s^{-1} that could preserve the abundance of SiO above the typical abundance of $< 10^{-12}$ in low-mass dense cores (Ziurys et al. 1989). Toward some diffuse and translucent clouds (e.g., Turner 1998; Rybarczyk et al. 2023), absorption observations show that SiO can already exist in the gas phase from diffuse environments. In addition, Guillet et al. (2011), Caselli et al. (1997) and Jiménez-Serra et al. (2008) show that low-velocity shocks about 10 – 15 km s^{-1} can produce SiO in the gas-phase through sputtering for evaporation of the grain mantle ices caused by grain-grain collisions or desorbing Si in the gas phase if a fraction of Si exits in the grain ice mantles. Such low-velocity shocks can be created by cloud-cloud collisions, infalling materials, or converging flows.

Our survey shows that narrow SiO without wing features are commonly detected toward IRDCs. However, this could be due to an observational bias because we observed more positions in the IRDCs than toward HMPOs and UCHIIs. We note that the large number of detections toward IRDCs are not due to their distances as their detection distribution in distance is not significantly different from those of HMPOs and UCHIIs. Therefore, it is hard to conclude that narrow SiO emission features appear to be related to a particular type of cloud, for example, IRDCs. If we only consider sources having ATLASGAL counterparts, we can discern that narrow SiO sources with no wings are associated with younger and colder dust clumps. This supports the suggestions proposed in previous studies that narrow and widespread SiO emission lines toward molecular clumps with a lack of star-forming activity seem to be originated from cloud formation processes producing low-velocity shocks (10 – 15 km s^{-1}) and to trace the early phase of molecular cloud evolution (Duarte-Cabral et al. 2014; Csengeri et al. 2016a).

5. Summary

We carried out a survey of 43 GHz SiO ($J = 1 - 0$) emission toward 366 massive star-forming regions consisting of different evolutionary stages of massive stars, including infrared dark cloud cores, outflow candidates of high mass young stellar objects, and ultracompact HII regions, with the KVN 21 m telescopes. The main results are:

- We detected SiO (1 – 0) emission toward 106 positions (59 IRDC cores, 21 HMPOs, and 26 UCHIIs), however, two sources out of the 59 IRDC cores are excluded from further analysis as the beam significantly overlaps with two sources with stronger SiO emission. We divide the 104 sources into two groups by line profile and $\Delta v_{\rm FWHM}$; 66 out of 104 sources are considered as non-wing SiO group because these sources do not have wing features at high-velocities in SiO (1 – 0) or/and (2 – 1) or/and $\Delta v_{\rm FWHM}$ of their SiO spectra are narrower than 8 km s^{-1}. The remaining 38 sources have either high-velocity wing features in SiO 1 – 0 or 2 – 1 or/and their $\Delta v_{\rm FWHM}$ is broader than 8 km s^{-1}(the median width of all the fitted components) . We show that 72 (69%) and 81 (78%) sources have 22 GHz H_2O and 44 GHz Class I CH_3OH masers, respectively. By comparing physical properties of the dust clumps with SiO detection and non-detections, we show that the dust clumps with SiO emission are more massive (median Log ($M_{\rm clump}$) = 3.26) and colder (median $T_{\rm dust}$ = 20 K) than the clumps without SiO emission.
- The range of the beam-averaged SiO column density is $2.18 \times 10^{12} - 7.92 \times 10^{13}$ cm^{-2}, and the median is 8.12×10^{12} cm^{-2}. The median and mean X(SiO) relative to $N(H_2)$ taken from the ATLASGAL catalog are 1.28×10^{-10} and 1.71×10^{-10}, respectively. N(SiO) shows a good correlation with $N(H_2)$, but X(SiO) does not show any strong correlation with the clump evolutionary stage as measured by the clump luminosity to mass ratio. We also find that for lower dust temperature sources, the SiO column density and abundance determined from SiO 1 – 0 are $\sim$ 3 times higher than those obtained from SiO 2 – 1 surveys. We find that less evolved sources (those with lower dust temperatures) tend to have higher $L_{\rm SiO}/L_{\rm bol}$ ratio by a factor of ~7 compared with higher temperature sources. $L_{\rm SiO}$ is also very well correlated with the clump dust mass.
- We have compared $L_{\rm SiO}/L_{\rm bol}$ with $L_{\rm H_2O}/L_{\rm bol}$ and $L_{\rm CH_3OH}/L_{\rm bol}$ toward H_2O and CH_3OH maser detected sources, respectively. We find that SiO does not seem to be correlated with H_2O, although both transitions are known as outflow tracers. However, the SiO luminosity correlates well with CH_3OH luminosity, which itself is also well correlated with clump mass. These two molecules occur on dust grains and are released from the dust icy mantles or grain cores. Thus, it seems that toward our sources, the SiO and Class I CH_3OH maser emission might result from the related shocks.
- Toward sources with outflow candidates, embedded young stellar objects or UCHIIs, the detected SiO emission may be associated with outflows or jets as many of them show wing features at high-velocities and/or broader $\Delta v_{\rm FWHM}$ (> 8 km s^{-1}). However, the origin of SiO emission toward infrared dark sources and sources without clear embedded young stellar objects is unclear. The majority of these sources have narrow SiO emission, and even if a SiO line width is broader than 8 km s^{-1}, there are no clear embedded sources, and the observed positions can be situated far from bright infrared sources by 0.64 – 1.12 pc. In addition, we show that the SiO emission is can be widely spread over infrared clouds, not concentrated in a small area. Such cases might be associated with other mechanisms with low-velocity shocks ($v_s \sim 5 - 15$ km s^{-1}). Cloud-cloud collisions, infalling material onto massive dense clumps, or converging flows from diffuse clouds toward dense molecular clouds are candidates for such low-velocity shock resources.

Acknowledgements. We would like to thank the referee for their constructive comments and suggestions that have helped to improve this article. We are grateful to all staff members in Korean VLBI Network (KVN) who helped to operate the array and to correlate the data. The KVN is a facility operated by Korea Astronomy and Space Science Institute (KASI). W.-J. Kim was supported by DLR/Verbundforschung Astronomie und Astrophysik Grant 50 OR 2007 for this work. G.A.F acknowledges support from the Universität zu Köln and its Global Faculty Program.

References

Anderson, L. D., Armentrout, W. P., Johnstone, B. M., et al. 2015, ApJS, 221, 26
Armijos-Abendaño, J., Banda-Barragán, W. E., Martín-Pintado, J., et al. 2020, MNRAS, 499, 4918
Beuther, H., Schilke, P., Menten, K. M., et al. 2002, ApJ, 566, 945

Bronfman, L., Nyman, L. A., & May, J. 1996, A&AS, 115, 81
Carral, P., Kurtz, S., Rodríguez, L. F., et al. 1999, Rev. Mexicana Astron. Astrofis., 35, 97
Caselli, P., Hartquist, T. W., & Havnes, O. 1997, A&A, 322, 296
Chambers, E. T., Jackson, J. M., Rathborne, J. M., & Simon, R. 2009, ApJS, 181, 360
Chira, R. A., Beuther, H., Linz, H., et al. 2013, A&A, 552, A40
Churchwell, E., Walmsley, C. M., & Cesaroni, R. 1990, A&AS, 83, 119
Codella, C., Bachiller, R., & Reipurth, B. 1999, A&A, 343, 585
Colombo, D., Rosolowsky, E., Duarte-Cabral, A., et al. 2019, MNRAS, 483, 4291
Cosentino, G., Jiménez-Serra, I., Caselli, P., et al. 2019, ApJ, 881, L42
Cosentino, G., Jiménez-Serra, I., Henshaw, J. D., et al. 2020, MNRAS, 499, 1666
Cosentino, G., Jiménez-Serra, I., Tan, J. C., et al. 2022, MNRAS, 511, 953
Csengeri, T., Bontemps, S., Schneider, N., Motte, F., & Dib, S. 2011a, A&A, 527, A135
Csengeri, T., Bontemps, S., Schneider, N., et al. 2011b, ApJ, 740, L5
Csengeri, T., Bontemps, S., Wyrowski, F., et al. 2017, A&A, 601, A60
Csengeri, T., Leurini, S., Wyrowski, F., et al. 2016a, A&A, 586, A149
Csengeri, T., Weiss, A., Wyrowski, F., et al. 2016b, A&A, 585, A104
Cyganowski, C. J., Whitney, B. A., Holden, E., et al. 2008, AJ, 136, 2391
Duarte-Cabral, A., Bontemps, S., Motte, F., et al. 2014, A&A, 570, A1
Dumas, G., Vaupré, S., Ceccarelli, C., et al. 2014, ApJ, 786, L24
Egan, M. P., Shipman, R. F., Price, S. D., et al. 1998, ApJ, 494, L199
Elia, D., Merello, M., Molinari, S., et al. 2021, MNRAS, 504, 2742
Endres, C. P., Schlemmer, S., Schilke, P., Stutzki, J., & Müller, H. S. 2016, Journal of Molecular Spectroscopy, 327, 95, new Visions of Spectroscopic Databases, Volume II
Felli, M., Palagi, F., & Tofani, G. 1992, A&A, 255, 293
Fuller, G. A., Williams, S. J., & Sridharan, T. K. 2005, A&A, 442, 949
Gómez-Ruiz, A. I., Kurtz, S. E., Araya, E. D., Hofner, P., & Loinard, L. 2016, ApJS, 222, 18
Gregory, P. C. & Condon, J. J. 1991, ApJS, 75, 1011
Griffith, M. R., Wright, A. E., Burke, B. F., & Ekers, R. D. 1994, ApJS, 90, 179
Guillet, V., Pineau Des Forêts, G., & Jones, A. P. 2011, A&A, 527, A123
Gusdorf, A., Pineau Des Forêts, G., Cabrit, S., & Flower, D. R. 2008, A&A, 490, 695
Haschick, A. D. & Baan, W. A. 1993, ApJ, 410, 663
Hennebelle, P., Pérault, M., Teyssier, D., & Ganesh, S. 2001, A&A, 365, 598
Jackson, J. M., Whitaker, J. S., Rathborne, J. M., et al. 2019, ApJ, 870, 5
Jiménez-Serra, I., Caselli, P., Martín-Pintado, J., & Hartquist, T. W. 2008, A&A, 482, 549
Jiménez-Serra, I., Caselli, P., Tan, J. C., et al. 2010, MNRAS, 406, 187
Jiménez-Serra, I., Martín-Pintado, J., Rodríguez-Franco, A., & Martín, S. 2005, ApJ, 627, L121
Kelly, G., Viti, S., García-Burillo, S., et al. 2017, A&A, 597, A11
Kim, C.-H. 2016, PhD thesis, Seoul National University, Korea
Kim, K.-T., Byun, D.-Y., Je, D.-H., et al. 2011, Journal of Korean Astronomical Society, 44, 81
Kim, W.-J., Kim, K.-T., & Kim, K.-T. 2019, ApJS, 244, 2
König, C., Urquhart, J. S., Csengeri, T., et al. 2017, A&A, 599, A139
Kurtz, S., Churchwell, E., & Wood, D. O. S. 1994, ApJS, 91, 659
Kurtz, S., Hofner, P., & Álvarez, C. V. 2004, ApJS, 155, 149
Lee, S.-S., Byun, D.-Y., Oh, C. S., et al. 2011, PASP, 123, 1398
Lefloch, B., Castets, A., Cernicharo, J., & Loinard, L. 1998, ApJ, 504, L109
Liu, R., Liu, T., Chen, G., et al. 2022, MNRAS, 511, 3618
López-Sepulcre, A., Watanabe, Y., Sakai, N., et al. 2016, ApJ, 822, 85
Louvet, F., Motte, F., Gusdorf, A., et al. 2016, A&A, 595, A122
Marsh, K. A., Whitworth, A. P., Lomax, O., et al. 2017, MNRAS, 471, 2730
Martin-Pintado, J., Bachiller, R., & Fuente, A. 1992, A&A, 254, 315
Molinari, S., Brand, J., Cesaroni, R., & Palla, F. 1996, A&A, 308, 573
Motte, F., Bontemps, S., Schilke, P., et al. 2007, A&A, 476, 1243
Müller, H. S. P., Schlöder, F., Stutzki, J., & Winnewisser, G. 2005, Journal of Molecular Structure, 742, 215
Nguyen-Lu'o'ng, Q., Motte, F., Carlhoff, P., et al. 2013, ApJ, 775, 88
Perault, M., Omont, A., Simon, G., et al. 1996, A&A, 315, L165
Peretto, N. & Fuller, G. A. 2009, A&A, 505, 405
Peretto, N., Fuller, G. A., Duarte-Cabral, A., et al. 2013, A&A, 555, A112
Pety, J. 2005, in SF2A-2005: Semaine de l'Astrophysique Francaise, ed. F. Casoli, T. Contini, J. M. Hameury, & L. Pagani, 721
Pillai, T. G. S., Urquhart, J. S., Leurini, S., et al. 2023, MNRAS, 522, 3357
Ramesh, B. & Sridharan, T. K. 1997, MNRAS, 284, 1001
Rathborne, J. M., Jackson, J. M., & Simon, R. 2006, ApJ, 641, 389
Rybarczyk, D. R., Stanimirovic, S., & Gusdorf, A. 2023, arXiv e-prints, arXiv:2304.06741
Sakai, T., Sakai, N., Hirota, T., & Yamamoto, S. 2010, ApJ, 714, 1658
Sánchez-Monge, Á., López-Sepulcre, A., Cesaroni, R., et al. 2013, A&A, 557, A94
Sato, F., Hasegawa, T., Whiteoak, J. B., & Miyawaki, R. 2000, ApJ, 535, 857
Schilke, P., Pineau des Forêts, G., Walmsley, C. M., & Martín-Pintado, J. 2001, A&A, 372, 291
Schilke, P., Walmsley, C. M., Pineau des Forets, G., & Flower, D. R. 1997, A&A, 321, 293
Schuller, F., Menten, K. M., Contreras, Y., Wyrowski, F., & Schilke, e. a. 2009, A&A, 504, 415
Simpson, R. J., Povich, M. S., Kendrew, S., et al. 2012, MNRAS, 424, 2442
Sridharan, T. K., Beuther, H., Schilke, P., Menten, K. M., & Wyrowski, F. 2002, ApJ, 566, 931
Svoboda, B. E., Shirley, Y. L., Battersby, C., et al. 2016, ApJ, 822, 59
Traficante, A., Fuller, G. A., Smith, R. J., et al. 2018, MNRAS, 473, 4975
Turner, B. E. 1998, ApJ, 495, 804
Urquhart, J. S., König, C., Giannetti, A., et al. 2018, MNRAS, 473, 1059
Urquhart, J. S., Wells, M. R. A., Pillai, T., et al. 2022, MNRAS, 510, 3389
Vaupré, S., Hily-Blant, P., Ceccarelli, C., et al. 2014, A&A, 568, A50
Voronkov, M. A., Caswell, J. L., Ellingsen, S. P., Green, J. A., & Breen, S. L. 2014, MNRAS, 439, 2584
Voronkov, M. A., Caswell, J. L., Ellingsen, S. P., & Sobolev, A. M. 2010, MNRAS, 405, 2471
Walmsley, C. M., Pineau des Forêts, G., & Flower, D. R. 1999, A&A, 342, 542
Walsh, A. J., Burton, M. G., Hyland, A. R., & Robinson, G. 1998, MNRAS, 301, 640
Widmann, F., Beuther, H., Schilke, P., & Stanke, T. 2016, A&A, 589, A29
Wood, D. O. S. & Churchwell, E. 1989a, ApJ, 340, 265
Wood, D. O. S. & Churchwell, E. 1989b, ApJS, 69, 831
Wright, A. E., Griffith, M. R., Burke, B. F., & Ekers, R. D. 1994, ApJS, 91, 111
Wyrowski, F., Güsten, R., Menten, K. M., et al. 2016, A&A, 585, A149
Zhu, F.-Y., Wang, J., Yan, Y., Zhu, Q.-F., & Li, J. 2023, MNRAS, 523, 2770
Zhu, F.-Y., Wang, J.-Z., Liu, T., et al. 2020, MNRAS, 499, 6018
Ziurys, L. M., Friberg, P., & Irvine, W. M. 1989, ApJ, 343, 201

Appendix A: Observed sources

Table A.2: Summary of sources

Source name	RA α (J2000)	Dec δ (J2000)	v_{sys} (km s^{-1})	SiO (1 – 0)	H_2O Maser	CH_3OH Maser	Selected Category	ATLASGAL Name	Classification
HM00117+6412	0:14:28	+64:28:46	−37.0	N	Y	N	HMPO	···	unclassified
HM00420+5530	0:44:58	+55:47:18	−51.0	N	Y	N	HMPO	–	unclassified
G5.48−0.24	17:59:03	−24:20:59	75.0	Y[a]	N	N	UCHII	005.474−00.244	MSF (radio-HII)*
G5.89−0.39	18:00:30	−24:04:00	10.0	Y[b]	Y	Y	UCHII	005.884−00.392	MSF (radio-HII)*
G6.55−0.10	18:00:50	−23:20:23	0.0	N	N	N	UCHII	006.551−00.097	MSF (radio-HII)*
G8.14+0.23	18:03:00	−21:48:05	19.7	N	Y	N	UCHII	008.141+00.222	MSF (radio-HII)*
G5.97−1.17	18:03:41	−24:22:44	10.0	N	N	N	UCHII	005.971−01.174	MSF (radio-HII)*
HM18014−2428	18:04:29	−24:28:47	13.0	N	N	N	HMPO	005.974−01.392	unclassified
HM18018−2426	18:04:54	−24:26:41	11.0	N	N	Y	HMPO	006.046−01.443	unclassified
G10.10+0.74	18:05:13	−19:50:35	38.6	N	N	N	UCHII	010.099+00.739	MSF (radio-HII)*
HM18024−2119	18:05:25	−21:19:41	1.0	Y[b]	N	Y	HMPO	008.831−00.027	Protostellar
HM18024−2231	18:05:31	−22:31:36	16.0	N	N	N	HMPO	–	unclassified
HM18162−1612	18:19:08	−16:11:21	62.0	N	N	Y	HMPO	014.891−00.404	MSF (radio-HII)
IRAS18162−2048	18:19:12	−20:47:34	20.0	N	Y	Y	UCHII	–	MSF (radio-HII)*
G15.04−0.68	18:20:25	−16:11:35	21.1	Y[e]	Y	Y	UCHII	–	MSF (radio-HII)*
HM18182−1433	18:21:08	−14:31:53	60.0	N	Y	Y	HMPO	016.586−00.051	MSF (HII)
IRAS18222−1317	18:25:02	−13:15:51	54.9	N	Y	Y	UCHII	018.148−00.284	MSF (radio-HII)*
HM18223−1243	18:25:11	−12:42:17	46.0	N	N	N	HMPO	018.654−00.059	MSF
IRAS18228−1312	18:25:42	−13:10:20	33.3	N	N	N	UCHII	018.301−00.389	MSF (radio-HII)*
G019.27+00.07 MM2	18:25:53	−12:04:48	26.2	Y[e]	Y	N	IRDC	019.286+00.082	Protostellar
G018.82−00.28 MM3	18:25:53	−12:44:37	42.2	Y[e]	N	N	IRDC	018.701−00.229	MSF (HII)
G018.82−00.28 MM1	18:25:56	−12:42:48	42.2	Y[e]	Y	Y	IRDC	018.734−00.226	MSF (HII)
G019.27+00.07 MM1	18:25:59	−12:03:59	26.2	Y[e]	N	N	IRDC	019.309+00.066	Protostellar
IRAS18232−1154	18:26:03	−11:52:34	24.1	N	Y	Y	UCHII	019.488+00.136	MSF (radio-HII)*
G018.82−00.28 MM4	18:26:16	−12:41:32	42.2	Y[b]	N	N	IRDC	018.789−00.286	YSO
G018.82−00.28 MM5	18:26:21	−12:41:11	42.2	N	N	N	IRDC	018.801−00.297	Quiescent
G018.82−00.28 MM2	18:26:23	−12:39:37	42.2	N	N	N	IRDC	018.833−00.301	MSF (radio-HII)
G19.07−0.27	18:26:47	−12:26:32	63.0	N	Y	Y	UCHII	019.076−00.287	MSF (radio-HII)*
HM18247−1147	18:27:31	−11:45:56	122.0	N	N	Y	HMPO	019.754−00.129	MSF (radio-HII)
G19.61−0.23	18:27:38	−11:56:42	41.6	N	Y	Y	UCHII	019.609−00.234	MSF (radio-HII)*
G20.08−0.14	18:28:11	−11:28:45	40.7	N	Y	N	UCHII	020.081−00.136	MSF (radio-HII)*
HM18256−0742	18:28:21	−7:40:22	37.0	N	N	N	HMPO	–	unclassified
HM18264−1152	18:29:14	−11:50:26	44.0	Y[b,c]	Y	Y	HMPO	019.882−00.534	YSO
HM18272−1217	18:30:03	−12:15:27	34.0	N	N	N	HMPO	019.606−00.901	MSF (HII)
G022.35+00.41 MM1	18:30:24	−9:10:34	50.7	Y[a,c]	Y	Y	IRDC	022.376+00.447	Protostellar
G022.35+00.41 MM2	18:30:24	−9:12:44	50.7	N	N	N	IRDC	022.342+00.431	MSF (HII)
HM18278−1009	18:30:35	−10:07:12	94.0	N	N	Y	HMPO	021.561−00.032	YSO
HM18288−0158	18:31:27	−1:56:35	6.0	N	N	N	HMPO	–	unclassified
HM18290−0924	18:31:45	−9:22:09	84.0	N	Y	Y	HMPO	–	unclassified
HM18306−0835	18:33:22	−8:33:38	77.0	N	Y	Y	HMPO	023.264+00.077	MSF (radio-HII)
HM18308−0841	18:33:32	−8:39:17	77.0	N	Y	Y	HMPO	023.199+00.001	MSF (radio-HII)
HM18310−0825	18:33:47	−8:23:35	84.0	N	N	N	HMPO	023.454+00.064	MSF (radio-HII)
G23.71+0.17	18:33:53	−8:07:32	115.0	N	Y	Y	UCHII	023.711+00.171	MSF (radio-HII)*
G023.60+00.00 MM5	18:34:10	−8:18:00	53.5	N	N	N	IRDC	023.582+00.031	MSF
G023.60+00.00 MM3	18:34:10	−8:18:28	53.5	N	N	N	IRDC	–	unclassified
G023.60+00.00 MM1	18:34:12	−8:19:06	106.1	Y[b]	Y	Y	IRDC	023.567+00.014	Protostellar
IRAS18316−0602	18:34:20	−5:59:44	41.4	Y[b,c]	Y	Y	UCHII	025.649+01.051	MSF (radio-HII)*
G023.60+00.00 MM2	18:34:21	−8:18:07	53.5	Y[e]	N	Y	IRDC	023.601−00.012	YSO
G023.60+00.00 MM7	18:34:21	−8:17:11	53.5	Y[e]	N	N	IRDC	–	unclassified
G023.60+00.00 MM4	18:34:23	−8:18:21	53.5	Y[b]	N	N	IRDC	–	unclassified
G23.96+0.15	18:34:25	−7:54:48	79.6	N	Y	Y	UCHII	023.954+00.151	MSF (radio-HII)*
G23.46−0.20	18:34:45	−8:31:07	65.0	N	N	N	UCHII	023.454−00.201	MSF (radio-HII)*
G024.08+00.04 MM1	18:34:57	−7:43:26	52.5	N	N	N	IRDC	024.183+00.121	MSF (radio-HII)
G024.33+00.11 MM1	18:35:08	−7:35:04	113.6	Y[b]	Y	Y	IRDC	024.328+00.144	YSO
G024.33+00.11 MM6	18:35:08	−7:34:33	113.6	Y[e]	Y	Y	IRDC	–	unclassified
G024.33+00.11 MM8	18:35:23	−7:37:21	113.6	N	N	N	IRDC	024.324+00.069	Extended 70 Micron
G024.33+00.11 MM9	18:35:27	−7:36:56	113.6	N	N	Y	IRDC	024.328+00.062	Quiescent
G024.33+00.11 MM3	18:35:28	−7:36:18	113.6	Y[e]	N	Y	IRDC	024.346+00.062	PDR−Quiescent
G024.33+00.11 MM10	18:35:28	−7:35:32	113.6	Y[e]	N	N	IRDC	–	unclassified
G024.33+00.11 MM5	18:35:34	−7:36:42	113.6	Y[a]	Y	Y	IRDC	024.351+00.037	Quiescent
G024.33+00.11 MM2	18:35:35	−7:37:28	113.6	Y[e]	Y	Y	IRDC	024.343+00.029	Quiescent
G024.60+00.08 MM2	18:35:36	−7:18:09	51.7	N	Y	N	IRDC	024.629+00.172	Protostellar
G024.60+00.08 MM1	18:35:40	−7:18:37	51.7	Y[a]	Y	Y	IRDC	024.633+00.152	YSO
G024.60+00.08 MM3	18:35:41	−7:18:30	51.7	Y	Y	Y	IRDC	024.633+00.152	YSO
HM18337−0743	18:36:29	−7:40:33	58.0	N	N	Y	HMPO	024.401−00.189	MSF (HII)
HM18345−0641	18:37:17	−6:38:32	96.0	Y[b]	N	Y	HMPO	025.409+00.106	MSF (radio-HII)
HM18348−0616	18:37:29	−6:14:15	110.0	N	Y	N	HMPO	025.796+00.242	MSF (radio-HII)
G25.72+0.05	18:38:03	−6:23:47	54.5	N	Y	N	UCHII	025.709+00.044	MSF (radio-HII)*

Table A.2: continued

Source name	RA α (J2000)	Dec δ (J2000)	v_{sys} (km s^{-1})	SiO (1 – 0)	H_2O Maser	CH_3OH Maser	Selected Category	ATLASGAL Name	Classification
G025.04−00.20 MM1	18:38:10	−7:02:34	63.5	Y[e]	N	Y	IRDC	025.153−00.274	YSO
G025.04−00.20 MM4	18:38:14	−7:03:12	63.5	N	N	N	IRDC	–	unclassified
G025.04−00.20 MM2	18:38:18	−7:02:51	63.5	Y[e]	N	Y	IRDC	025.163−00.304	Protostellar
HM18363−0554	18:39:04	−5:52:15	65.0	N	N	N	HMPO	026.294+00.071	Extended Emission
HM18372−0541	18:39:56	−5:38:49	23.0	N	Y	N	HMPO	026.596−00.022	MSF (radio-HII)
G27.28+0.15	18:40:34	−4:57:48	31.7	N	Y	Y	UCHII	027.273+00.147	MSF (radio-HII)*
G27.28+0.15	18:40:34	−4:57:48	31.7	N	Y	Y	UCHII	027.279+00.147	MSF (radio-HII)*
HM18385−0512	18:41:12	−5:09:06	26.0	N	Y	N	HMPO	027.184−00.081	MSF (radio-HII)
G027.75+00.16 MM3	18:41:17	−4:31:55	79.1	N	N	N	IRDC	–	unclassified
G027.75+00.16 MM1	18:41:20	−4:32:20	79.1	N	N	N	IRDC	027.741+00.172	Protostellar
G027.75+00.16 MM2	18:41:33	−4:33:44	79.1	N	N	N	IRDC	027.746+00.116	unclassified
HM18396−0431	18:42:19	−4:28:37	97.0	N	N	N	HMPO	027.903−00.012	MSF (radio-HII)
G028.08+00.07 MM1	18:42:20	−4:16:42	75.8	N	N	N	IRDC	028.089+00.071	Quiescent
G028.37+00.07 MM5	18:42:27	−4:01:30	78.6	N	Y	N	IRDC	028.324+00.161	YSO
G028.37+00.07 MM15	18:42:32	−4:01:16	78.6	N	Y	N	IRDC	028.341+00.142	MSF
G028.37+00.07 MM2	18:42:38	−4:02:05	78.6	Y[e]	Y	Y	IRDC	028.336+00.117	YSO
G028.37+00.07 MM16	18:42:40	−4:00:23	78.6	Y[e]	Y	N	IRDC	028.364+00.121	Quiescent
G028.37+00.07 MM13	18:42:42	−3:57:08	78.6	N	Y	N	IRDC	028.418+00.141	MSF (HII)
G028.37+00.07 MM11	18:42:43	−4:01:44	78.6	Y[e]	Y	N	IRDC	028.354+00.102	Protostellar
G028.37+00.07 MM6	18:42:49	−4:02:23	78.6	Y[c]	Y	Y	IRDC	028.354+00.072	Quiescent
G028.37+00.07 MM8	18:42:50	−4:09:54	78.6	N	N	N	IRDC	028.244+00.012	MSF (radio-HII)
G028.37+00.07 MM4	18:42:51	−4:03:15	78.6	Y[b,c]	Y	Y	IRDC	028.344+00.061	Protostellar
G028.37+00.07 MM1	18:42:52	−3:59:45	78.6	Y[e]	Y	Y	IRDC	028.398+00.081	unclassified
G028.37+00.07 MM10	18:42:54	−4:02:30	78.6	Y[d]	Y	Y	IRDC	028.361+00.054	YSO
G028.37+00.07 MM7	18:42:56	−4:07:31	78.6	N	N	N	IRDC	028.291+00.007	unclassified
G028.67+00.13 MM3	18:42:58	−3:48:20	79.5	N	N	N	IRDC	028.581+00.146	MSF (radio-HII)
IRAS18403−0417	18:42:58	−4:14:00	97.4	N	Y	Y	UCHII	028.199−00.049	MSF (radio-HII)*
G028.37+00.07 MM17	18:43:00	−4:01:34	78.6	N	Y	Y	IRDC	028.388+00.037	Quiescent
G028.37+00.07 MM3	18:43:03	−4:06:24	99.7	N	N	Y	IRDC	028.321−00.009	MSF
G028.67+00.13 MM1	18:43:03	−3:41:41	79.5	N	N	N	IRDC	028.687+00.177	MSF (HII)
G028.67+00.13 MM2	18:43:07	−3:44:01	79.5	N	N	Y	IRDC	028.658+00.144	Quiescent
G028.67+00.13 MM6	18:43:12	−3:45:39	79.5	N	N	N	IRDC	028.642+00.119	Extended 70 Micron
G028.37+00.07 MM18	18:43:13	−4:01:16	78.6	N	N	N	IRDC	028.416−00.007	YSO
G028.23−00.19 MM2	18:43:29	−4:12:16	79.6	N	N	N	IRDC	–	unclassified
G028.23−00.19 MM3	18:43:30	−4:12:33	79.6	N	N	N	IRDC	–	unclassified
G027.97−00.42 MM1	18:43:53	−4:36:13	45.9	N	N	N	IRDC	027.974−00.421	Protostellar
G027.97−00.42 MM3	18:43:55	−4:36:08	45.9	N	N	Y	IRDC	–	unclassified
G027.97−00.42 MM2	18:43:58	−4:34:24	45.9	N	Y	N	IRDC	028.011−00.426	YSO
G027.94−00.47 MM2	18:44:03	−4:37:25	45.7	N	Y	Y	IRDC	–	unclassified
G027.94−00.47 MM1	18:44:04	−4:38:00	45.7	N	Y	Y	IRDC	027.968−00.474	YSO
G028.04−00.46 MM1	18:44:09	−4:33:22	45.5	Y[e]	N	Y	IRDC	028.048−00.456	YSO
G028.28−00.34 MM4	18:44:11	−4:17:22	47.4	N	Y	N	IRDC	–	unclassified
G028.28−00.34 MM3	18:44:13	−4:18:05	47.4	N	Y	Y	IRDC	028.288−00.362	MSF (radio-HII)
G028.28−00.34 MM1	18:44:15	−4:17:54	47.4	N	N	Y	IRDC	028.288−00.362	MSF (radio-HII)
G028.53−00.25 MM2	18:44:16	−3:59:41	87.0	Y[a,c]	N	Y	IRDC	–	unclassified
G028.53−00.25 MM5	18:44:17	−4:02:04	87.0	N	N	N	IRDC	028.526−00.251	Protostellar
G028.53−00.25 MM6	18:44:18	−4:00:05	87.0	Y[b,c]	Y	Y	IRDC	028.564−00.236	Protostellar
G028.53−00.25 MM10	18:44:19	−3:58:43	87.0	Y[b]	Y	N	IRDC	–	unclassified
G028.53−00.25 MM4	18:44:19	−4:00:05	87.0	N	N	N	IRDC	028.564−00.236	Protostellar
G028.53−00.25 MM9	18:44:19	−3:58:05	87.0	N	Y	N	IRDC	–	unclassified
IRAS18416−0420	18:44:19	−4:17:53	48.1	N	Y	Y	UCHII	028.301−00.382	MSF (radio-HII)*
G028.28−00.34 MM2	18:44:21	−4:17:37	47.4	N	N	N	IRDC	028.301−00.382	MSF (radio-HII)
HM18424−0329	18:45:03	−3:26:49	48.0	N	N	N	HMPO	–	unclassified
HM18426−0204	18:45:13	−2:01:12	15.0	N	Y	Y	HMPO	030.423+00.466	MSF (radio-HII)
HM18431−0312	18:45:47	−3:09:24	105.0	N	N	N	HMPO	029.476−00.179	MSF (HII)
G29.96−0.02	18:46:04	−2:39:22	96.0	Y[b,c]	Y	Y	UCHII	029.954−00.016	MSF (radio-HII)*
HM18437−0216	18:46:23	−2:13:24	111.0	N	N	N	HMPO	–	unclassified
HM18440−0148	18:46:36	−1:45:23	98.0	N	N	N	HMPO	030.818+00.274	YSO
G030.14−00.06 MM1	18:46:36	−2:31:03	86.7	N	N	N	IRDC	030.138−00.071	Quiescent
G30.54+0.02	18:46:59	−2:07:32	−48.0	N	Y	Y	UCHII	030.534+00.021	MSF (radio-HII)*
HM18445−0222	18:47:11	−2:19:06	87.0	N	N	N	HMPO	030.386−00.104	unclassified
HM18447−0229	18:47:24	−2:25:55	103.0	N	N	N	HMPO	–	unclassified
G31.41+0.31	18:47:35	−1:12:43	98.5	Y[c]	Y	Y	UCHII	031.412+00.307	MSF (radio-HII)*
G030.57−00.23 MM3	18:47:55	−2:11:15	86.2	N	N	N	IRDC	030.583−00.211	Quiescent
G030.57−00.23 MM2	18:47:59	−2:15:20	86.2	N	N	N	IRDC	030.529−00.259	YSO
G030.57−00.23 MM6	18:47:59	−2:13:13	86.2	N	N	N	IRDC	–	unclassified
G030.57−00.23 MM1	18:48:00	−2:07:20	86.2	Y[b]	N	N	IRDC	030.651−00.204	YSO
HM18454−0158	18:48:01	−1:54:49	53.0	N	Y	N	HMPO	–	unclassified
HM18454−0136	18:48:04	−1:33:23	39.0	N	N	N	HMPO	031.158+00.047	MSF (radio-HII)
IRAS18456−0129	18:48:15	−1:26:25	109.9	N	Y	Y	UCHII	–	MSF (radio-HII)*
G030.97−00.14 MM1	18:48:22	−1:48:27	78.8	Y[e]	N	Y	IRDC	030.971−00.141	YSO
G030.97−00.14 MM2	18:48:22	−1:47:42	78.8	N	N	N	IRDC	–	unclassified
HM18460−0307	18:48:39	−3:03:53	84.0	N	N	N	HMPO	029.886−00.781	MSF (HII)

Table A.2: continued

Source name	RA α (J2000)	Dec δ (J2000)	v_{sys} (km s^{-1})	SiO (1 – 0)	H_2O Maser	CH_3OH Maser	Selected Category	ATLASGAL Name	Classification
G031.97+00.07 MM5	18:49:22	−0:50:35	96.7	Y[b]	N	Y	IRDC	031.946+00.076	Protostellar
G031.97+00.07 MM7	18:49:28	−0:48:54	96.7	N	N	N	IRDC	031.982+00.064	Quiescent
G031.97+00.07 MM8	18:49:29	−0:48:12	96.7	Y[e]	N	N	IRDC	–	unclassified
G031.97+00.07 MM3	18:49:32	−0:47:02	96.7	Y[b,c]	Y	N	IRDC	032.019+00.064	MSF (HII)
G031.97+00.07 MM4	18:49:33	−0:47:33	96.7	Y[a,c]	Y	Y	IRDC	032.007+00.062	unclassified
IRAS18469−0132	18:49:35	−1:29:08	87.7	N	Y	Y	UCHII	031.396−00.257	MSF (radio-HII)*
G031.97+00.07 MM2	18:49:36	−0:46:16	96.7	Y[a,c]	N	N	IRDC	032.044+00.059	YSO
G031.97+00.07 MM1	18:49:36	−0:45:45	96.7	Y[a,c]	Y	Y	IRDC	032.044+00.059	YSO
HM18470−0044	18:49:37	−0:41:05	97.0	N	Y	N	HMPO	032.117+00.091	MSF (HII)
HM18472−0022	18:49:51	−0:19:09	49.0	N	N	N	HMPO	032.471+00.204	MSF (radio-HII)
IRAS18479−0005	18:50:31	−0:01:59	15.0	Y[b]	Y	N	UCHII	032.797+00.191	MSF (radio-HII)*
HM18488+0000	18:51:25	+00:04:19	83.0	N	Y	Y	HMPO	032.990+00.034	MSF (radio-HII)
G33.50+0.20	18:51:47	+00:35:32	11.0	N	N	N	UCHII	–	MSF (radio-HII)*
IRAS18496+0004	18:52:10	+00:08:40	76.9	N	Y	Y	UCHII	–	MSF (radio-HII)*
G033.69−00.01 MM5	18:52:48	+00:36:47	105.9	Y[b]	Y	N	IRDC	033.633−00.022	YSO
G33.92+0.11	18:52:50	+00:55:29	107.6	Y[c]	Y	Y	UCHII	033.914+00.109	MSF (radio-HII)*
G033.69−00.01 MM2	18:52:50	+00:37:57	105.9	Y[e]	N	N	IRDC	033.656−00.019	MSF (HII)
G033.69−00.01 MM3	18:52:51	+00:36:43	105.9	Y[b]	N	N	IRDC	033.638−00.034	YSO
G033.69−00.01 MM10	18:52:53	+00:38:35	105.9	N	N	Y	IRDC	–	unclassified
G033.69−00.01 MM4	18:52:56	+00:43:08	105.9	Y[c]	N	Y	IRDC	033.744−00.007	Protostellar
G033.69−00.01 MM9	18:52:58	+00:41:20	105.9	N	N	N	IRDC	–	unclassified
G033.69−00.01 MM1	18:52:59	+00:42:37	105.9	Y[e]	Y	Y	IRDC	033.739−00.021	YSO
G034.43+00.24 MM8	18:53:16	+01:26:20	57.1	Y[b]	Y	Y	IRDC	–	unclassified
HM18507+0121	18:53:17	+01:24:55	57.0	Y[a,c]	Y	Y	HMPO	034.401+00.226	MSF (radio-HII)
G034.43+00.24 MM7	18:53:18	+01:27:13	57.1	Y[b]	Y	Y	IRDC	–	unclassified
G034.43+00.24 MM1	18:53:18	+01:25:24	57.1	Y[a,c]	Y	Y	IRDC	034.411+00.234	YSO
G34.26+0.15	18:53:19	+01:14:58	58.3	Y[b,c]	Y	Y	UCHII	034.258+00.154	MSF (radio-HII)*
G034.43+00.24 MM2	18:53:19	+01:24:40	57.1	Y[a,c]	Y	Y	IRDC	034.401+00.226	MSF (radio-HII)
G034.43+00.24 MM6	18:53:19	+01:27:48	57.1	Y[b]	Y	Y	IRDC	–	unclassified
G034.43+00.24 MM4	18:53:19	+01:24:08	57.1	Y[b,c]	N	Y	IRDC	034.401+00.226	MSF (radio-HII)
G034.43+00.24 MM5	18:53:20	+01:23:30	57.1	Y[b]	Y	Y	IRDC	034.391+00.214	unclassified
G034.43+00.24 MM3	18:53:20	+01:28:23	57.1	Y[b,c]	Y	Y	IRDC	034.459+00.247	YSO
HM18511+0146	18:53:38	+01:50:27	57.0	N	N	N	HMPO	034.821+00.351	YSO
IRAS18515+0157	18:54:04	+02:01:34	51.9	N	Y	Y	UCHII	–	MSF (radio-HII)*
HM18517+0437	18:54:14	+04:41:32	44.0	Y[e]	Y	Y	HMPO	037.431+01.519	unclassified
HM18521+0134	18:54:41	+01:38:02	76.0	N	N	N	HMPO	034.757+00.024	MSF (HII)
HM18527+0301	18:55:17	+03:05:07	76.0	N	Y	N	HMPO	036.114+00.554	MSF (HII)
HM18530+0215	18:55:34	+02:19:08	78.0	Y[b,c]	N	N	HMPO	035.466+00.141	MSF (radio-HII)
HM18532+0047	18:55:51	+00:51:22	59.0	N	Y	N	HMPO	034.196−00.592	MSF (radio-HII)
IRAS18534+0218	18:56:01	+02:22:52	49.6	N	Y	N	UCHII	035.577+00.067	MSF (radio-HII)*
IRAS18538+0216	18:56:24	+02:20:38	53.2	N	Y	N	UCHII	035.579−00.031	MSF (radio-HII)*
HM18540+0220	18:56:36	+02:24:54	50.0	N	N	N	HMPO	035.671−00.046	MSF
G035.39−00.33 MM1	18:56:41	+02:09:52	44.7	N	Y	N	IRDC	035.457−00.179	MSF (radio-HII)
G034.77−00.55 MM3	18:56:45	+01:20:42	43.5	N	N	N	IRDC	–	unclassified
G034.77−00.55 MM1	18:56:48	+01:18:47	43.5	Y[c]	N	N	IRDC	034.712−00.596	YSO
G035.39−00.33 MM2	18:56:59	+02:04:53	44.7	N	Y	N	IRDC	035.419−00.284	MSF
G035.59−00.24 MM1	18:57:02	+02:17:04	44.7	N	N	N	IRDC	035.604−00.202	MSF (HII)
G035.39−00.33 MM3	18:57:05	+02:06:29	44.7	N	Y	Y	IRDC	035.452−00.296	MSF (HII)
G035.59−00.24 MM2	18:57:07	+02:16:14	44.7	N	N	N	IRDC	035.601−00.229	Protostellar
G035.39−00.33 MM4	18:57:07	+02:08:23	44.7	N	Y	N	IRDC	035.484−00.287	Protostellar
G035.39−00.33 MM7	18:57:08	+02:10:50	44.7	N	N	N	IRDC	035.522−00.274	YSO
G035.39−00.33 MM6	18:57:08	+02:09:09	44.7	N	N	N	IRDC	035.496−00.287	Protostellar
G35.05−0.52	18:57:09	+01:39:03	49.6	N	Y	Y	UCHII	035.054−00.517	MSF (radio-HII)*
G035.59−00.24 MM3	18:57:12	+02:16:08	44.7	N	N	N	IRDC	035.607−00.244	Quiescent
HM18551+0302	18:57:42	+03:06:05	58.0	N	N	N	HMPO	036.406+00.021	MSF (radio-HII)
HM18553+0414	18:57:53	+04:18:06	10.0	N	Y	N	HMPO	037.498+00.531	YSO
HM18565+0349	18:59:03	+03:53:22	92.0	N	Y	Y	HMPO	037.268+00.081	MSF (HII)
HM18566+0408	18:59:10	+04:12:14	85.0	Y[b,c]	Y	Y	HMPO	037.554+00.201	YSO
HM18567+0700	18:59:14	+07:04:47	29.0	N	N	N	HMPO	040.121+01.500	MSF (HII)
HM18571+0349	18:59:40	+03:53:35	56.0	N	N	N	HMPO	–	unclassified
G37.55−0.11	19:00:16	+04:03:13	53.7	N	Y	N	UCHII	037.546−00.112	MSF (radio-HII)*
HM18586+0106	19:01:11	+01:11:16	38.0	N	N	N	HMPO	–	unclassified
IRAS18592+0108	19:01:47	+01:13:08	43.6	N	Y	Y	UCHII	–	MSF (radio-HII)*
IRAS18593+0408	19:01:53	+04:12:50	60.7	N	Y	N	UCHII	037.874−00.399	MSF (radio-HII)*
HM19012+0505	19:03:44	+05:09:49	40.0	N	Y	N	HMPO	–	unclassified
HM19012+0536	19:03:45	+05:40:40	66.0	N	N	Y	HMPO	039.388−00.141	MSF (radio-HII)
G038.95−00.47 MM4	19:04:01	+05:09:06	41.6	N	N	N	IRDC	–	unclassified
G038.95−00.47 MM2	19:04:03	+05:07:56	41.6	N	N	N	IRDC	038.937−00.457	YSO
G038.95−00.47 MM1	19:04:07	+05:08:48	41.6	Y[e]	N	N	IRDC	038.957−00.466	YSO
HM19035+0641	19:06:01	+06:46:35	32.0	N	Y	N	HMPO	040.622−00.137	MSF (radio-HII)
HM19043+0726	19:06:48	+07:31:38	59.0	N	N	Y	HMPO	041.377+00.037	MSF (radio-HII)
G41.71+0.11	19:07:10	+07:51:36	−10.0	N	N	N	UCHII	–	MSF (radio-HII)*
G41.74+0.10	19:07:16	+07:52:44	−13.0	N	N	N	UCHII	041.741+00.097	MSF (radio-HII)*

Table A.2: continued

Source name	RA α (J2000)	Dec δ (J2000)	v_{sys} (km s^{-1})	SiO (1 – 0)	H_2O Maser	CH_3OH Maser	Selected Category	ATLASGAL Name	Classification
G42.90+0.57	19:07:42	+09:07:20	−20.6	N	N	N	UCHII	–	MSF (radio-HII)*
G42.42−0.27	19:09:50	+08:18:44	25.0	N	Y	Y	UCHII	042.421−00.259	MSF (radio-HII)*
HM19074+0752	19:09:53	+07:57:22	55.0	N	N	N	HMPO	042.108−00.447	MSF
IRAS19081+0903	19:10:35	+09:08:31	6.7	N	Y	Y	UCHII	043.236−00.047	MSF (radio-HII)*
HM19088+0902	19:11:16	+09:07:27	60.0	N	Y	Y	HMPO	043.306−00.212	MSF (radio-HII)
HM19092+0841	19:11:37	+08:46:30	60.0	N	Y	Y	HMPO	043.038−00.452	MSF (radio-HII)
HM19094+0944	19:11:52	+09:49:46	65.0	N	N	N	HMPO	043.994−00.012	YSO
IRAS19095+0930	19:11:53	+09:35:46	44.1	N	Y	Y	UCHII	043.794−00.127	MSF (radio-HII)*
G44.26+0.10	19:11:57	+10:07:02	60.0	N	N	N	UCHII	–	MSF (radio-HII)*
G43.18−0.52	19:12:09	+08:52:09	57.2	N	Y	Y	UCHII	043.179−00.519	MSF (radio-HII)*
G45.07+0.13	19:13:22	+10:50:53	58.3	N	Y	Y	UCHII	045.071+00.132	MSF (radio-HII)*
G45.12+0.13	19:13:28	+10:53:37	58.6	N	Y	N	UCHII	045.121+00.131	MSF (radio-HII)*
G45.48+0.13	19:14:09	+11:12:16	60.8	N	Y	N	UCHII	045.474+00.134	MSF (radio-HII)*
G45.45+0.06	19:14:21	+11:09:14	57.6	N	Y	N	UCHII	045.454+00.061	MSF (radio-HII)*
G43.89−0.78	19:14:26	+09:22:34	52.9	N	Y	Y	UCHII	043.889−00.786	MSF (radio-HII)*
G45.47+0.05	19:14:26	+11:09:26	57.6	Y[c]	Y	N	UCHII	045.466+00.046	MSF (radio-HII)*
HM19175+1357	19:19:49	+14:02:46	15.0	N	N	N	HMPO	048.634+00.231	MSF (HII)
IRAS19181+1349	19:20:28	+13:55:26	17.7	N	Y	Y	UCHII	–	MSF (radio-HII)*
G50.31+0.68	19:21:28	+15:44:21	26.0	N	Y	N	UCHII	050.314+00.676	MSF (radio-HII)*
G048.65−00.29 MM2	19:21:48	+13:49:22	34.0	N	Y	N	IRDC	–	unclassified
G048.65−00.29 MM1	19:21:50	+13:49:30	34.0	Y[e]	Y	N	IRDC	048.669−00.304	YSO
HM19198+1423	19:22:08	+14:29:20	60.0	N	Y	N	HMPO	049.288−00.056	MSF (HII)
G50.23+0.33	19:22:35	+15:30:10	30.0	N	N	N	UCHII	–	MSF (radio-HII)*
HM19213+1723	19:23:37	+17:28:59	42.0	N	Y	N	HMPO	052.099+01.042	MSF (radio-HII)
W51D	19:23:40	+14:30:51	59.6	Y[b]	Y	Y	UCHII	049.489−00.369	MSF (radio-HII)*
HM19217+1651	19:23:59	+16:57:37	4.0	Y[b,c]	Y	Y	HMPO	051.678+00.719	MSF (radio-HII)
HM19220+1432	19:24:20	+14:38:03	69.0	N	Y	N	HMPO	049.669−00.457	MSF (radio-HII))
HM19266+1745	19:28:54	+17:51:56	5.0	N	N	Y	HMPO	053.037+00.112	MSF (radio-HII)
G053.11+00.05 MM3	19:29:01	+17:55:11	22.0	N	N	N	IRDC	053.092+00.119	MSF (HII)
G053.11+00.05 MM1	19:29:17	+17:56:21	22.0	Y[b]	Y	Y	IRDC	053.141+00.069	YSO
G053.11+00.05 MM2	19:29:20	+17:57:06	22.0	Y[e]	Y	N	IRDC	053.161+00.066	YSO
G053.11+00.05 MM4	19:29:20	+17:55:04	22.0	N	N	N	IRDC	–	unclassified
G053.11+00.05 MM5	19:29:26	+17:54:53	22.0	N	N	N	IRDC	053.136+00.027	YSO
G053.25+00.04 MM6	19:29:32	+17:59:50	23.9	N	Y	N	IRDC	053.219+00.049	YSO
G053.25+00.04 MM2	19:29:33	+18:01:00	23.9	N	Y	N	IRDC	053.239+00.052	YSO
G053.25+00.04 MM4	19:29:35	+18:01:39	23.9	N	Y	N	IRDC	–	unclassified
G053.25+00.04 MM5	19:29:39	+17:58:40	23.9	N	N	N	IRDC	–	unclassified
G053.25+00.04 MM1	19:29:39	+18:01:42	23.9	N	Y	Y	IRDC	053.259+00.039	Protostellar
G053.31+00.00 MM2	19:29:42	+18:03:57	24.0	N	N	N	IRDC	053.301+00.044	Protostellar
G053.25+00.04 MM3	19:29:44	+17:58:47	23.9	N	N	N	IRDC	–	unclassified
G053.31+00.00 MM3	19:29:50	+18:04:39	24.0	N	N	N	IRDC	–	unclassified
G053.31+00.00 MM1	19:29:50	+18:05:07	24.0	N	N	N	IRDC	–	unclassified
IRAS19282+1814	19:30:28	+18:20:53	23.6	N	N	N	UCHII	053.632+00.014	MSF (radio-HII)*
G54.10−0.06	19:31:42	+18:42:52	39.9	N	Y	N	UCHII	–	MSF (radio-HII)*
HM19368+2239	19:38:58	+22:46:32	36.0	Y[c]	N	Y	HMPO	058.469+00.436	MSF (HII)
HM19374+2352	19:39:33	+23:59:55	37.0	N	Y	Y	HMPO	059.602+00.912	MSF (radio-HII)
HM19388+2357	19:40:59	+24:04:39	35.0	N	Y	Y	HMPO	059.832+00.672	YSO
HM19403+2258	19:42:27	+23:05:12	27.0	N	N	N	HMPO	059.136−00.117	MSF (radio-HII)
IRAS19410+2336	19:43:12	+23:44:06	22.4	Y[e]	Y	Y	UCHII	059.782+00.066	MSF (radio-HII)*
HM19411+2306	19:43:18	+23:13:59	29.0	N	Y	N	HMPO	059.359−00.207	YSO
HM19413+2332	19:43:29	+23:40:04	21.0	N	N	N	HMPO	059.762−00.026	MSF (HII)
IRAS19442+2427	19:46:20	+24:35:24	21.7	N	Y	N	UCHII	–	MSF (radio-HII)*
G61.48+0.09	19:46:47	+25:12:44	21.9	N	Y	N	UCHII	–	MSF (radio-HII)*
HM19471+2641	19:49:10	+26:48:52	21.0	N	Y	N	HMPO	–	unclassified
IRAS19598+3324	20:01:46	+33:32:44	−25.2	N	Y	Y	UCHII	–	MSF (radio-HII)*
HM20051+3435	20:07:04	+34:44:35	12.0	N	N	N	HMPO	–	unclassified
HM20050+2720	20:07:07	+27:28:53	6.0	N	Y	Y	HMPO	–	unclassified
HM20056+3350	20:07:32	+33:59:39	9.0	N	Y	N	HMPO	–	unclassified
HM20062+3550	20:08:10	+35:59:20	1.0	N	Y	Y	HMPO	–	unclassified
IRAS20081+3122	20:10:09	+31:31:34	11.6	Y[e]	Y	Y	UCHII	–	MSF (radio-HII)*
HM20081+2720	20:10:12	+27:29:06	6.0	N	N	N	HMPO	–	unclassified
HM20099+3640	20:11:46	+36:49:37	−36.0	N	Y	N	HMPO	–	unclassified
HM20106+3545	20:12:31	+35:54:46	8.0	N	N	N	HMPO	–	unclassified
HM20126+4104	20:14:26	+41:13:32	−4.0	Y[e]	Y	Y	HMPO	–	unclassified
IRAS20178+4046	20:19:39	+40:56:30	0.9	N	N	N	UCHII	–	MSF (radio-HII)*
HM20188+3928	20:20:39	+39:37:52	2.0	Y[e]	Y	Y	HMPO	–	unclassified
G75.83+0.40	20:21:39	+37:31:04	0.0	N	N	Y	UCHII	–	MSF (radio-HII)*
G75.78+0.34	20:21:44	+37:26:40	−0.1	Y[b]	Y	Y	UCHII	–	MSF (radio-HII)*
HM20205+3948	20:22:22	+39:58:05	−2.0	N	N	N	HMPO	–	unclassified
HM20216+4107	20:23:24	+41:17:40	−2.0	N	N	N	HMPO	–	unclassified
HM20217+3947	20:23:32	+39:57:23	−1.0	N	N	N	HMPO	–	unclassified
IRAS20220+3728	20:23:56	+37:38:10	−2.7	N	N	Y	UCHII	–	MSF (radio-HII)*
IRAS20255+3712	20:27:27	+37:22:48	−1.7	N	Y	N	UCHII	–	MSF (radio-HII)*

Table A.2: continued

Source name	RA α (J2000)	Dec δ (J2000)	v_{sys} (km s^{-1})	SiO (1 – 0)	H_2O Maser	CH_3OH Maser	Selected Category	ATLASGAL Name	Classification
IRAS20264+4042	20:28:12	+40:52:28	0.0	N	N	Y	UCHII	–	MSF (radio-HII)*
IRAS20277+3851	20:29:36	+39:01:17	−2.9	N	Y	N	UCHII	–	MSF (radio-HII)*
HM20278+3521	20:29:47	+35:31:39	−5.0	N	N	N	HMPO	–	unclassified
HM20286+4105	20:30:28	+41:15:48	−4.0	N	Y	Y	HMPO	–	unclassified
HM20293+3952	20:31:11	+40:03:10	6.0	Y[b]	Y	Y	HMPO	–	unclassified
IRAS20306+4005	20:32:29	+40:16:05	3.7	N	N	N	UCHII	–	MSF (radio-HII)*
HM20319+3958	20:33:49	+40:08:45	9.0	N	N	N	HMPO	–	unclassified
HM20332+4124	20:35:01	+41:34:48	−2.0	N	Y	N	HMPO	–	unclassified
HM20333+4102	20:35:10	+41:13:18	8.0	N	N	N	HMPO	–	unclassified
HM20343+4129	20:36:07	+41:40:01	11.5	N	N	N	HMPO	–	unclassified
IRAS20350+4126	20:36:53	+41:36:32	−3.1	N	N	N	UCHII	–	MSF (radio-HII)*
DR21	20:39:01	+42:19:43	0.0	Y[a]	Y	Y	UCHII	–	MSF (radio-HII)*
HM20444+4629	20:46:08	+46:40:41	−4.0	N	N	N	HMPO	–	unclassified
HM21078+5211	21:09:25	+52:23:44	−6.0	N	Y	N	HMPO	–	unclassified
HM21307+5049	21:32:32	+51:02:22	−47.0	N	Y	Y	HMPO	–	unclassified
HM21391+5802	21:40:42	+58:16:10	0.0	N	Y	Y	HMPO	–	unclassified
HM21519+5613	21:53:39	+56:27:46	−63.0	N	N	N	HMPO	–	unclassified
HM22134+5834	22:15:09	+58:49:09	−20.0	N	Y	N	HMPO	–	unclassified
HM22172+5549	22:19:09	+56:04:45	−44.0	N	N	N	HMPO	–	unclassified
IRAS22176+6303	22:19:18	+63:18:46	−10.0	Y[e]	Y	Y	UCHII	–	MSF (radio-HII)*
HM22198+6336	22:21:28	+63:51:42	−11.0	N	Y	N	HMPO	–	unclassified
HM22305+5803	22:32:24	+58:18:58	−52.0	N	N	N	HMPO	–	unclassified
HM22506+5944	22:52:39	+60:00:56	−52.0	Y[b]	Y	Y	HMPO	–	unclassified
IRAS22543+6145	22:56:19	+62:01:57	−11.1	N	Y	Y	UCHII	–	MSF (radio-HII)*
IRAS22551+6221	22:57:05	+62:37:44	−13.4	N	N	N	UCHII	–	MSF (radio-HII)*
HM22570+5912	22:59:06	+59:28:28	−47.0	N	Y	N	HMPO	–	unclassified
HM23026+5948	23:04:46	+60:04:35	−51.0	N	N	N	HMPO	–	unclassified
HM23033+5951	23:05:26	+60:08:08	−53.0	Y[e]	Y	Y	HMPO	–	unclassified
NGC 7538	23:13:46	+61:28:21	−57.2	Y[e]	Y	Y	UCHII	–	MSF (radio-HII)*
IRAS23133+6050	23:15:32	+61:07:09	−56.3	N	Y	Y	UCHII	–	MSF (radio-HII)*
IRAS23138+5945	23:16:05	+60:02:00	−44.1	N	Y	N	UCHII	–	MSF (radio-HII)*
HM23139+5939	23:16:09	+59:55:23	−45.0	N	Y	Y	HMPO	–	unclassified
HM23140+6121	23:16:12	+61:37:45	−52.0	N	N	N	HMPO	–	unclassified
HM23151+5912	23:17:21	+59:28:49	−54.0	N	Y	Y	HMPO	–	unclassified
HM23314+6033	23:33:44	+60:50:30	−45.0	N	Y	N	HMPO	–	unclassified
HM23385+6053	23:40:53	+61:10:21	−50.0	N	Y	Y	HMPO	–	unclassified
HM23545+6508	23:57:05	+65:25:11	−20.0	N	N	N	HMPO	–	unclassified
IRAS02232+6138	2:27:01	+61:52:14	−46.4	Y[e]	Y	Y	UCHII	–	MSF (radio-HII)*
IRAS02575+6017	3:01:32	+60:29:12	−38.0	N	N	Y	UCHII	–	MSF (radio-HII)*
IRAS03035+5819	3:07:26	+58:30:52	−39.4	N	Y	Y	UCHII	–	MSF (radio-HII)*
HM04579+4703	5:01:40	+47:07:23	−17.0	N	Y	N	HMPO	–	unclassified
HM05137+3919	5:17:13	+39:22:23	−25.0	N	Y	N	HMPO	–	unclassified
HM05168+3634	5:20:16	+36:37:21	−15.0	N	Y	N	HMPO	–	unclassified
HM05274+3345	5:30:46	+33:47:52	−4.0	Y[b]	Y	Y	HMPO	–	unclassified
HM05345+3157	5:37:48	+31:59:24	−18.0	N	Y	N	HMPO	–	unclassified
HM05358+3543	5:39:10	+35:45:19	−18.0	Y[e]	Y	Y	HMPO	–	unclassified
HM05373+2349	5:40:24	+23:50:54	2.0	Y[b]	Y	N	HMPO	–	unclassified
IRAS05391−0152	5:41:39	−1:51:19	10.0	N	Y	Y	UCHII	–	MSF (radio-HII)*
IRAS05393−0156	5:41:50	−1:55:17	10.0	N	Y	Y	UCHII	–	MSF (radio-HII)*
HM05490+2658	5:52:13	+26:59:33	1.0	N	N	Y	HMPO	–	unclassified
HM05553+1631	5:58:14	+16:32:00	6.0	N	Y	N	HMPO	–	unclassified
MONR2	6:07:47	−6:22:59	9.5	N	Y	Y	UCHII	–	MSF (radio-HII)*
IRAS06056+2131	6:08:41	+21:31:01	0.0	N	N	N	UCHII	–	MSF (radio-HII)*
IRAS06058+2138	6:08:54	+21:38:25	2.5	Y[e]	Y	Y	UCHII	–	MSF (radio-HII)*
IRAS06061+2151	6:09:08	+21:50:39	−0.7	N	Y	N	UCHII	–	MSF (radio-HII)*
IRAS06063+2040	6:09:22	+20:39:28	9.5	N	Y	N	UCHII	–	MSF (radio-HII)*
IRAS06084−0611	6:10:51	−6:11:54	10.0	N	Y	Y	UCHII	–	MSF (radio-HII)*
IRAS06099+1800	6:12:53	+17:59:22	10.0	N	Y	Y	UCHII	–	MSF (radio-HII)*
HM06584−0852	7:00:52	−8:56:29	41.0	N	N	N	HMPO	–	unclassified

Appendix B: SiO line parameters

Table B.3: SiO line parameters

ID	Source name	Line	$\int T_{\rm mb}\, dv$ (K)	$v_{\rm peak}$ (km s^{-1})	$\Delta v_{\rm FWHM}$ (km s^{-1})	$T_{\rm mb,peak}$ (K)	rms (mK)
18	G024.60+00.08 MM1[a]	1	0.549±0.116	52.42±0.18	3.30±0.58	0.156	23.34
	...	2	1.490±0.171	53.61±0.86	17.92±2.89	0.078	23.34
19	G024.60+00.08 MM3[a]	1	0.312±0.156	52.61±0.30	2.55±1.35	0.115	24.49
	...	2	1.276±0.243	51.10±1.70	20.42±6.85	0.059	24.49
20	G025.04−00.20 MM1	1	1.091±0.184	62.31±0.33	4.53±1.06	0.226	54.25
21	G025.04−00.20 MM2	1	0.700±0.156	62.61±0.31	3.41±1.22	0.193	44.98
22	G028.04−00.46 MM1	1	1.123±0.163	45.53±0.54	7.23±1.29	0.146	29.76
23	G028.37+00.07 MM1	1	1.625±0.120	77.46±0.18	5.24±0.49	0.291	35.90
24	G028.37+00.07 MM2	1	0.890±0.118	79.99±0.28	4.92±0.91	0.170	32.69
25	G028.37+00.07 MM4	1	2.262±0.277	79.24±0.43	8.29±1.37	0.256	44.51
26	G028.37+00.07 MM6	1	3.397±0.202	79.95±0.16	5.73±0.44	0.557	57.02
27	G028.37+00.07 MM10	1	0.819±0.353	79.22±0.39	3.78±1.22	0.204	56.51
	...	2	2.444±0.454	77.88±1.32	16.15±3.05	0.142	56.51
28	G028.37+00.07 MM11	1	0.509±0.072	80.04±0.16	2.36±0.38	0.203	33.52
29	G028.37+00.07 MM16	1	0.636±0.131	80.92±0.83	7.58±2.06	0.079	21.98
30	G028.53−00.25 MM2	1	0.970±0.181	86.15±0.19	5.62±0.66	0.162	18.22
	...	2	1.576±0.196	85.07±0.92	20.44±2.90	0.072	18.22
31	G028.53−00.25 MM4[a]	1	2.097±0.109	85.92±0.20	8.63±0.61	0.228	24.02
32	G028.53−00.25 MM6[a]	1	2.220±0.110	86.01±0.19	8.29±0.53	0.252	25.54
33	G028.53−00.25 MM10	1	1.420±0.248	88.70±0.92	10.96±2.76	0.122	32.29
34	G030.57−00.23 MM1	1	2.131±0.235	88.72±0.58	11.80±1.72	0.17	31.50
35	G030.97−00.14 MM1	1	0.932±0.139	77.18±0.47	6.67±1.32	0.131	25.06
36	G031.97+00.07 MM1[b]	1	1.792±0.351	93.94±0.16	5.11±0.60	0.329	33.35
	...	2	3.340±0.358	95.34±0.76	17.90±2.70	0.175	33.35
37	G031.97+00.07 MM2[b]	1	1.848±0.269	94.18±0.13	4.40±0.37	0.395	34.46
	...	2	3.687±0.329	93.80±0.42	14.49±1.16	0.239	34.46
38	G031.97+00.07 MM3	1	3.021±0.173	94.75±0.31	11.74±0.86	0.242	33.05
39	G031.97+00.07 MM4	1	2.750±0.251	96.09±0.28	7.63±0.44	0.339	28.33
	...	2	0.902±0.264	85.21±1.66	10.54±3.14	0.080	28.33
40	G031.97+00.07 MM5	1	0.692±0.165	96.01±1.07	9.78±3.09	0.066	24.61
41	G031.97+00.07 MM8	1	1.642±0.202	95.28±0.44	7.66±1.22	0.201	48.90
42	G033.69−00.01 MM1	1	1.383±0.201	105.30±0.28	4.28±0.83	0.304	63.19
43	G033.69−00.01 MM2	1	0.536±0.096	104.50±0.44	4.82±0.98	0.104	22.23
44	G033.69−00.01 MM3	1	1.190±0.159	103.20±0.54	8.35±1.33	0.134	27.27
45	G033.69−00.01 MM4	1	1.445±0.130	105.60±0.18	4.15±0.49	0.327	42.54
46	G033.69−00.01 MM5	1	0.770±0.144	105.10±0.96	10.54±2.48	0.069	21.24
47	G034.43+00.24 MM1	1	1.835±0.270	57.20±0.12	4.33±0.48	0.398	32.14
	...	2	4.684±0.277	60.07±0.58	18.77±1.57	0.234	32.14
48	G034.43+00.24 MM2[b]	1	5.957±0.178	56.97±0.13	9.51±0.39	0.589	37.38
49	G034.43+00.24 MM3	1	4.016±0.181	59.39±0.33	15.41±0.90	0.245	30.80
50	G034.43+00.24 MM4[b]	1	4.562±0.158	56.01±0.13	8.15±0.37	0.526	36.57
51	G034.43+00.24 MM5	1	1.641±0.109	55.55±0.27	8.72±0.76	0.177	24.59
52	G034.43+00.24 MM6	1	1.329±0.134	57.30±0.42	8.40±0.95	0.149	33.54
53	G034.43+00.24 MM7	1	1.230±0.145	56.05±0.46	8.25±1.22	0.140	33.93
54	G034.43+00.24 MM8	1	1.848±0.269	57.29±0.96	14.46±2.77	0.120	32.82
55	G034.77−00.55 MM1	1	0.739±0.141	43.20±0.70	6.77±1.13	0.103	30.38
56	G038.95−00.47 MM1	1	1.138±0.172	40.22±0.41	5.90±1.19	0.181	45.43
57	G048.65−00.29 MM1	1	0.368±0.075	33.27±0.40	4.12±1.01	0.084	18.33
58	G053.11+00.05 MM1	1	1.837±0.114	22.94±0.33	11.87±1.00	0.145	21.30
59	G053.11+00.05 MM2	1	0.836±0.067	21.90±0.18	4.60±0.44	0.171	21.79
60	HM05274+3345	1	1.471±0.150	−3.59±0.53	10.66±1.26	0.130	23.22
61	HM05358+3543	1	1.301±0.091	−18.29±0.19	5.78±0.50	0.212	26.25
62	HM05373+2349	1	0.806±0.127	0.15±0.67	8.36±1.48	0.091	22.52
63	HM18024-2119	1	1.641±0.289	−0.54±0.77	9.34±2.58	0.165	36.76
64	HM18089-1732	1	0.356±0.063	33.20±0.16	1.80±0.35	0.186	34.06

Table B.3: continued.

ID	Source name	Line	$\int T_{\rm mb} dv$ (K)	$v_{\rm peak}$ (km s^{-1})	$\Delta v_{\rm FWHM}$ (km s^{-1})	$T_{\rm mb,peak}$ (K)	rms (mK)
65	HM18102-1800	1	1.827±0.144	19.52±0.32	8.96±0.94	0.192	22.37
66	HM18144-1723	1	1.027±0.237	47.45±0.42	5.74±1.18	0.168	29.13
	···	2	1.213±0.198	40.89±1.18	12.58±0.79	0.091	29.13
67	HM18151-1208	1	0.529±0.130	30.71±0.70	6.29±2.19	0.079	23.03
68	HM18264-1152	1	0.962±0.235	43.72±1.07	9.37±2.99	0.096	36.06
69	HM18345-0641	1	1.388±0.146	92.65±0.64	12.15±1.53	0.107	21.00
70	HM18507+0121	1	1.255±0.321	56.73±0.25	3.78±0.84	0.312	39.53
	···	2	4.301±0.471	57.08±1.10	22.14±3.38	0.183	39.53
71	HM18517+0437	1	0.571±0.081	43.88±0.27	3.88±0.67	0.138	28.72
72	HM18530+0215	1	1.264±0.154	76.66±0.77	12.76±1.74	0.093	22.09
73	HM18566+0408	1	1.353±0.152	83.74±0.73	13.15±1.72	0.097	21.08
74	HM19217+1651	1	0.854±0.134	1.87±0.83	10.46±1.88	0.077	21.16
75	HM19368+2239	1	1.326±0.140	36.16±0.26	5.43±0.78	0.229	39.08
76	HM20126+4104	1	0.405±0.078	−3.63±0.47	4.89±1.01	0.078	18.31
77	HM20188+3928	1	1.326±0.180	1.58±0.39	5.70±0.83	0.218	39.38
78	HM20293+3952	1	0.397±0.092	5.18±0.64	5.22±1.19	0.072	21.58
	···	2	0.641±0.117	20.7 5±0.85	8.79±1.50	0.068	21.58
79	HM22506+5944	1	0.908±0.140	−48.84±0.95	12.68±2.46	0.067	18.89
80	HM23033+5951	1	1.015±0.100	−51.64±0.36	7.27±0.77	0.131	27.50
81	IRAS02232+6138	1	0.869±0.069	−47.48±0.21	5.64±0.56	0.145	20.12
82	IRAS06058+2138	1	0.722±0.066	3.18±0.21	4.56±0.50	0.149	21.72
83	IRAS18032-2032	1	3.515±0.290	5.93±1.01	24.52±2.66	0.135	27.46
84	IRAS18085-1931	1	0.758±0.123	−1.41±0.55	6.98±1.40	0.102	22.98
85	IRAS18316-0602	1	3.169±0.285	39.08±0.76	19.78±2.68	0.15	26.45
86	IRAS18479-0005	1	0.496±0.115	15.86±0.99	8.51±2.36	0.055	19.59
87	IRAS19410+2336	1	0.670±0.074	22.79±0.34	6.62±0.94	0.095	19.30
88	IRAS20081+3122	1	2.554±0.126	10.95±0.17	7.94±0.54	0.302	28.49
89	IRAS22176+6303	1	0.614±0.045	−7.55±0.13	3.79±0.33	0.152	15.99
90	G5.48-0.24	1	2.171±0.321	91.57±0.49	8.50±1.13	0.240	41.92
	···	2	9.048±0.405	73.11±2.19	54.16±3.51	0.157	41.92
	···	3	1.730±0.221	115.80±2.93	21.85±4.79	0.074	041.92
91	G5.89-0.39	1	5.265±0.389	11.56±0.59	19.32±2.08	0.256	37.58
92	G8.67-0.36	1	5.152±0.315	34.39±0.28	9.66±0.74	0.501	69.39
93	G10.30-0.15	1	2.317±0.176	11.3±0.43	11.30±1.08	0.193	35.83
94	G10.47+0.03	1	2.938±0.177	66.02±0.28	10.25±0.81	0.269	36.57
95	G11.94-0.62	1	1.594±0.150	38.24±0.54	13.56±1.80	0.110	17.89
96	G12.21-0.10	1	1.753±0.172	24.97±0.71	14.83±1.76	0.111	22.09
97	G15.04-0.68	1	1.350±0.119	18.61±0.32	7.79±0.87	0.163	28.65
98	G29.96-0.02	1	0.977±0.093	97.30±0.38	8.22±0.97	0.112	22.34
99	G31.41+0.31	1	0.909±0.105	96.22±0.34	5.92±0.78	0.144	31.11
100	G33.92+0.11	1	0.734±0.089	107.20±0.29	5.17±0.92	0.133	23.32
101	G34.26+0.15	1	4.692±0.206	58.47±0.14	7.01±0.40	0.629	52.61
102	G45.47+0.05	1	1.734±0.185	61.28±0.37	7.27±1.20	0.224	37.59
103	G75.78+0.34	1	1.651±0.089	−1.16±0.22	8.33±0.53	0.186	22.03
104	W51D	1	4.846±0.326	59.32±0.44	13.01±1.02	0.350	64.45
105	DR21	1	1.175±0.095	−5.45±0.46	11.62±1.11	0.095	19.53
106	NGC 7538	1	1.573±0.084	−57.54±0.14	5.54±0.38	0.267	24.41

Appendix C: Derived column density and abundances, and physical parameters of associated dust clumps

Table C.4: Derived column density and abundances, and physical parameters of associated dust clumps

Source	N_{SiO} (cm^{-2})	Log($N^a_{H_2}$) (cm^{-2})	Log($N^b_{H_2}$) (cm^{-2})	X_{SiO}	Dist. (kpc)	T_{dust} (K)	Log(L_{bol}) ($L_\odot$)	Log(M_{clump}) ($M_\odot$)	L_{H_2O} ($L_\odot$)	L_{CH_3OH} ($L_\odot$)
DR21	7.19×10^{12}	···	···	···	···	···	···	···	···	···
G015.05+00.07MM1	5.99×10^{12}	22.500	22.348	1.89×10^{-10}	13.3	14.8	3.440	3.561	···	···
G018.82−00.28MM3	3.46×10^{12}	22.539	22.477	1.00×10^{-10}	12.6	17.8	4.240	4.024	···	···
G018.82−00.28MM4	6.16×10^{12}	22.745	···	1.11×10^{-10}	4.0	11.3	2.260	3.140	···	···
G019.27+00.07MM1	5.88×10^{12}	22.758	22.609	1.03×10^{-10}	2.8	13.8	2.403	2.927	···	···
G023.60+00.00MM4	6.50×10^{12}	···	22.561	···	···	···	···	···	···	···
G023.60+00.00MM7	5.98×10^{12}	···	22.501	···	···	···	···	···	···	···
G024.33+00.11MM1	1.28×10^{13}	23.063	23.004	1.10×10^{-10}	7.6	23.8	4.767	3.636	1.29×10^{-4}	2.03×10^{-4}
G024.33+00.11MM10	2.98×10^{12}	···	22.625	···	···	···	···	···	···	···
G024.33+00.11MM2	6.28×10^{12}	22.730	22.575	1.17×10^{-10}	7.6	12.5	2.746	3.012	6.70×10^{-7}	2.39×10^{-6}
G024.33+00.11MM3	7.45×10^{12}	22.551	22.607	2.10×10^{-10}	7.6	16.8	3.944	3.779	···	6.64×10^{-6}
G024.33+00.11MM5	1.65×10^{13}	22.656	22.632	3.64×10^{-10}	7.6	15.9	3.894	3.951	1.74×10^{-6}	6.91×10^{-6}
G024.33+00.11MM6	8.10×10^{12}	···	22.893	···	···	···	···	···	···	···
G024.60+00.08MM1	1.25×10^{13}	22.772	22.547	2.11×10^{-10}	3.6	15.9	2.850	2.884	1.14×10^{-5}	3.58×10^{-6}
G025.04−00.20MM1	6.68×10^{12}	22.837	22.610	9.72×10^{-11}	2.7	15.3	3.101	3.165	···	7.04×10^{-7}
G025.04−00.20MM2	4.29×10^{12}	22.880	22.394	5.65×10^{-11}	2.7	10.2	1.916	3.050	···	2.01×10^{-7}
G028.04−00.46MM1	6.87×10^{12}	22.551	22.124	1.93×10^{-10}	3.4	13.7	2.115	2.459	···	3.62×10^{-5}
G028.37+00.07MM1	9.94×10^{12}	23.166	23.164	6.79×10^{-11}	4.3	18.5	3.980	3.475	1.95×10^{-4}	9.99×10^{-5}
G028.37+00.07MM10	2.00×10^{13}	23.027	22.719	1.88×10^{-10}	4.3	8.9	2.192	3.644	2.23×10^{-6}	1.09×10^{-5}
G028.37+00.07MM11	3.12×10^{12}	22.334	22.563	1.44×10^{-10}	4.3	15.8	2.396	2.926	7.46×10^{-6}	···
G028.37+00.07MM16	3.89×10^{12}	22.434	22.464	1.43×10^{-10}	4.3	13.5	2.316	2.779	1.24×10^{-5}	···
G028.37+00.07MM2	5.45×10^{12}	22.751	22.590	9.66×10^{-11}	4.3	18.0	3.670	3.076	3.69×10^{-6}	6.55×10^{-6}
G028.37+00.07MM4	1.38×10^{13}	23.080	22.747	1.15×10^{-10}	4.3	9.8	2.342	3.590	9.01×10^{-6}	2.64×10^{-6}
G028.37+00.07MM6	2.08×10^{13}	22.799	22.680	3.30×10^{-10}	4.3	12.0	2.311	3.259	2.27×10^{-6}	8.00×10^{-6}
G028.53−00.25MM10	8.69×10^{12}	···	22.659	···	···	···	···	···	···	···
G028.53−00.25MM2	1.56×10^{13}	···	22.818	···	···	···	···	···	···	···
G028.53−00.25MM6	1.36×10^{13}	···	22.792	···	5.0	···	···	···	1.91×10^{-6}	2.42×10^{-6}
G030.57−00.23MM1	1.30×10^{13}	22.738	22.838	2.38×10^{-10}	4.9	19.9	3.769	3.144	···	···
G030.97−00.14MM1	5.71×10^{12}	22.841	22.630	8.23×10^{-11}	4.9	14.8	3.791	3.568	···	1.10×10^{-6}
G031.97+00.07MM1	3.14×10^{13}	23.151	22.814	2.22×10^{-10}	5.1	20.7	4.604	3.756	9.11×10^{-6}	1.03×10^{-5}
G031.97+00.07MM2	3.39×10^{13}	23.151	22.665	2.39×10^{-10}	5.1	20.7	4.604	3.756	···	···
G031.97+00.07MM3	1.85×10^{13}	22.942	22.504	2.11×10^{-10}	5.1	15.1	3.764	3.639	4.28×10^{-6}	4.55×10^{-6}
G031.97+00.07MM4	2.24×10^{13}	22.677	22.540	4.70×10^{-10}	5.1	14.0	3.473	3.653	2.72×10^{-6}	1.34×10^{-5}
G031.97+00.07MM5	4.24×10^{12}	22.714	22.320	8.18×10^{-11}	5.1	10.4	2.046	3.462	···	2.15×10^{-6}
G031.97+00.07MM8	1.00×10^{13}	···	22.387	···	···	···	···	···	···	···
G033.69−00.01MM1	8.46×10^{12}	22.997	22.755	8.52×10^{-11}	8.8	13.9	3.847	3.980	2.52×10^{-6}	4.95×10^{-5}
G033.69−00.01MM2	3.28×10^{12}	22.368	22.676	1.41×10^{-10}	8.8	27.3	4.331	2.934	···	···
G033.69−00.01MM3	7.28×10^{12}	22.607	22.447	1.80×10^{-10}	8.8	14.1	3.114	3.625	···	···
G033.69−00.01MM4	8.84×10^{12}	22.825	22.675	1.32×10^{-10}	8.8	11.9	3.298	4.038	···	8.19×10^{-6}
G033.69−00.01MM5	4.71×10^{12}	22.177	22.453	3.13×10^{-10}	8.8	24.7	3.950	3.196	8.98×10^{-7}	···
G034.43+00.24MM1	3.99×10^{13}	23.378	22.840	1.67×10^{-10}	2.9	22.7	4.027	3.128	1.36×10^{-4}	1.37×10^{-5}
G034.43+00.24MM2	3.65×10^{13}	23.249	22.885	2.05×10^{-10}	2.9	20.5	4.042	3.260	9.94×10^{-5}	2.55×10^{-5}
G034.43+00.24MM3	2.46×10^{13}	22.961	22.425	2.69×10^{-10}	2.9	14.4	2.960	3.074	5.56×10^{-6}	1.71×10^{-5}
G034.43+00.24MM4	2.79×10^{13}	23.249	22.667	1.57×10^{-10}	2.9	20.5	4.042	3.26	···	2.20×10^{-5}
G034.43+00.24MM5	1.00×10^{13}	···	22.299	···	2.9	···	···	···	2.36×10^{-5}	1.39×10^{-6}
G034.43+00.24MM6	8.13×10^{12}	···	22.201	···	···	···	···	···	···	···
G034.43+00.24MM7	7.53×10^{12}	···	22.111	···	···	···	···	···	···	···
G034.43+00.24MM8	1.13×10^{13}	···	22.121	···	···	···	···	···	···	···
G034.77−00.55MM1	4.53×10^{12}	22.654	22.486	1.00×10^{-10}	2.2	22.1	3.346	2.424	···	···
G038.95−00.47MM1	6.96×10^{12}	22.844	22.446	9.97×10^{-11}	1.9	12.7	2.091	2.790	···	···
G048.65−00.29MM1	2.25×10^{12}	22.246	22.021	1.28×10^{-10}	4.1	17.4	2.361	2.342	5.15×10^{-6}	···
G053.11+00.05MM1	1.12×10^{13}	23.007	22.625	1.11×10^{-10}	4.0	21.8	3.970	3.073	7.72×10^{-6}	8.98×10^{-6}
G053.11+00.05MM2	5.11×10^{12}	22.525	22.093	1.53×10^{-10}	4.0	14.2	2.438	2.648	1.41×10^{-6}	···
G10.30−0.15	1.42×10^{13}	23.045	···	1.28×10^{-10}	2.9	29.8	4.994	3.161	1.95×10^{-7}	1.00×10^{-5}
G10.47+0.03	1.80×10^{13}	23.803	···	2.83×10^{-11}	8.5	25.1	5.646	4.406	5.92×10^{-4}	6.25×10^{-5}
G11.94−0.62	9.76×10^{12}	23.036	···	8.98×10^{-11}	3.4	28.9	4.759	3.243	1.10×10^{-5}	1.22×10^{-6}
G12.21−0.10	1.07×10^{13}	23.340	···	4.90×10^{-11}	13.4	24.4	5.516	4.445	3.12×10^{-3}	1.40×10^{-4}
G15.04−0.68	8.26×10^{12}	···	···	···	···	···	···	···	···	···
G29.96−0.02	5.98×10^{12}	23.142	···	4.31×10^{-11}	4.9	35.5	5.650	3.542	1.01×10^{-4}	1.52×10^{-5}
G5.48−0.24	7.92×10^{13}	22.476	22.375	2.65×10^{-9}	3.0	22.0	4.218	3.241	···	···
G5.89−0.39	3.22×10^{13}	23.489	···	1.05×10^{-10}	3.0	34.5	5.326	3.232	9.81×10^{-6}	2.27×10^{-5}
G75.78+0.34	1.01×10^{13}	···	···	···	···	···	···	···	···	···
G8.67−0.36	3.15×10^{13}	23.463	···	1.09×10^{-10}	4.4	25.9	4.959	3.642	4.99×10^{-5}	7.35×10^{-5}

Table C.4: continued.

Source	N_{SiO} (cm^{-2})	Log($N^a_{H_2}$) (cm^{-2})	Log($N^b_{H_2}$) (cm^{-2})	X_{SiO}	Dist. (kpc)	T_{dust} (K)	Log(L_{bol}) ($L_\odot$)	Log(M_{clump}) ($M_\odot$)	L_{H_2O} ($L_\odot$)	L_{CH_3OH} ($L_\odot$)
HM05274+3345	9.00×10^{12}	···	23.086	···	···	···	···	···	···	···
HM05358+3543	7.96×10^{12}	···	···	···	···	···	···	···	···	···
HM05373+2349	4.93×10^{12}	···	···	···	···	···	···	···	···	···
HM18024−2119	1.00×10^{13}	22.852	22.623	1.41×10^{-10}	0.1	21.2	···	···	7.54×10^{-9}	9.11×10^{-9}
HM18089−1732	2.18×10^{12}	23.267	···	1.18×10^{-11}	2.5	23.4	4.254	3.099	2.03×10^{-5}	7.13×10^{-6}
HM18102−1800	1.12×10^{13}	···	22.862	···	···	···	···	···	···	···
HM18144−1723	1.37×10^{13}	22.871	22.768	1.85×10^{-10}	4.5	25.7	4.373	3.074	3.26×10^{-5}	6.03×10^{-5}
HM18151−1208	3.24×10^{12}	···	···	···	···	···	···	···	···	···
HM18264−1152	5.88×10^{12}	23.260	22.843	3.23×10^{-11}	3.3	20.3	3.897	3.214	5.59×10^{-5}	2.38×10^{-5}
HM18345−0641	8.49×10^{12}	22.478	22.481	2.83×10^{-10}	5.6	21.9	3.752	2.799	···	1.66×10^{-5}
HM19368+2239	8.12×10^{12}	22.719	22.610	1.55×10^{-10}	4.4	18.5	3.449	3.095	···	2.16×10^{-5}
HM20126+4104	2.48×10^{12}	···	···	···	···	···	···	···	···	···
HM20188+3928	8.12×10^{12}	···	22.816	···	···	···	···	···	···	···
HM20293+3952	6.35×10^{12}	···	22.737	···	···	···	···	···	···	···
HM22506+5944	5.56×10^{12}	···	22.407	···	···	···	···	···	···	···
HM23033+5951	6.21×10^{12}	···	···	···	···	···	···	···	···	···
IRAS02232+6138	5.32×10^{12}	···	···	···	···	···	···	···	···	···
IRAS06058+2138	4.42×10^{12}	···	22.908	···	···	···	···	···	···	···
IRAS18032−2032	2.15×10^{13}	23.214	···	1.31×10^{-10}	5.2	32.1	5.379	3.523	9.69×10^{-5}	7.71×10^{-6}
IRAS18085−1931	4.64×10^{12}	22.895	22.782	5.91×10^{-11}	1.0	21.7	3.301	2.314	···	···
IRAS18316−0602	1.94×10^{13}	23.177	···	1.29×10^{-10}	2.1	23.4	3.971	2.870	6.13×10^{-4}	8.72×10^{-6}
IRAS18479−0005	3.03×10^{12}	23.171	22.193	2.05×10^{-11}	9.7	34.2	5.844	3.900	1.88×10^{-4}	···
IRAS19410+2336	4.10×10^{12}	23.021	22.668	3.91×10^{-11}	2.9	23.6	4.186	3.122	2.86×10^{-5}	5.96×10^{-6}
IRAS20081+3122	1.56×10^{13}	···	···	···	···	···	···	···	···	···
IRAS22176+6303	3.76×10^{12}	···	···	···	···	···	···	···	···	···
NGC 7538	9.63×10^{12}	···	23.270	···	···	···	···	···	···	···
W51D	2.97×10^{13}	23.687	···	6.10×10^{-11}	5.2	35.2	6.157	4.109	1.57×10^{-2}	4.08×10^{-5}

Appendix D: SiO 1 – 0 spectral lines

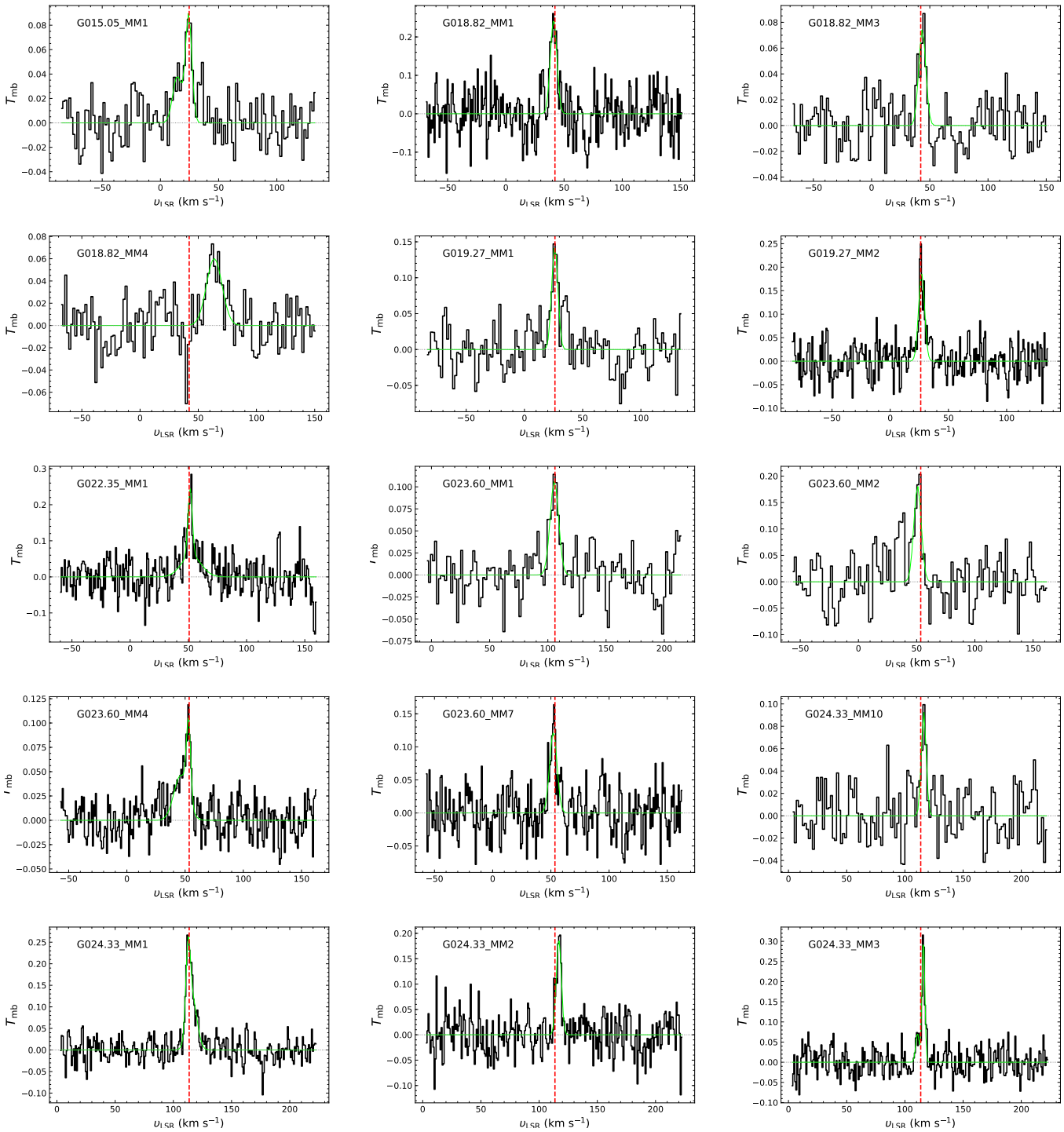

Fig. D.1: 43 GHz SiO $J = 1 - 0$ spectra in a T_{mb} scale, toward sources from the three different catalogs that are IRDC, HMPO, and UCHII.

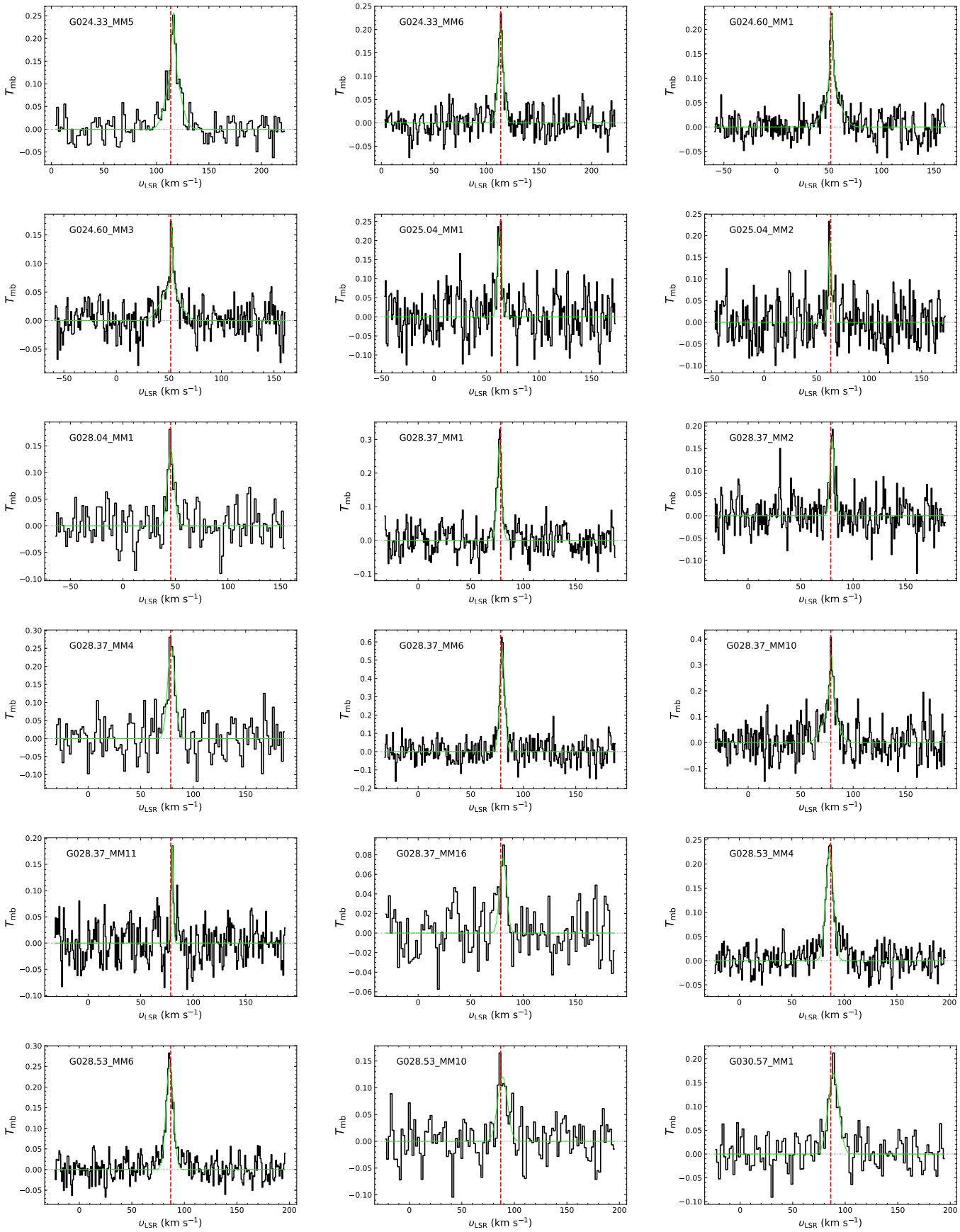

Fig. D.2: Continuation of Fig. D.1

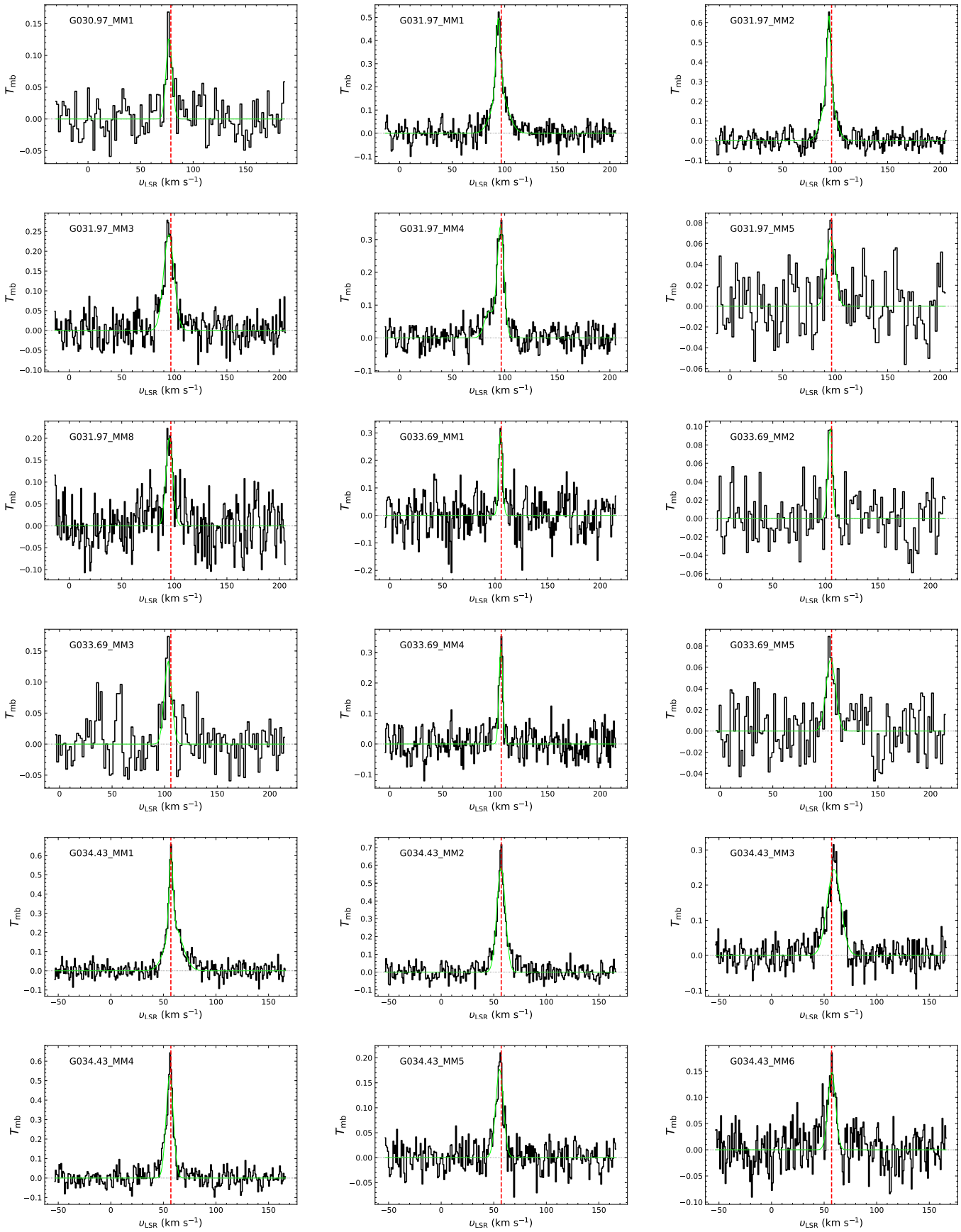

Fig. D.3: Continuation of Fig. D.1

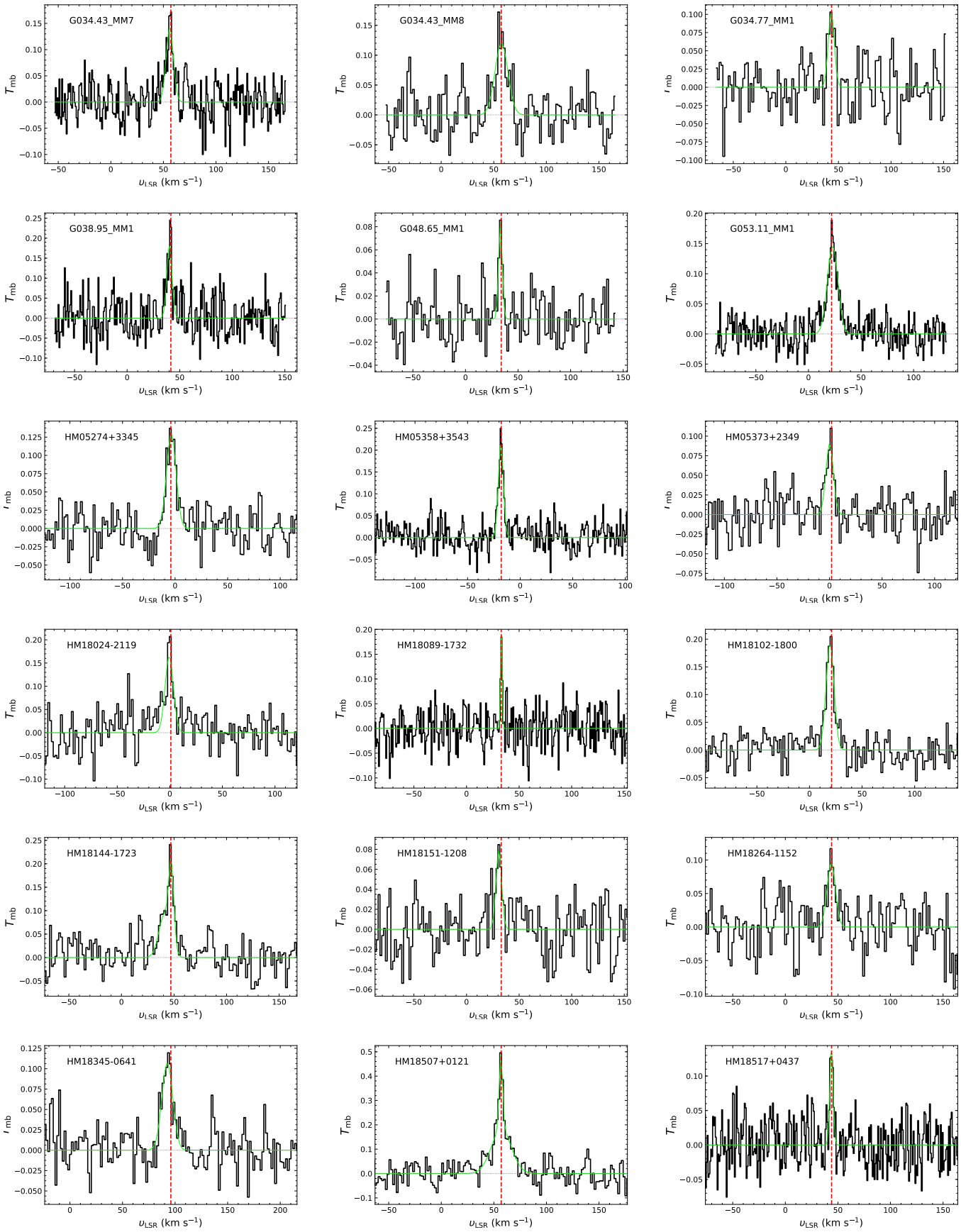

Fig. D.4: Continuation of Fig. D.1

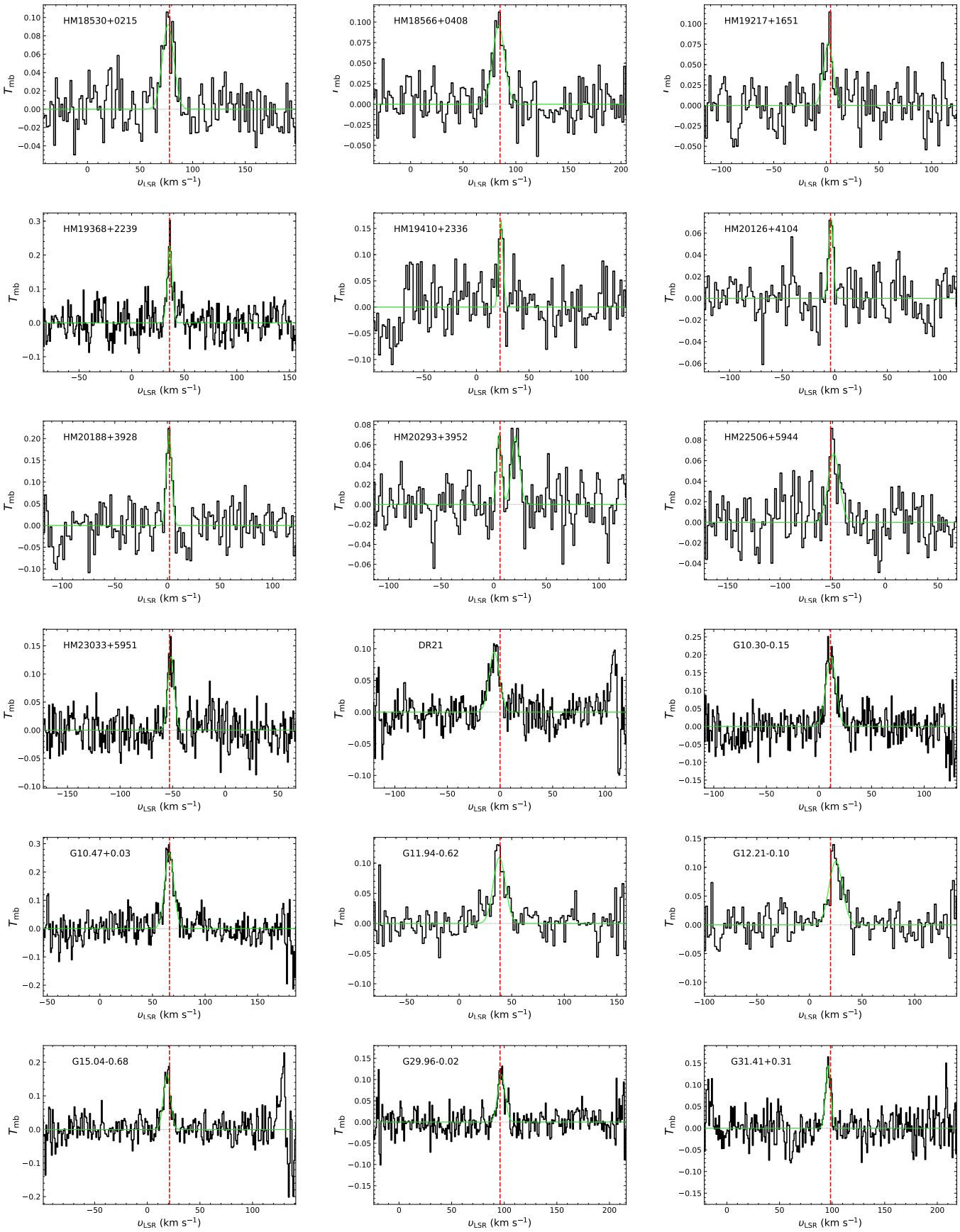

Fig. D.5: Continuation of Fig. D.1

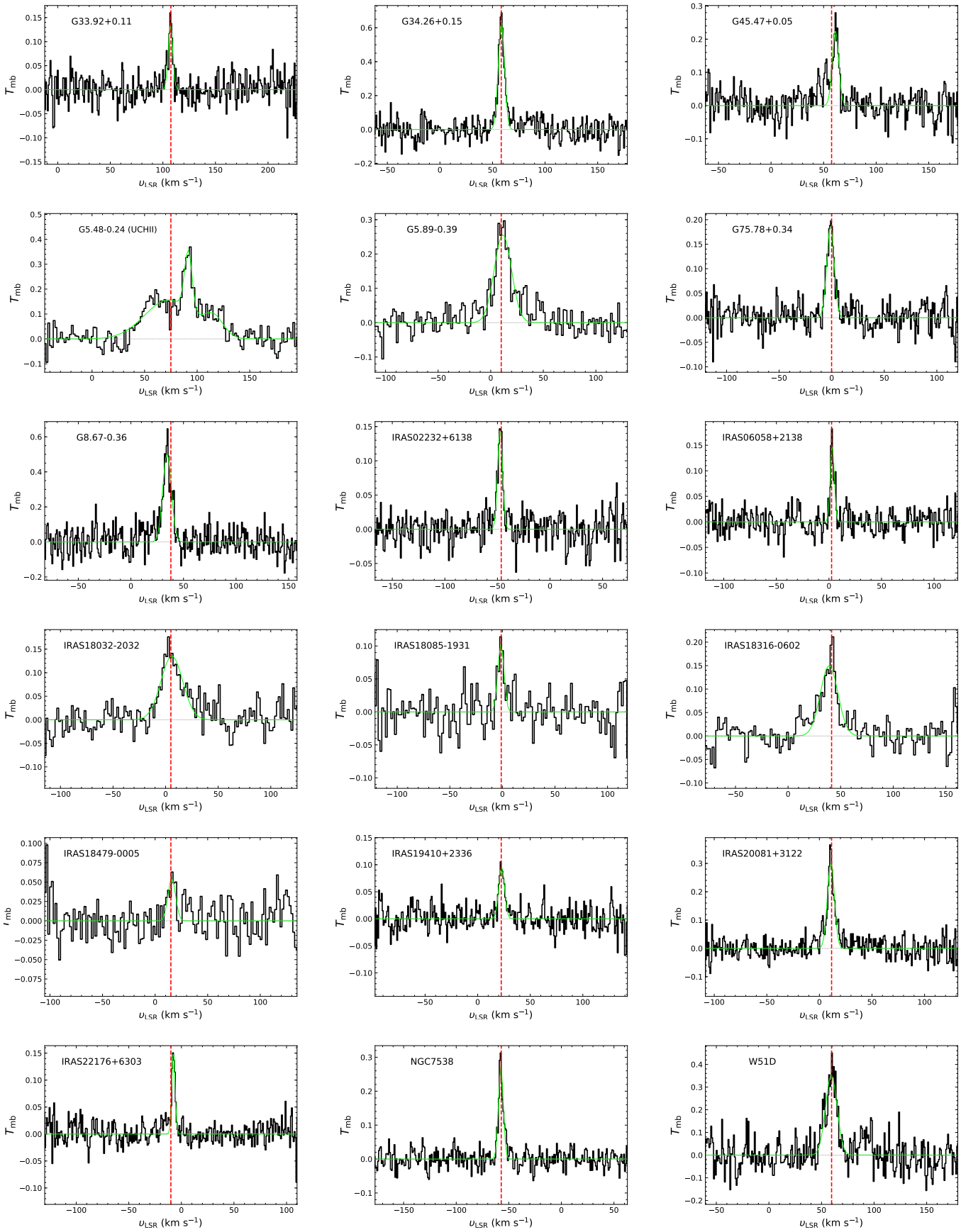

Fig. D.6: Continuation of Fig. D.1

Appendix E: Histograms

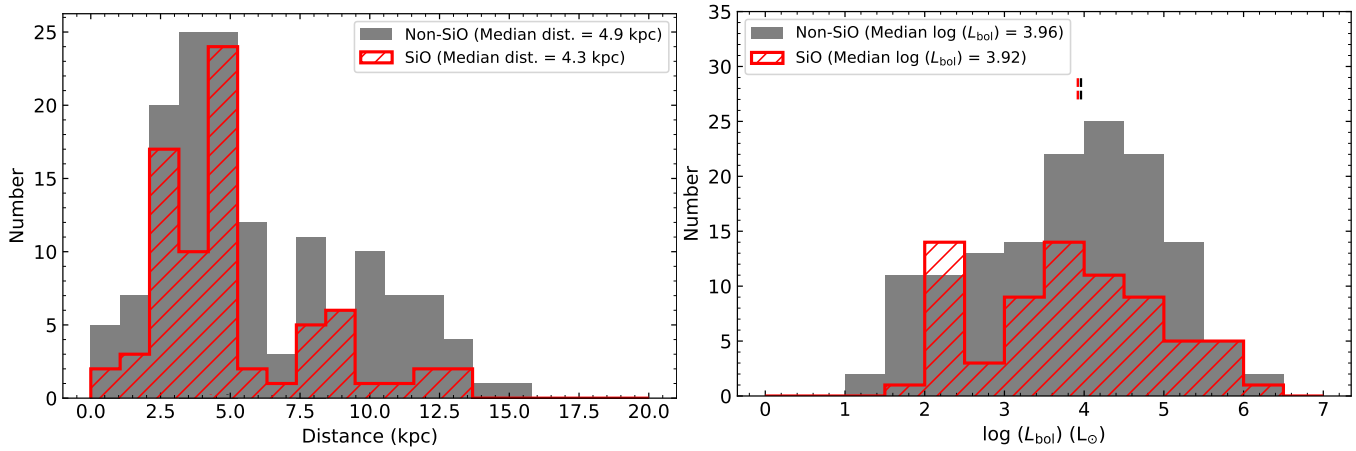

Fig. E.1: Histograms of distance (left) and bolometric luminosity (right)for sources with SiO detection (red) and non-detection (gray).